Universität Stuttgart

Light emission from lanthanide-doped AlN and $Al_xIn_{1-x}N$ layers

Dissertation

Von der Fakultät Chemie der Universität Stuttgart zur Erlangung der Würde eines Doktors der Naturwissenschaften (Dr. rer. nat.) genehmigte Abhandlung

vorgelegt von

Herrn Dipl.-Ing. Miao Yang
aus Peking, VR. China

Hauptberichter:	Prof. Dr. Dr. h.c. Guido Schmitz
Mitberichter:	Prof. Dr. Joachim Bill
Mitprüfer:	Prof. Dr. Peer Fischer
Betreuer:	Prof. Dr. Horst P. Strunk
	Prof. Dr. Dr. h.c. Guido Schmitz

eingereicht am: 20. Juli 2015
Tag der mündlichen Prüfung: 29. September 2015

Institut für Materialwissenschaft der Universität Stuttgart
2015

With four parameters I can fit an elephant, and with five I can make him wiggle his trunk.

— Johnny von Neumann [1]

Acknowledgement

Die vorliegende Arbeit wurde im Zeitraum von September 2011 bis April 2015 am Institut für Materialwissenschaft der Universität Stuttgart durchgeführt. Ich möchte mich an dieser Stelle bei all denen bedanken, die mich bei der Anfertigung meiner Dissertation so kräftig unterstützt haben.

Ganz besonders bedanken möchte ich mich bei meinem Doktorvater, Herrn *Prof. Dr. Horst P. Strunk*, für das nette Angebot einer Assistentenstelle mit Gelegenheit zur Promotion nach meinem Diplomstudium sowie in mich gesetztes Vertrauen. Ohne Ihre unvergleichlichen Unterstützungen sowie fruchtbaren Diskussionen bei allen Forschungsvorhaben wäre diese Arbeit nicht entstanden.

Ein Herzliches dankschön geht an Herrn *Prof. Dr. Guido Schmitz*, der die Betreuung in der Schlussphase meiner Promotion unverzüglich übernahm und als Hauptberichter meine Arbeit begutachtete. Ebenso sei mein Dank am Herrn *Prof. Dr. Joachim Bill* gerichtet, nicht nur für die Bereitschaft, als Mitberichter diese Arbeit zu evaluieren, sondern auch für die Zulassung, die spektroskopischen Instrumente in seiner Arbeitsgruppe langjährig zu benutzen. Außerdem möchte ich mich bei Herrn *Prof. Dr. Peer Fischer*, Institut für Physikalische Chemie der Universität Stuttgart, für die freundliche Übernahme des Mitprüfers bzw. Vorsetzender der Doktorprüfung bedanken.

Bei Herrn *Dr. Shangda Jiang*, der mir ein treuer Freund ist und am 1. Physikalisches Institut der Universität Stuttgart arbeitete[1], möchte ich mich herzlichst für die Beantwortung meiner endlosen Fragen über Kristall-Field Theorie (oft auf dem Bartisch) bedanken. Außerdem bin ich ihm für die Erlaubnis, seine Auswertungsalgorithmen in meiner Arbeit anzuwenden, zu Dank verpflichtet.

Des Weiteren möchte ich mich bei Herrn *Apl. Prof. Dr. Klaus Thonke* und seinen Mitarbeiter, Herr *Sebastian Bauer*, Herr *Niklas Bayrle* und Herr *Murat Yildirim*, Institut für Quantenmaterie der Universität Ulm, für die Tieftemperatur-Photolumineszenz-Messungen und den koffeinreichen Empfang bei regelmäßigen Diskussionen über Messergebnisse bedanken. Ferner geht großer Dank an Herrn *Dr. Michael Jetter*, Herrn *Jan Kettler*,

---

[1] jetzt am Laboratoire National de Champs Magnétiques Intenses (LNCMI), Grenoble, Frankreich

---

[2] jetzt an der Fakultät für Werkstoffwissenschaften und -technik, Universität Nanchang, VR. China
[3] jetzt am Institut für Werkstoffwissenschaft der TU Bergakademie Freiberg, Deutschland

Abstract

Optical properties of lanthanide doped phosphors and semiconductors are of great interest especially in view of solid-state light emitting devices of the next generation. Radiative intra-$4f$ electron transitions of trivalent lanthanide ions present sharp and well-defined emission lines at the wavelengths from UV to IR part of the spectrum. However, their intensity is comparatively weak hitherto. In the scope of this dissertation, wide band gap III-nitride semiconductors, AlN and $Al_x In_{1-x} N$, are chosen as host materials and doped with Pr, Sm, Tb and Tm ions respectively. According to our elaborate optoelectronic, structural and compositional characterisations, we attempt to find an innovative guideline how to obtain the lanthanide luminescence and increase their intensity.

In the light of crystal field (CF) theory, *electrostatic perturbation with a non-central symmetry on the lanthanide ions* is a fundamental requirement for the selection of host material to achieve their intra-$4f$ transitions. Splitting of low-temperature photoluminescence (PL) peaks from AlN:Sm and AlN:Tb layers reveals that most of the radiative lanthanide ions are substitutionally located in a C_{3v} local symmetry. Physical and structural information of this architecture in AlN:Sm system (namely the effective point charge of four surrounding N ions felt by the $4f$-electrons of Sm ion and their spatial positions related to $4f$-electron orbital of Sm ion) is determined through our preliminary efforts by using computer-assisted fitting procedure.

Once the host material is defined, intensity of the lanthanide luminescence can be "extrinsically" enhanced by three ways. (1) *Appropriate thermal treatment* is a conventional technique for this purpose. The atomic rearrangements activated thereby can be considered as a joint reaction of first order. By introducing a concept of "extended lanthanide luminescence centres" we are able to simplify the description of this intensity enhancement in AlN:Ln system with only two thermodynamic and kinetic parameters.

From the PL spectra of AlN with and without lanthanide doping, we confirm that the luminescence generated by carrier recombination within O-associated defect states can be strengthened particularly after annealing at intermediate temperatures (300 - 600 °C). The peak of this defect luminescence covers the required energy for the excitation of lanthanide luminescence. Both of them exhibit therefore a correlated development. This result enables us to assist the excitation processes of lanthanide luminescence centre through (2) *utilising available defect states within the band gap.*

Inspired of this, lanthanide luminescence can be further intensified by (3) *establishing ad-*

ditional excitation path via engineering the band structure of host material. This method is proven to be effective in $Al_{0.87}In_{0.13}N$:Tm and $Al_{0.84}In_{0.16}N$:Pr systems. Due to decomposition at proper temperature, we observe an almost instantaneous formation of nano-sized In-rich $Al_xIn_{1-x}N$ quantum dots (QDs) with subsequent comparatively slow coarsening. This coarsening permits us to modify the band gap energy of QDs by altering their size, which is a function of the annealing temperature and duration. If this band gap energy is in resonance with the $4f$-levels to be excited in the lanthanide ions, luminescence intensity increases. An elaborate model, relating thermal formation of "extended lanthanide luminescence centres", time-dependent variation of band gap energy and resonant energy transfer, can sufficiently describe the development of lanthanide luminescence intensity during the annealing.

Kurzzusammenfassung

Optische Eigenschaften von lanthanoide-dotierten Leuchtstoffen und Halbleitern sind von großem Interesse, insbesondere im Hinblick auf Festkörperbeleuchtungsvorrichtungen nächster Generation. Strahlende intra-$4f$ Elektronenübergänge von dreiwertigen Lanthanoid-Ionen präsentieren scharfe und wohldefinierte Emissionslinien mit den Wellenlängen im UV- bis IR-Bereich des Spektrums. Allerdings ist ihre Intensität bisher vergleichsweise schwach. Im Rahmen von dieser Dissertation wurden III-Nitrid-Halbleiter mit breiter Bandlücke, AlN und $Al_xIn_{1-x}N$, als Wirtsmaterialien ausgewählt und jeweils durch Pr-, Sm-, Tb- und Tm-Ionen dotiert. In Anlehnung an unseren umfangreichen optoelektronischen, strukturellen und chemischen Charakterisierungen versuchen wir eine innovative Richtlinie zu finden, wie man die Lanthanoide-Lumineszenz erhalten und ihre Intensität erhöhen kann.

Gemäß der Kristall-Field (CF) Theorie ist die *elektrostatische Störung mit einer Nicht-Zentralsymmetrie auf den Lanthanoide-Ionen* eine fundamentale Anforderung an die Auswahl des Wirtsmaterials, um ihre intra-$4f$ Übergänge zu erzielen. Die Aufspaltung der Photolumineszenz (PL)-Peaks von AlN:Sm- und AlN:Tb-Schichten bei tiefer Temperatur zeigt, dass die meisten strahlenden Lanthanoide-Ionen in einer C_{3v} lokalen Symmetrie substitutionell lokalisiert sind. Physikalische und strukturelle Information dieser Architektur im AlN:Sm-System (nämlich die auf $4f$-Elektronen des Sm-Ions wechselwirkende effektive Punktladung von den vier benachbarten N Ionen und ihre räumlichen Positionen in Bezug auf $4f$-Elektronschale des Sm-Ions) wurde durch unsere ersten Versuche mit Hilfe von computerunterstütztem Anpassungsverfahren bestimmt.

Solange das Wirtsmaterial festgelegt ist, kann die Intensität der Lanthanoide-Lumineszenz durch drei Maßnahmen "extrinsisch" erhöht werden. (1) *Geeignete Wärmebehandlung* ist eine konventionelle Technik, um diesen Zweck zu erzielen. Die dadurch aktivierten Atomumlagerungen können als eine gemeinsame Reaktion erster Ordnung betrachtet werden. Durch Einführung eines Konzeptes der "erweiterten Lanthanoide Lumineszenz-Zentren" sind wir imstande, die Darstellung der Intensitätsverstärkung in AlN:Ln System auf lediglich zwei thermodynamische und kinetische Parameter zu vereinfachen.

Laut der PL-Spektren von AlN mit und ohne Lanthanoide-Dotierung bestätigen wir, dass die Lumineszenz, die durch Rekombination von Ladungsträgern innerhalb der O-assoziierten Defektniveaus erzeugt wird, vorzugsweise nach der Glühung bei mittleren Temperaturen (300 - 600 °C) verstärkt werden kann. Der Peak dieser Defektlumineszenz

überlappt sich mit der benötigten Energie für die Anregung der Lanthanoide-Lumineszenz. Daher weisen die beiden eine korrelierte Entwicklung auf. Dieses Ergebnis ermöglicht uns, die Anregungsprozesse vom Lanthanoide Lumineszenz-Zentrum durch (2) *Ausnutzung verfügbarer Defektniveaus innerhalb der Bandlücke* zu unterstützen.

Inspiriert von dieser Beobachtung, kann die Lanthanoide-Lumineszenz durch (3) *Aufbau eines zusätzlichen Anregungspfades via Engineering der Bandstruktur des Matrixmaterials* intensiviert werden. Dieses Verfahren wird in $Al_{0.87}In_{0.13}N$:Tm- und $Al_{0.84}In_{0.16}N$:Pr-Systeme als effektiv erwiesen. Infolge der Entmischung bei angemessener Temperatur beobachten wir eine fast unverzögerte Ausbildung von In-reichenden $Al_xIn_{1-x}N$ Quantenpunkten (QDs) in Nano-Größe mit anschließender vergleichsweise langsamer Vergröberung. Diese Vergröberung erlaubt uns, die Bandlückenenergie der Quantenpunkte durch Änderung ihrer Größe, die eine Funktion von der Glühtemperatur und -dauer ist, zu modifizieren. Wenn diese Bandlückenenergie in Resonanz mit den zu anregenden $4f$-Niveaus in den Lanthanid-Ionen ist, erhöht sich die Lumineszenzintensität. Ein ausgearbeitetes Modell, welches auf die thermische Ausbildung von "erweiterten Lanthanoide Lumineszenz-Zentren", die zeitabhängigen Variation der Bandlückenenergie und den Resonanz-Energietransfer bezogen ist, kann die Entwicklung von Lanthanoide Lumineszenzintensität im Laufe der Glühung zulänglich beschreiben.

Contents

Chapter 1

Introduction

1.1 Current approaches on solid-state lighting development

Although the application of renewable energy has been rapidly developed in recent years, fossil fuels as the main energy source and major pollution source of carbon dioxide (CO_2) are still irreplaceable in the electricity generation. Due to the technological limitations, current electricity consumptions are clearly unsustainable. Without taking specific measures, the energy-related CO_2-emission will be at least doubled in the middle of 21st century as predicted in [2]. Hence, a rational and efficient use of electric energy is imperative. According to the mandatory eco-design requirements promulgated by European Commission (commission regulation (EC) No 244/2009 [3]), as of 2016, almost all of the lamps for household applications with energy efficiency class lower than "B" will be prohibited to be placed on the European market. As an excellent alternative to the conventional lighting sources (such as incandescent lamps with a typical luminous efficacy of 17 lm/W and fluorescent lamps with maximum efficacy of 90 lm/W), the solid-state lighting (SSL) devices, in particular light-emitting diodes (LEDs), have a significant advantage that it has the highest possible energy efficiency up to several hundreds of lm/W [4]. In addition, they are more eco-friendly in comparison with the mercury vapour containing fluorescent lamps.

Light emission from semiconductor band-band transition

Applying an appropriate voltage in the forward direction of LED, electrons populated in the n-type conduction band are "forced" to recombine with the holes in p-type valence band. Energy released thereby can be emitted in form of photons. The photon energy and thus the luminous colour are therefore determined by the direct band gap energy of semiconductor in the active region, and the resulting light emission is comparatively monochromatic. In order to generate white-light, which is one of the most important LED applications, a promising approach is to use a "multichip" technique. As shown in figure 1.1 (a) it consists of an assembly of three (or four) separate LEDs emitting blue, green, red (and yellow) light. Through adjusting the emission intensity of each LED, the colour
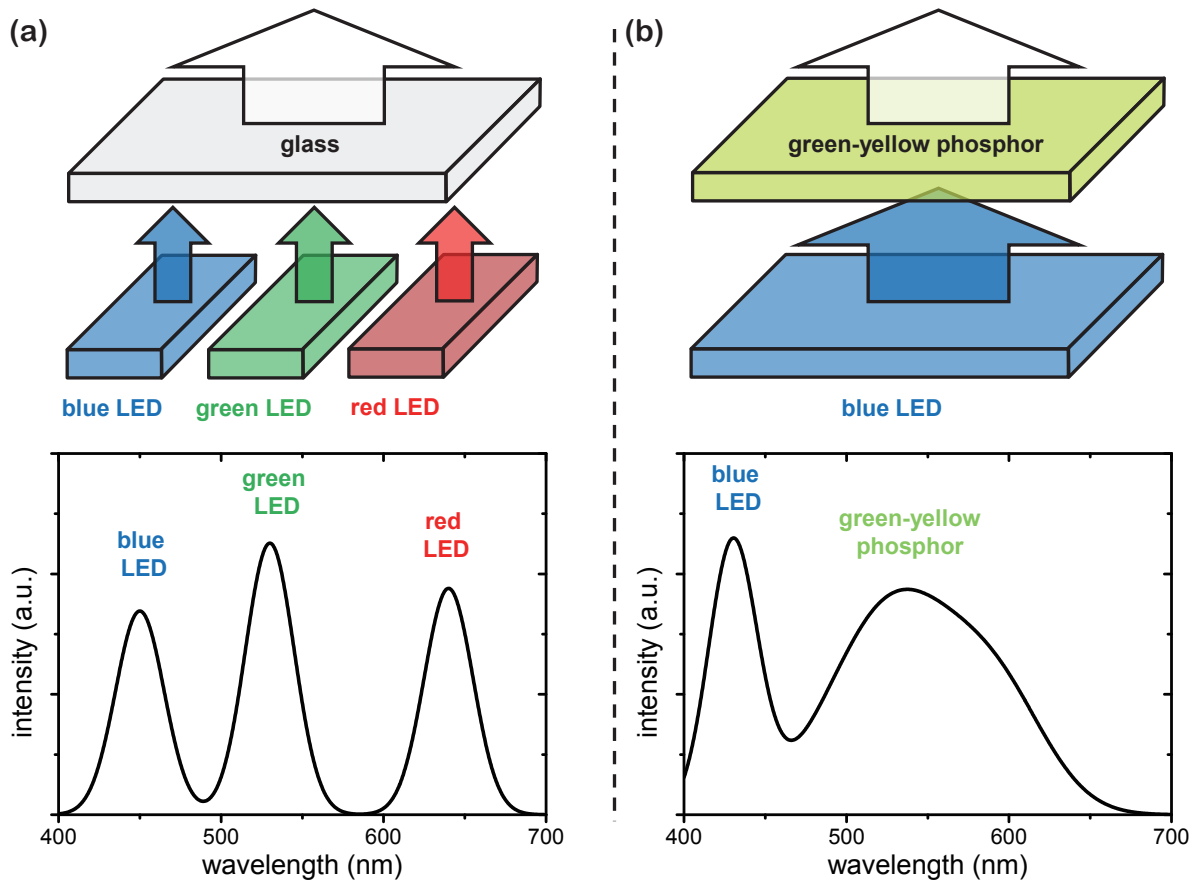
Figure 1.1: Sketches on the structure and the corresponding emission spectra of wright-lighting LED using (a) multichip technique and (b) phosphor converter.

rendering index (CRI)[1] is able to surpass 85 for three component system and 95 for four [6], which fulfils the requirements of indoor illustration [7]. After decades of breakthrough and improvement, the external quantum efficiencies (EQE) of inorganic violet-blue and red emitting LEDs (respectively based on GaInN and (Al,Ga)InP system) are already above 50 % [8]. In 2014, the Nobel Prize in Physics was jointly awarded to three Japanese and japanese-american scientists, Isamu Akasaki, Hiroshi Amano and Shuji Nakamura, due to their tireless works on the invention of efficient blue LED.

However, current development of LED multichip technique still remains challenging. One major issue is the lack of suitable material for high efficient green-yellow emission. Although GaInN with higher content of InN (corresponds to alter the luminous colour from blue to green by reducing the band gap energy) was widely expected as a candidate for this [9], the LEDs based thereon suffered from performance limitations. Piezoelectric and spontaneous polarisation as well as crystal defects and phase separation were believed as the dominant factors for their efficiency drop [10, 11, 12, 13]. Additionally, because of the transformation from direct to indirect semiconductor [14], it is also impossible to increase the AlInP content in (Al,Ga)InP (corresponds to alter the luminous colour from

---

[1] In 1777 a color theorist, George Palmer, found that the colors of objects perceived by human eye are strongly depending on the color of light source [5]. CRI is an important indicator of the light source to inspect its color reproduction. The maximum CRI value, 100, is defined by sun light.

red to green by enlarging the band gap energy) to cover this "green-yellow gap". Secondly, high efficiency of III-V LEDs can be achieved only at lower injection current and operating temperature, which restrict the practical applications of high-power, large-area LED based white lighting source [15, 16]. While the mechanisms of efficiency quenching at high current are not fully understood, two hypotheses respectively pointing at indirect Auger-process [17, 18] and leakage of injected carriers from the active region [19, 20, 21] are well accepted for III-V LEDs. Moreover, injection current, working environment and thermal design of the assembly determine the LED operating temperature. If it is above, say, 120 °C, phonon-associated processes will lead to an efficiency droop and, particularly for (Al,Ga)InP, a red shift of emission spectrum [22]. The third challenge, which plays the most important role in commercialisation of LEDs, is that the multichip concept for white-lighting complicates the production processes and raises the cost.

Phosphors as energy down-converters

In contrast to the multichip approach, the more economical phosphor-converted LED (pc-LED) uses only one short-wavelength LED with phosphor coatings. A most common phosphor is yttrium aluminium garnet doped with trivalent cerium (YAG:Ce^{3+}, see figure 1.1 (b)). The primary blue light emitted from GaInN LED is partly absorbed thereby and down-converted into broadband green-yellow luminescence in the wavelength region between 520 and 640 nm, which corresponds to the radiative transition from $4f^05d^1$ to $4f^1$ of Ce^{3+} [23, 24]. The intrinsic luminescence quenching temperature of this phosphor coating (up to 500 °C [25]) is much higher than that of conventional LEDs. Combination of phosphor luminescence and residual blue emission from GaInN LED produces a white light with acceptable efficiency but fairly low CRI value (70 - 80). Hence it can be used only for outdoor lighting with less demand. Through adopting an additional red-emitter, for instance co-doping of the YAG with other lanthanide ions or using nitridosilicate-based phosphors [26, 27, 28], the resulted CRI value can be significantly improved and approach that of the multichip approach. However, the luminous efficacy of such pc-LED reduces substantially due to unpreventable Stockes energy loss [29] during wavelength conversion [4].

Quantum dots and trivalent lanthanide ions as light emitters

According to the *status quo* of LEDs mentioned above, optimising the present production processes and, more importantly, looking for innovative materials with high luminous efficacy are the major tasks in view of optoelectronic development engineers and scientists. Beside of electroluminescence devices based on organic materials (viz. organic light-emitting diodes (OLED) and polymer light-emitting diodes (PLED)), which have only limited emission range and suffer from high sensitivity against water and oxygen as well as mechanical instability [30, 31, 32], light emission generated through recombination of the carriers confined in inorganic quantum dots (QDs) and radiative intra $4f$-transitions of lanthanide ions are two novel approaches toward next-generation SSL device.
A significant advantage of QDs is their precisely tuneable emission wavelength according to the size-dependent quantum confinement effect (for more details see section 5.2.1).
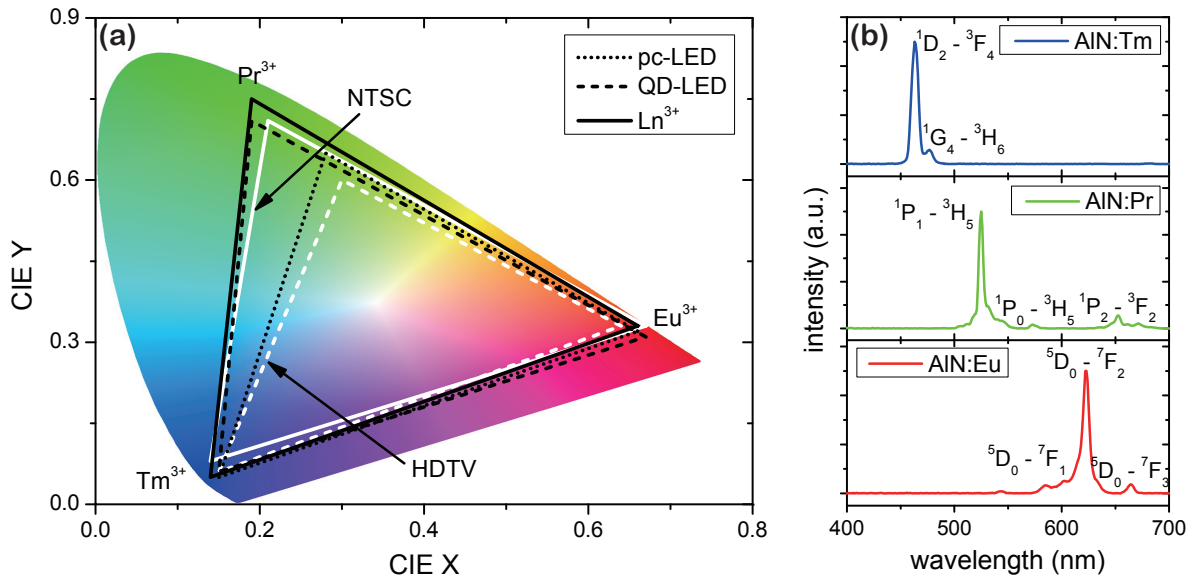
Figure 1.2: (a). CIE chromaticity diagram with the colour gamut mentioned in text; (b) - (d) the PL spectra used to calculate the CIE coordinates of lanthanide ion emission by using colour-matching functions [33]. Results of Tm^{3+} and Pr^{3+} are taken from chapter 4 of this work and Eu^{3+} from the bachelor thesis of M. Böhme [34]

Current colloidal QDs with a core-shell structure (e.g. CdSe-core with lower band gap energy clad in CdS/CdZnS/ZnS-shell with larger band bap energy [35, 36]) exhibit extended absorption cross-section at shorter wavelength region and approximate unity internal quantum yield [37]. Hence they can be served as promising energy down-converter instead of phosphors descript above. Recently, S. Jun and his co-workers reported that the luminous efficacy of white-lighting QD-LED by using in silica-encapsulated CdSe QDs as green and red converters reaches 47 lm/W. This is the highest value so far [38]. Moreover, benefited from rapid nucleation and consecutive much slower growth rate, the chemically synthesised QDs have a narrow size-distribution, which leads to purer emission colour with a typical full width at half-maximum (FWHM) of 20 - 40 nm [39]. This feature renders QD-LEDs as a more energy-efficient and vivid light source, which could not only be used in the backlight unit of liquid crystal displays (LCD) [40] but also be pixelated as RGB electroluminescence (EL) elements for full-colour display [41]. In the chromaticity diagram made by the International Commission on Illumination (CIE chromaticity diagram, as shown in figure 1.2 (a)) the colour gamut of colloidal QDs emission (black dash line) [42] is 46.4% larger than the requirement for HDTV (grey dash line, corresponds to ITU-R Recommendation BT.709 [43]), 21.1% larger than the colour gamut of pc-LED (black dotted line) [42] and even 3.7% larger than the television colour standard established by National Television System Committee (NTSC) in 1953 (grey solid line) [44]. Trivalent lanthanide ion is another candidate for light emission with much higher thermal and chemical stability. Photoluminescence (PL) results of our previous and present works (figure 1.2 (b) - (d)) indicate that if appropriate lanthanide ions are doped in AlN host, FWHMs of monochromatic blue ($^1D_2$ - $^3F_4$ and $^1G_4$ - $^3H_6$ of Tm^{3+}), green ($^1P_1$ - $^3H_5$ of Pr^{3+}) and red luminescence peak ($^5D_0$ - $^7F_2$ of Eu^{3+}) are smaller than 5 nm.

This provides, to our knowledge, the largest RGB colour gamut (10.8% larger than NTSC standard, see black solid line in figure 1.2 (a)). And for this reason, they may have a great application potential in solid-state lighting and full-colour display. Different to the above mentioned lighting sources, light emission of trivalent lanthanide ions is originated from radiative intra $4f$-configurational transitions with diverse excitation mechanisms. These will be briefly introduced in next section.

1.2 Light emission from intra $4f$-transitions of lanthanide ions and their electroluminescent devices

Fundamental properties of the lanthanide $4f$-orbital

States of a multi-electron system are expressed by a total Hamiltonian operator $\hat{H}$, which includes different interaction terms:

$$\hat{H} = \hat{H}_0 + \hat{H}_{ee} + \hat{H}_{so} + \hat{H}_{CF} + ...,\tag{1.1}$$

where $\hat{H}_0$ represents the influence of central force field, $\hat{H}_{ee}$ the Coulomb interaction between electrons within the considered system, $\hat{H}_{so}$ the spin-orbit interactions and $\hat{H}_{CF}$ the crystal field interaction. Other interactions, such as two- and three-particle interaction, electrostatically correlated spin-orbit interaction and relativistic effects etc., are too weak to induce susceptible perturbations on the total Hamiltonian of $4f$-electrons in lanthanide ions [45] and thus can be neglected in the scope of light emission.

In case of trivalent lanthanide ions, if they are doped in semiconductor host, the $4f$-electrons are intuitively shrunken towards the nucleus. Electrostatic perturbations caused by surrounding ions are essentially screened by outer 5s- and 5p-electrons and thus relative weak. As indicated in figure 1.3, the crystal field related state splitting with merely several hundred cm^{-1} is in general one and two magnitude weaker than that caused by spin-orbit and electron-electron interactions respectively ($\hat{H}_{CF} < \hat{H}_{so} < \hat{H}_{ee}$) [46]. The energy of the photons stemming from the radiative intra-$4f$ transitions is therefore independent of the host material. For this reason, it is more convenient to use spectroscopic measurements instead of *ab-initio* calculations to determine the energy positions of $4f$-levels of all trivalent lanthanide ions, which were tabulated in the book written by G.H. Dieke in 1968 [47]. Through summarising the data from our own PL-spectra and [47], energy diagrams of $4f$-levels for the lanthanides studied in this work are illustrated in figure C.1 of appendix C.

The energy levels of $4f$ electrons are denoted by Russell-Saunders term symbols with the form:

$$^{2S+1}L_J.\tag{1.2}$$

Here S represents the total spin quantum number, L the orbital angular momentum and $J = S + L$ the total angular momentum. In general, L is specified in spectroscopic notation, in which the numbers $L = 0, 1, 2, 3, 4, 5, ...$ are replaced by the letters $S, P, D, F, G, H, ...$. The possible J-states for a given combination of L and S are deter-
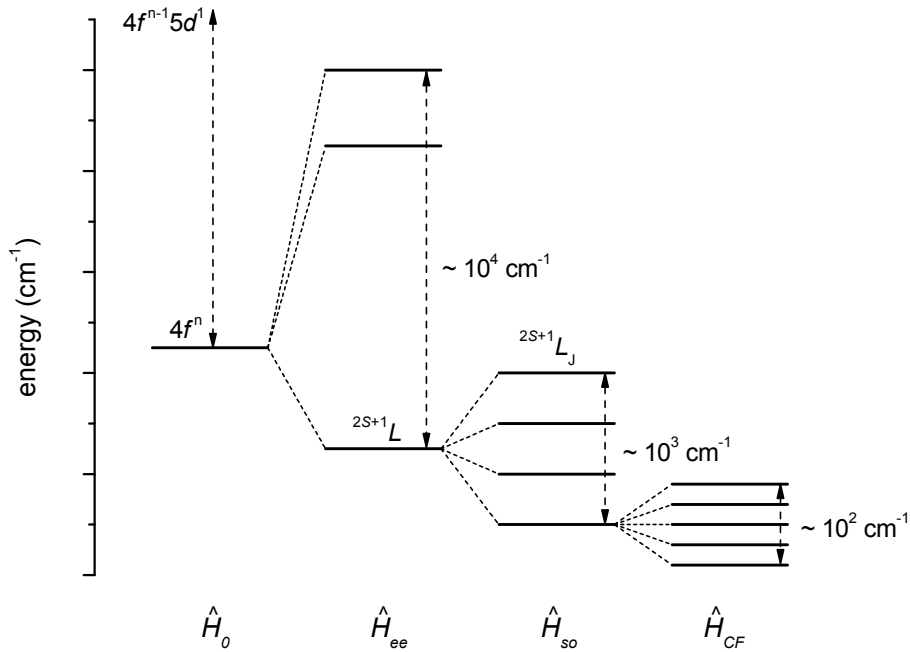
Figure 1.3: Qualitative energy scale of the $4f$ electronic structures of lanthanide ions (redrawn according to [46]). The splitting of $4f$-level due to electron-electron interaction, spin-orbit coupling and crystal field (from left to right) is schematically illustrated.

mined by the angular momentum summation rules, namely $|L - S| \leq J \leq |L - S|$.

Lanthanide based electroluminescence devices

Until the middle of the first decade in the 21st century, most research concerning lanthanide based electroluminescence (EL) was focused on the "high-voltage" devices [48, 49, 50]. A lanthanide doped wide band gap III-V semiconductor layer with a thickness of 0.5 - 1 μm was sandwiched between two dielectric layers (e.g. Al_2O_3 [48]). Applying a high-voltage high-frequency power (usually in the magnitude of 100 V and 10 kHz) onto both dielectric layers, breakdown of the lanthanide containing semiconductor layer occurs. Hot electrons accelerated thereby impact the lanthanide ions and excite their $4f$ ground state electrons (hot carrier impact excitation). The required electric field is typically greater than 1 MV/cm. Although one may use the Schottky contact to significantly reduce the breakdown voltage and therefore the "turn-on" voltage [51], the emission efficiency is still fairly low. The small cross-section of lanthanide ions for impact excitation and the limitation on the maximum achievable doping concentration are insurmountable obstacles to optimise the efficiency.

In comparison to this, electron-hole recombination is a more efficient and promising way for the lanthanide excitation. With similar structure and fabrication procedures to conventional LEDs, lanthanide ions are doped in the active region of III-V LEDs. A DC voltage as low as 3 V is adequate to obtain a bright emission [52, 53]. However, the resulting luminous efficacy is not sufficient to outrange the other types of LED introduced in the previous section. And the present progress in the enhancement of the lanthanide emission intensity has been rather slow hitherto. This is not at least due to the fact that

a detailed explanation of this excitation mechanism is still missing. The related electron processes are complicated and vary with the systems to be considered. In general, non-radiative transfer of the energy released by carrier recombination to lanthanide emission centres is thought to play a dominant role. Latest results indicate that this energy transfer may be strongly influenced by intentional and unintentional crystal defects, either positively or negatively [54].

1.3 Aims of this work

The central task of present work is to find a systematic strategy to obtain the lanthanide emission and increase its intensity. The study focuses on the photoluminescence (PL) of Pr, Sm, Tb and Tm ions, because the corresponding excitation mechanism is comparable with the one of EL in lanthanide doped LED. III-nitride semiconductor layers, AlN and $Al_x In_{1-x} N$, are selected as host materials. Following a compendious introduction on the techniques applied for sample preparation and characterisation (chapter 2), the intrinsic conditions for occurrence of lanthanide intra-$4f$ transitions are reviewed in chapter 3. With the help of crystal field theory and computer-assisted fitting procedure on our low-temperature PL results, the local symmetry and lattice location of radiative lanthanide dopants in AlN host are ascertained. In chapter 4, thermal enhancements of lanthanide luminescence intensity are investigated and modelled. Some collateral effects, especially the correlation between luminescence intensity originated from lanthanide centres and O-associated defect complex, are also discussed. Taking this as inspiration, the band structure of $Al_x In_{1-x} N$ is modified in order to resonantly excite lanthanide luminescence centres. This is achieved through engineering the size of In-rich $Al_x In_{1-x} N$ nanoparticles, which arise from decomposition. Discussions on the thermodynamics and kinetics of the spinodal decomposition in $Al_x In_{1-x} N$ system as well as the resonant excitation of Tm and Pr luminescence centres are highlighted in chapter 5.

Chapter 2

Sample preparation and characterisation techniques

In this chapter, all of the techniques adopted in this work for sample preparation, thermal treatment and characterisation as well as the relevant principles and parameters are itemised and briefly presented.

The lanthanide doped AlN and $Al_xIn_{1-x}N$ layers were deposited by the use of reactive magnetron co-sputtering technique (section 2.1). Thereafter they were respectively annealed in a furnace at different temperatures and durations (section 2.2) to activate the lanthanide luminescence centres and thus enhance the luminescence intensity. Crystallographic structures of the layers were investigated by X-ray diffractometry (XRD). Microscopic images up to atomic resolution were obtained by transmission electron microscopy (TEM). Furthermore, results of electron energy loss spectroscopy (EELS) and high-angle annular dark field (HAADF) imaging, which are embedded in scanning transmission electron microscopy (STEM), provide qualitative information about the chemical contents of the layers (section 2.3). In order to determine the chemical concentration more accurately, inductively coupled plasma optical emission spectroscopy (ICP-OES) was used. This technique, however, is incapable to analyse the anionic components, namely nitrogen and oxygen. Hence, we employed physical analytic methods, including X-ray photoelectron spectroscopy (XPS), energy-dispersive X-ray spectroscopy (EDS) and Auger electron spectroscopy (AES), to characterise them (section 2.4). The band gap energy of AlN and $Al_xIn_{1-x}N$ hosts were determined through measuring the optical absorption in a UV-Vis spectroscope. Finally, elaborate studies on lanthanide luminescence and its excitation mechanisms were conducted by means of photoluminescence spectroscopy (PL) operated at room temperature and under cryogenic conditions (section 2.5).

2.1   Sample deposition

Sputtering is understood as a process in which atoms are ejected from their solid state through bombardment of energetic particles. It is a conventional physical vapour deposition (PVD) technique and often used in the thin film fabrication.
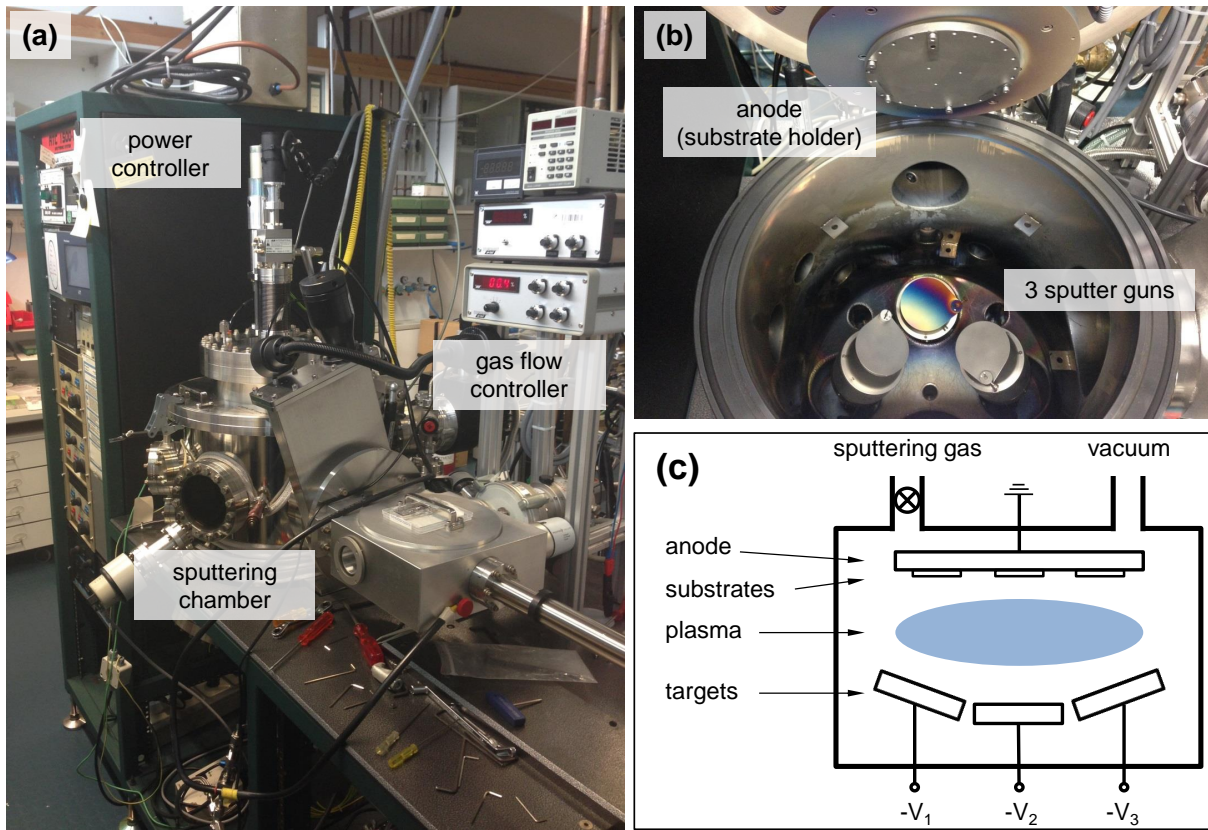
Figure 2.1: (a) Sputtering apparatus (ATC 1500-F) used in this work, (b) its chamber set-up and (c) schematic of a simplified DC sputtering system.

The chamber of the direct current (DC) sputtering apparatus used in this work, ATC 1500-F (AJA International Inc.), is equipped with a pair of parallel electrodes (as illustrated in figure 2.1). Target materials with diameter of 2 inches are placed on the top of cathodes, which are connected to the negative pole of a DC power supply of several kilovolts typically. The substrates are fixed to the anode. Switching on the power supply, stray electrons between the electrodes are accelerated towards the anode. If they uptake sufficient kinetic energy, the neutral process gas atoms can be positively discharged by collision (Townsend discharge). Subsequently, the electric field drives these gas ions towards the target. The metallic atoms and/or ions bombarded out of the target surface fly through the discharge region and finally condense on the substrate surface.

In order to deposit non-metallic layers, including oxides, nitrides, carbides, sulfides, oxycarbides and oxynitrides, a reactive process gas or a mixture of reactive and inert gas must be filled in the chamber. With elaborate adjustment of the sputtering parameters (sputtering power, gas pressure etc.) metallic atoms and/or ions sputtered from the target react with the gas and build a compound layer on the substrate. In case of III-nitride deposition, nitrogen serves as active process gas. The corresponding chemical reaction is therefore:

$$2\,M + N_2 \longrightarrow 2\,MN,$$
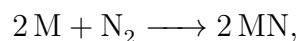
where M stands for the metallic elements.

In the present work, the lanthanide doped AlN and $Al_x In_{1-x} N$ layers were deposited

through reactive magnetron co-sputtering at room temperature onto single crystalline sapphire (orientation: (0001), size 10×10 mm, producer: CrysTec GmbH) and silicon substrates (orientation: (100), diameter 4 inch, producer: CrysTec GmbH). They were clamped on the substrate holder (anode), which rotated at a speed of 10 rpm during the sputtering. Before each sputtering process, the chamber was heated at 120 °C for 12 hours to reduce the moisture and then evacuated by a turbo-molecular vacuum pump until a pressure of 4 - 7 $\times 10^{-7}$ mbar was reached. Subsequently the targets were sputtered by Ar ions (purity 6N, pressure: 3.2 $\times 10^{-3}$ mbar) with the power of 100 W for 10 minutes. This procedure removes the impurities and absorption layer on the target surface. After re-evacuation the reactive process gas, nitrogen with the purity of 6N, was filled into the chamber.

To produce AlN:Ln layers we applied two Al Targets and one lanthanide target as material source whereas in the case of $Al_xIn_{1-x}N$:Ln, three targets, namely Al, In and selected lanthanide, were used. Concentration of the metallic components could be purposefully achieved by elaborate adjustment of sputtering power on each target. The AlN content of $Al_xIn_{1-x}N$ layer, x_{AlN}, depends on the ratio of the power applied on Al target to that on In target. According to our pre-tests, however, the sputtering power was limited between 1 - 250 W. With higher power, the chemical reaction has a higher probability to form a nitride layer on the target surface, which impairs further sputtering (target poisoning). On the other hand, with lower power, ionised nitrogen is energetically insufficient to eject target materials. This limitation of sputtering power restricts the attainable composition range of $Al_xIn_{1-x}N$. Figure 2.2 (a) shows that even with the power limits (Al: 250 W, In: 1 W) the Al content of the resulting $Al_xIn_{1-x}N$ layer is still lower than 0.85.

This problem could be solved by replacing the In target by a second Al Target, on which two In wires with the diameter of 2 mm were placed. Setting the sputtering power of the other pure Al target as 250 W, we obtained an almost linear dependence of the Al content on the power of the Al/In mixed target (see figure 2.2 (b)). By using this setup, we were
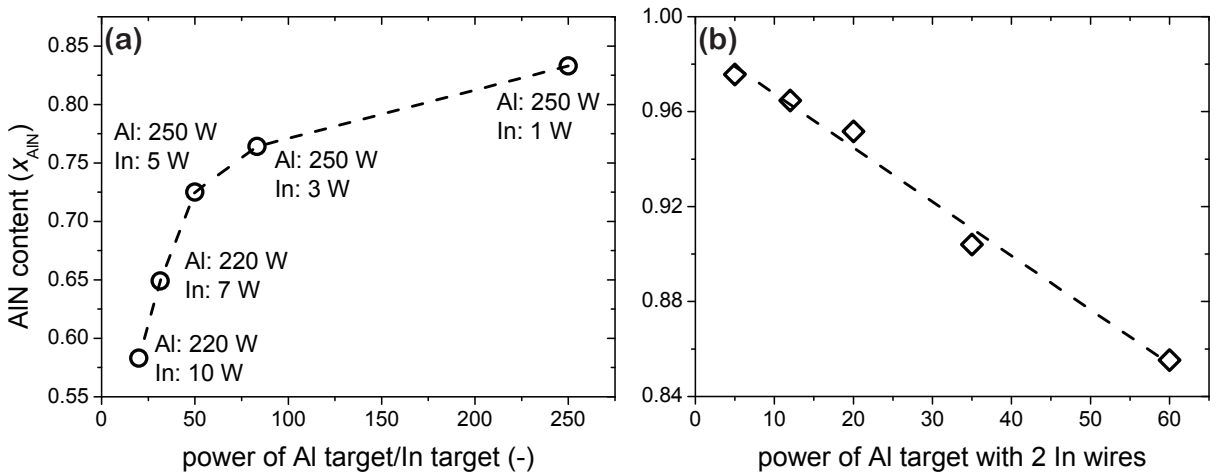
Figure 2.2: (a) Relationship between AlN content of $Al_xIn_{1-x}N$:Ln layer and quotient of sputtering power on Al target against that on In target. Values of applied powers are labelled on the diagram. (b) Relationship between AlN content of $Al_xIn_{1-x}N$:Ln layer and sputtering power of the Al target with two In wires. Power of the other Al target is set to be 250 W.

able to produce the $Al_xIn_{1-x}N$ layers in the whole composition range[1].

After deposition, the layers on the Si wafers with diameter of 4 inches were cut by a diamond saw into smaller samples with the dimension of 10×10 mm, and then cleaned successively with distilled water and ethanol for several times.

Detailed sputtering parameters for the AlN:Ln (Ln = Pr, Sm, Tb and Tm), $Al_{0.87}In_{0.13}N$:Tm and $Al_{0.84}In_{0.16}N$:Pr layers investigated in this work can be found in the table A.1 of appendix A. The purities and manufacturer of the target materials are listed in table 2.1.

Table 2.1: Purities and manufacturer of the target materials.

Material	Pr	Tm	Sm	Tb	Al	In	In wire
Prurity	3N	4N	3N	3N	5N5	5N	4N
Producer		Evochem	MacTeck		Kurt J. Lesker		-

2.2   Thermal annealing treatments

As will be further discussed in chapter 4, in order to activate the lanthanide luminescence centres and therefore to enhance their luminescence intensity, a heat treatment is required. AlN:Ln and $Al_xIn_{1-x}N$:Ln layers deposited on Si substrates were thermally annealed in a quartz tube furnace (figure 2.3 (a)). The layers carried in an Al_2O_3 crucible were placed in the quartz tube. A pumping system consisting of a pre-vacuum pump and a turbo-molecular pump provides a base pressure of about 7×10^{-5} mbar. After this, nitrogen protecting gas was filled in the tube with calculated pressure, which ensures that it reaches approximately 1 bar during the annealing at elevated temperatures. Once the furnace was pre-heated to desired temperature, the quartz tube was shifted into it. After annealing, the tube was taken out of the furnace and air-cooled to room temperature.

For AlN:Ln layers, 11 samples from each kind of lanthanide dopants were selected and respectively annealed at 150 °C, 300 °C, 400 °C, 500 °C, 600 °C, 700 °C, 800 °C, 850 °C, 900 °C, 950 °C and 1000 °C for 30 minutes. It must be further noticed that after insertion of the cold quartz tube, the furnace temperature dropped about 50 to 100 °C, and took around 5 minutes to rise back to the desired temperature. The air-cooling process usually lasts about 20 minutes.

In order to study the kinetics of thermal activation of lanthanide luminescence centres in AlN:Ln layers (cf. chapter 4) and the coarsening of In-rich $Al_xIn_{1-x}N$ nanoparticles resulted from decomposition in $Al_xIn_{1-x}N$:Ln layers (cf. chapter 5), a precise control of annealing duration is required. To achieve this, the layers were encapsulated within quartz phial under nitrogen atmosphere (figure 2.3 (b)). After pre-heating of a conventional furnace, quartz phials were put into holes of sample holder made of cast iron (figure 2.3

---

[1] It needs to be noticed here, that the line plotted in figure 2.2 (b) is a guideline with less accuracy for the sample preparation. Other factors, for example the position of In wires, will influence the In concentration as well. Hence the exact values of AlN content of as-prepared $Al_xIn_{1-x}N$ layer must be determined by other ways as introduced in section 2.4.
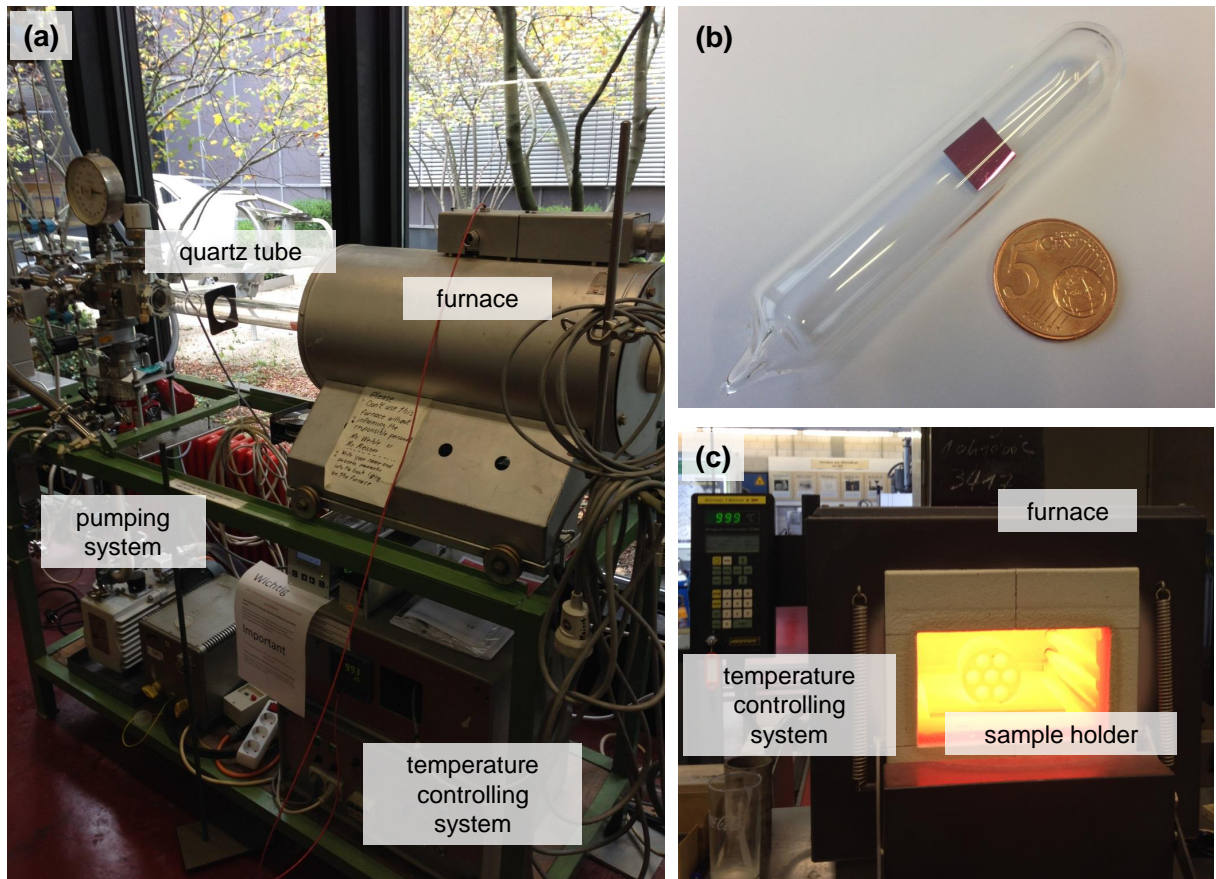
Figure 2.3: (a) Quartz tube furnace, (b) an $Al_{0.87}In_{0.13}N$:Tm layer in quartz phial and (c) the furnace used in this work to anneal the encapsulated layers.

(c)). There is no information about the factual heating rate of encapsulated layers. But considering to the small volume of phial we can expect that the time of the heating stage is negligible. After thermal annealing the quartz phials were quenched in iced water. The applied annealing temperatures and durations are listed in table A.2 of appendix A.

2.3 Structural characterisation

2.3.1 X-ray diffraction

θ-2θ-method

X-ray diffractometry (XRD) is a standard method to identify the crystal structure. The sample surface is irradiated thereby with a monochromatic X-ray beam. If the incident beam angle θ, distance between the lattice planes of the sample d and the wavelength of incident X-ray λ satisfies the Bragg's law

$$n\lambda = 2d\sin\theta, \tag{2.1}$$

constructive interference occurs. n is an integer determined by the order of diffraction. The instrument employed in this work was the diffractometer D5000 manufactured by

Siemens AG with a Cu X-ray source. With a Ni foil the Cu-K_α radiation is filtered and used for the measurement. The radiation source and the detector are mounted on a Bragg-Brentano diffractometer, wherein they can move independently. In order to establish a diffractogram, the intensity of diffracted X-rays were measured (with step size $\Delta 2\theta = 0.02$) and plotted against 2θ (θ-2θ-method). By comparing the results with the reference card from the database of the International Centre for Diffraction Data (ICDD), number 00-25-1133, we ensure that at room temperature AlN and $Al_xIn_{1-x}N$ layers exhibit the hexagonal wurtzite structure (cf. figure B.2 of appendix B).

Once the distances between certain lattice planes of a hexagonal crystal system (hkl), d_{hkl}, are determined by using equation 2.1, its lattice parameters a and c can be calculated by

$$\frac{1}{d_{hkl}^2} = \frac{4}{3}\left(\frac{h^2 + hk + k^2}{a^2}\right) + \frac{l^2}{c^2}. \tag{2.2}$$

$\sin^2 \Psi$-method

For more accurate determination of the lattice parameters, the influences of the biaxial elastic internal stress $\sigma_\parallel$ should be taken into account. It is often introduced during the layer deposition and thermal treatment. In case of a polycrystalline sample with a random crystal orientation, the changes of a considered plane distance due to internal stress depend on its orientations with respect to the sample surface. Measuring an individual lattice plane distance d_Ψ under variation of the tilting angles Ψ, it follows:

$$d_\Psi = d_0 \frac{1+\nu}{E}\sigma_\parallel \sin^2 \Psi + d_0\left(1 - \frac{2\nu}{E}\right), \tag{2.3}$$

where ν is the Poisson's ratio, E the Young's-modulus and d_0 the stress-free plane distance. In this work, XRD measurements using above mentioned $\sin^2 \Psi$-method were taken by X'Pert MR diffractometer (PANalytical B.V.). (100), (002) and (101) reflexes of AlN:Pr and $Al_{0.84}In_{0.16}N$:Pr layers before and after annealing were measured with tilting angles $\Psi = 5°$, $20°$, $30°$, $40°$, $55°$, $65°$ and $75°$. Results of the stress-free lattice parameters and the elastic internal stress are presented in figure 5.4 (chapter 5) and table B.2 and B.3 (appendix B).

2.3.2 Transmission electron microscopy

Bright field (BF) imaging

The microstructures of AlN:Ln and $Al_xIn_{1-x}N$:Ln layers were observed via transmission electron microscopy (TEM). Using a tripod polisher and a subsequent ion milling the cross-sections of the selected layers were thinned to about 20 nm, so that the electron beam is able to transmit through it. Contrast in the TEM images is formed by the Coulomb interaction between the incident electrons and the atoms in TEM sample. In the bright field (BF) mode only the transmitted electrons, which are not (and merely slightly) scattered by the sample, are detected (see figure 2.4 (a)). The resulting image represents a two dimensional projection of the sample along the optical axis.
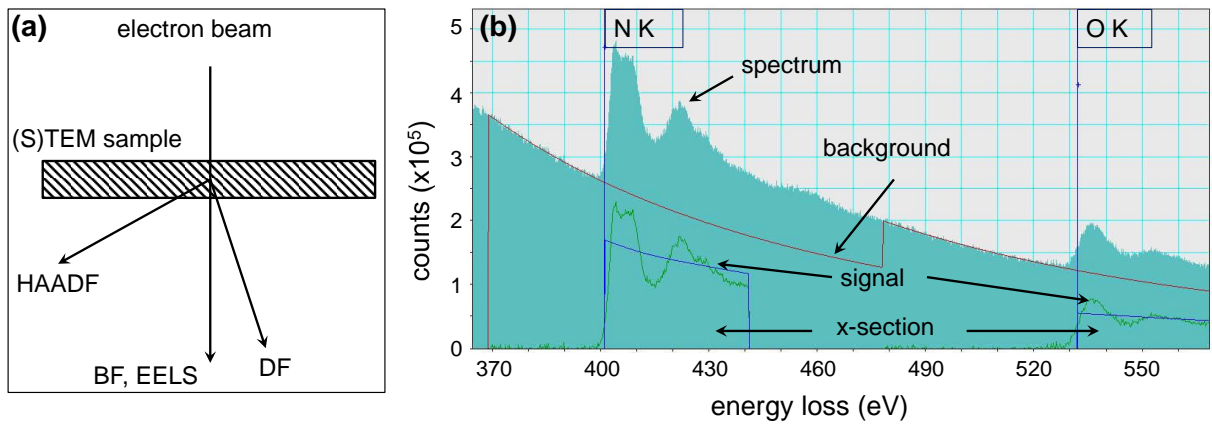
Figure 2.4: (a) Sketch of the transmitted electrons detected for TEM bright filed (BF), dark filed (DF) and high-angle annular dark field (HAADF) imaging as well as elemental mapping by electron energy loss spectroscopy (EELS). (b) Example of an EELS spectrum detected in this work for the nitrogen and oxygen mapping.

The resolution of TEM images depends on the accelerating voltage. The instrument applied for high resolution TEM (HRTEM) investigations was a 4000FX manufactured by JEOL Ltd.. It has an accelerating voltage of 400 kV. Thereby the atomic structures of the layers can be easily identified.

High-angle annular dark field (HAADF) imaging

If the incident electrons interact with the atoms of the TEM sample, they will be scattered either elastically or inelastically. In the former case, electrons are deviated from their original trajectory. By using the dark field (DF) mode of TEM, only this part of electrons is detected. In contrast to conventional DF imaging, the scattering angles of incoherently scattered electrons are much higher (figure 2.4 (a)) and depend on the atomic number Z of atoms in the sample. Scanning the sample with a focused electron beam (STEM) and combining the two-dimensional coordinates and the signal of the scattered electrons collected by a high-angle annular dark field (HAADF) detector, a Z-contrast image (HAADF image) is produced.

In this work we applied a SESAM microscope (Sub-Electron-volt Sub-Angstrom Microscope, with accelerating voltage of 200 kV) produced by Carl Zeiss AG to analyse the formation of Al-rich and In-rich $Al_xIn_{1-x}N$ phases after decomposition (see chapter 5).

Electron energy loss spectroscopy (EELS)

Unfortunately the HAADF technique is incapable of identifying the light elements with atomic numbers close to each other. In order to study the nitrogen and oxygen distribution in the AlN:Ln layers (chapter 4) we used an electron energy loss spectroscope (EELS), which is assembled in a 912 Omega microscope with accelerating voltage of 120 kV (Carl Zeiss AG).

During electron penetration, the kinetic energy of electrons is partially absorbed by the atoms in the sample and is used to ionise their core electrons (inelastic scattering). The

energy lost thereby is element characteristic. As shown in figure 2.4 (b), electrons with an energy loss due to K-shell ionisation of nitrogen and oxygen are detected in the EELS elemental mapping.

2.4   Compositional characterisation

2.4.1   Chemical analysis

In order to obtain a higher luminescence of lanthanide ion as well as to avoid its concentration quenching, doping concentration must be restricted within a proper range. Furthermore, as will be discussed in chapter 5, the concentration of In in $Al_x In_{1-x}N$:Ln layers plays a dominant role on the shape and size of In-rich $Al_x In_{1-x}N$ phase after decomposition at adequate annealing temperature. Thus, it is very important to characterise the average layer composition as accurately as possible.

Inductively coupled plasma optical emission spectroscopy (ICP-OES) is an appropriate technique for this purpose. Samples of identical size were thereby dissolved in concentrated acids and filled in 10 mL volumetric flask respectively. For AlN:Ln layers, we used a mixture of 500 mL HCl and 100 mL HNO_3 as disolvating agent. And the reaction was kept at 125 °C. In case of $Al_x In_{1-x}N$:Ln, the procedure was more complicated: At first, they were partly dissolved in a mixture of 500 mL HCl and 200 mL HNO_3. And subsequently the acids were evaporated at 175 °C. In order to completely dissolve the layer we further added 500 mL H_2SO_4. As soon as the reaction completed, the solution was heated at 325 °C to remove the H_2SO_4 and finally 500 mL HCl was filled. By using the device "Ciros CCD" (SPECTRO Analytical Instruments GmbH) the solution was injected as an aerosol into the argon plasma, which is inductively heated to 5000 - 7000 °C. The ions to be measured were excited and the resulting element characteristic radiation was detected by a CCD detector. Peak intensity of this optical emission spectrum is linearly proportional to the number of ions. Hence, through comparing the experimental results with the reference spectra of standard solutions one obtains the information about chemical composition of the layers. The results are presented in the following chapters and in table B.1 of appendix B.

It is noteworthy to mention that, due to the utilised disolvating agent, non-metallic components (nitrogen and oxygen) of the layers are unable to be determined by ICP-OES. This shortcoming calls for other analytic methods, which may deliver less accurate but more comprehensive compositional information, as introduced in the next subsection.

2.4.2   Physical analysis

Physical analytic methods, including Auger electron spectroscopy (AES), energy-dispersive X-ray spectroscopy (EDS) and X-ray photoelectron spectroscopy (XPS), were adopted in this work as alternative means to determine the chemical concentration of AlN:Ln and $Al_x In_{1-x}N$:Ln layers. These methods are based on the inelastic interaction between incident electrons or photons and shell electrons of the elements to be measured.
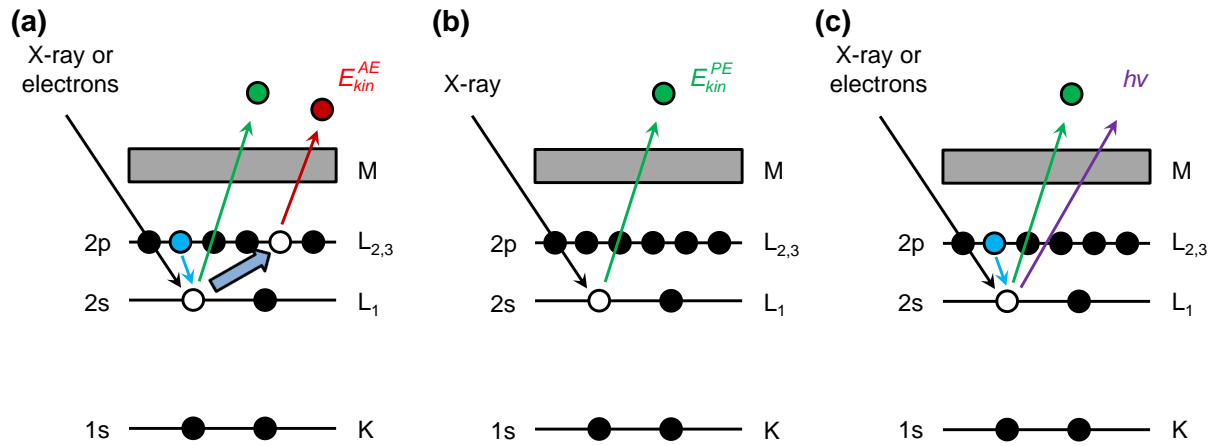
Figure 2.5: Schematic illustration of the processes to produce (a) Auger electron in AES, (b) photoelectron in XPS and (c) characteristic X-ray in EDS (black: incident beam, green: primarily emitted electron, blue: secondary electron, red: Auger electron and purple: emitted X-ray).

Auger electron spectroscopy (AES)

Through bombardment with high-energetic photons or electrons, atoms in the layer are able to be ionised and emit electrons from the inner shell. The ionisation energy is not less than the energy of this electron shell respective to the vacuum level E_1^{AE}. The remaining electron vacancies are unstable and can be occupied by electrons relaxed from an outer shell (with the energy relate to vacuum: E_2^{AE}). Energy released thereby may subsequently transferred to other electrons (with the energy relate to vacuum: E_3^{AE}) and eject them out of the atoms (figure 2.5 (a)). This third electron is named as Auger electron. By using AES, Auger electrons of the sample are generated and their kinetic energies $E_{kin.}^{AE}$ are detected. They are element specific and depend on all of the relevant electron shell energy in this process as:

$$E_{kin.}^{AE} = E_1^{AE} - E_2^{AE} - E_3^{AE} - \Phi_{WF},\qquad(2.4)$$

where Φ_{WF} represents the work function of the analyser.

X-ray photoelectron spectroscopy (XPS)

The core-shell electrons, which are escaped from the sample surface through irradiation by high-energetic photons $h\nu$, are called photoelectrons (figure 2.5 (b)). By means of XPS one measures the kinetic energy of the photoelectrons $E_{kin.}^{PE}$ and calculates the corresponding binding energy E_B^{PE} according to

$$E_B^{PE} = h\nu - E_{kin.}^{PE} - \Phi_{WF},\qquad(2.5)$$

which provides the information about the chemical components of the sample.

Energy-dispersive X-ray spectroscopy (EDS)

If the shell electrons are excited and escaped from the sample, energy released by filling the vacancies could not only generate Auger electrons, but also can be dissipated in the form of X-rays ((figure 2.5 (c))). The resulting X-ray spectrum recorded by EDS is characteristic for each element. And the chemical components of the sample are distinguishable.

Calculation of chemical compositions

Chemical composition of the layer can be calculated from the AES, EDS or XPS spectra quantitatively. The atomic fraction of element A in a n-component system, x_A for example, is determined as

$$x_A = \frac{I_A/C_A}{\sum_{i=1}^{n}(I_i/C_i)}, \tag{2.6}$$

where I_i and C_i denote the spectral intensity of i-th component and a characteristic constant, which takes (depending on the applied method) the instrumental sensitivity, the sensitivity factor of i-th component and the inelastic mean free path.

In the present work, we used an AES instrument JAMP-7830F (JEOL Ltd.) and the XPS system Theta Probe (Thermo VG Scientific) to characterise the chemical concentrations of AlN:Ln and $Al_x In_{1-x} N$:Ln layers, in particular their non-metallic components. In the AES the layer surface can be gradually removed through bombardment of inert ions. Since the interaction volume of Auger electrons is fairly small, one is able to receive a detailed compositional depth profile (see figure B.1 in appendix B as example). The EDS detector is installed in a dedicated STEM (in this work: SESAM). It permits us to determine the chemical concentration within selected regions (EDS line scan and point measurement as shown in chapter 5).

2.5 Optoelectronic characterisation

2.5.1 Optical transmission spectroscopy

In an optical transmission spectroscope, AlN:Ln and $Al_x In_{1-x} N$:Ln layers deposited on transparent sapphire substrates were irradiated by a monochromatic light with continuously varied wavelength. Intensity of the light $I(x)$ passing through the layer of thickness x is recorded. If the light is absorbed by the layer due to e.g. band-band transition and/or excitation of defect levels within the band gap, $I(x)$ reduces with respect to the incident intensity I_0. A transmission coefficient T is defined as the ratio of the transmitted and the incident intensity to describe the intensity attenuation. And the Lambert's law

$$T = \frac{I(x)}{I_0} = \exp(-\alpha x) \tag{2.7}$$

is used to calculate the absorption coefficient α. The band gap energy E_g and Urbach energy E_U of AlN:Ln and $Al_x In_{1-x} N$:Ln layers were in this work directly determined via graphic fitting on a plot of the absorption coefficient α versus photon energy $h\nu$ by using
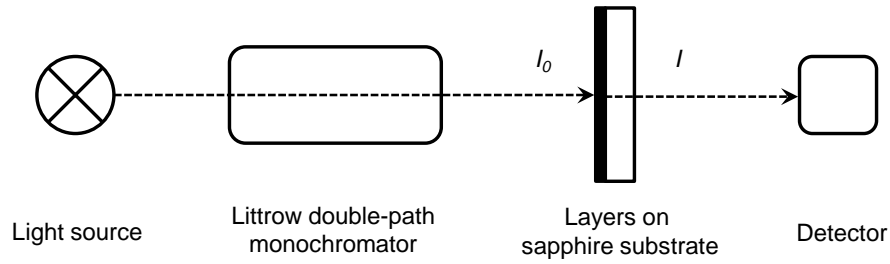
Figure 2.6: Sketch of the beam path in the device Cary 5000.

the equations:

$$\alpha = K_g(h\nu - E_g)^{\beta} \qquad \text{for } h\nu \geq E_g, \text{ and} \tag{2.8a}$$

$$\alpha = K_U \exp\left(\frac{h\nu - E_g}{E_U}\right) \qquad \text{for } h\nu \leq E_g, \tag{2.8b}$$

where K_g and K_U are independent constants and the exponent $\beta = 0.5$ for direct semiconductors [55]. An example of the fitting curves is shown in figure B.3 (a) of appendix B.

The optical transmission measurements in present work were carried out at room temperature by using the device Cary 5000 UV-VIS-NIR absorption spectrometer (Agilent Technologies Inc.) with a deuterium arc lamp and visible QI lamp as light source (figure 2.6). The radiation wavelength was filtered by a Littrow double-path monochromator and set to be gradually decreased from 800 nm to 200 nm (1.55 - 6.20 eV) with a scanning-interval of 1 nm per 0.1 second. The transmitted intensities were recorded by a PbS detector and plotted against the wavelength. In order to eliminate the disturbing influences of light reflection and absorption by the sapphire substrate as well as the general absorption along the whole beam path, a transmission spectrum of the sapphire substrate without any deposited layer was taken as a reference.

2.5.2 Photoluminescence spectroscopy

Room temperature photoluminescence spectroscopy (PL)

By means of photoluminescence (PL) spectroscopy the samples are excited by a monochromatic light and the resulting luminescence intensity is detected and plotted against its wavelength or photon energy.

The room temperature PL studies of this work were operated by a Fluorolog-3 FL3-22 (Horiba Jobin Yvon GmbH) spectrometer with a xenon arc lamp as light source (see figure 2.7 (a) and (b)). The spot of excitation light is about 10 mm high and 3.8 mm wide. In order to homogenously radiate AlN:Ln and $Al_xIn_{1-x}N$:Ln layers with the dimension of 10 ×10 mm, layers were placed on the sample holder with an angle of 67.5° between their surface normal and the excitation light (corresponds to the right-angle (RA) mode of spectrometer, see figure 2.7 (c)). By means of two double-grating monochromators we were able to adjust the excitation light and measure the PL spectrum in a broad wave-
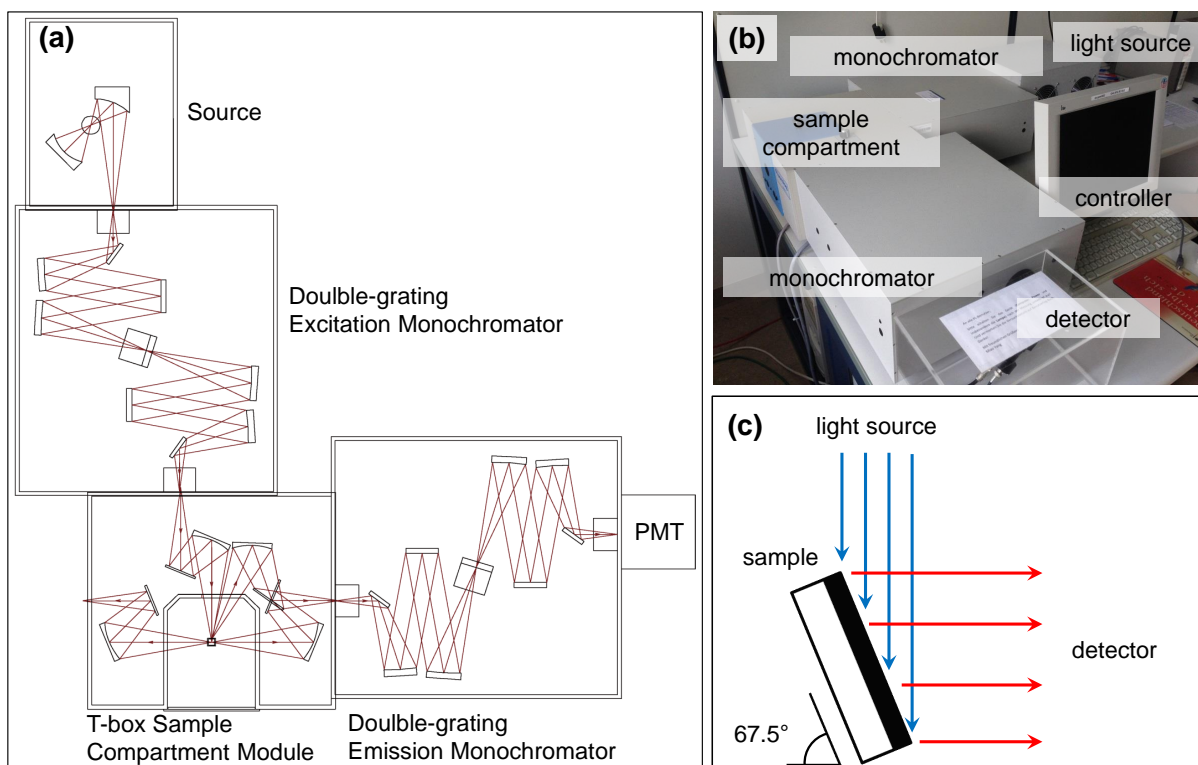
Figure 2.7: (a) Sketch of the optical path and (b) constitution of the PL spectrometer (Fluorolog-3 FL3-22) used in this work. (c) Sketch of the layer installation at the RA scanning mode.

length range[2]. Luminescence intensity was measured by a photomultiplier tube (PMT). The applied excitation wavelengths/energies are noted in the captions of the spectral results shown in the following chapters. If not otherwise mentioned, band pass of 4 nm was chosen both for excitation and emission. And the PL spectra were taken with a measuring rate of 1 nm per second.

Room temperature photoluminescence excitation spectroscopy (PLE)

The measurement principle of a photoluminescence excitation (PLE) spectroscopy is a reverse process of a PL measurement. Instead of monochromatic excitation, the wavelength of the incident light to the layer varies continuously. And the intensity of a selected luminescence is recorded and plotted against the excitation wavelength or energy. Through analysing the peak positions in PLE spectra, energy levels, which are related to this luminescence, are able to be identified.

The apparatus, band pass and scanning rate used for PLE spectroscopy are the same as the room temperature PL measurement. It must be emphasised that the raw PLE data are sometimes misleading when used without any corrections. This is on the one hand due to the fact that the intensity of xenon lamp alters significantly by changing its radiation wavelength (see figure 2.8 (a)). On the other hand, the PLE spectra monitored at the characteristic lanthanide luminescence contain integrated information consisting of lanthanide luminescence, defect luminescence of host material and back-ground signals.

---

[2] excitation range: 230 - 800 nm (5.39 - 1.55 eV); detection range: 240 - 850 nm (5.17 - 1.46 eV)
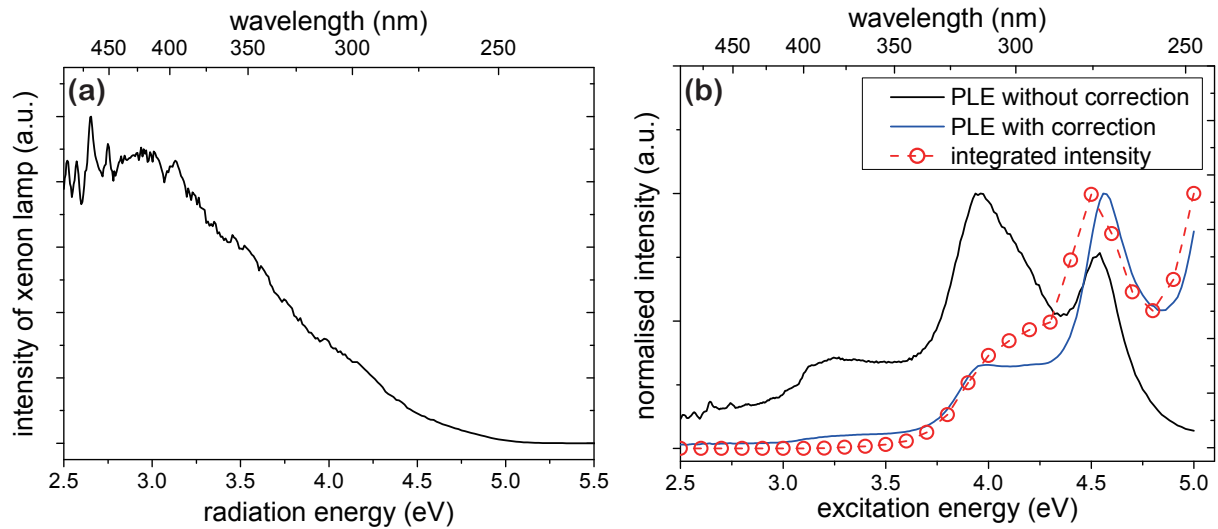
Figure 2.8: (a) Emission spectrum of the xenon lamp used for room temperature PL and PLE investigations in this work. The lamp outputs were measured by a photodiode. (b) Normalised PLE spectrum of a AlN:Tb layer (monitored at 543 nm, corresponds to $^5D_4$ - $^7F_5$ transition) after 30 minutes annealing at 500 °C with and without lamp correction (blue and black line respectively) and the plot of the integrated luminescence intensity originated from intra $4f$-transitions of Tb ions (red dashed line with circles).

Based on the low pumping property of the xenon lamp for the excitation of lanthanide luminescence centres in AlN [56], we corrected the PLE data of this work with the assumption, that the luminescence intensity depends linearly on the lamp output. And in order to obtain a more accurate PLE spectrum for lanthanide emission, PL spectra were firstly taken by using different excitation energy (with energy interval of 0.1 eV). After this, we subtracted the back ground signals, integrated the area below every lanthanide luminescence peaks, corrected the results with lamp output and then plotted then against the excitation energy. As can be seen in figure 2.8 (b), the signal disturbances are eliminated by using this treatment.

Low temperature PL spectroscopy

As will be analysed in the next chapter, the splitting of lanthanide luminescence peaks due to crystal field perturbation can be only observed under cryogenic conditions. After 30 minutes annealing at 1000 °C the AlN:Sm and AlN:Tb layers were cooled down to about 10 K by a Helium-flow cryostat. An ArF exciplex laser with wavelength of 193 nm (6.42 eV) served as excitation light source. The resulting luminescence was filtered by a grating monochromator with 1 m focal length and detected by a back-illuminated CCD camera.

Thereby, two kinds of diffraction grating with groove density 1200 and 2400 g/mm were available. They provide a spectral resolution of about 0.012 nm in the detection range from 340 nm to 800 nm (3.65 - 1.55 eV).

Chapter 3

Lanthanide luminescence and architecture of neighbour ions - Crystal Field Theory

In quantum mechanics, a transition $\langle \Psi_i | \hat{O} | \Psi_f \rangle$ is non-vanished, if Γ, the symmetry of the transition operator $\hat{O}$, is contained in the direct product of $\Gamma_i \otimes \Gamma_f$, where Γ_i and Γ_f are symmetric irreducible representations of initial and final states, Ψ_i and Ψ_f, respectively. In case of lanthanide ion under a centrosymmetric electrostatic field, all of the induced intra-$4f$ electric dipole transitions (ED transitions) are forbidden, because the parities of its initial and finale state are identical and the ED operator has an ungerade parity (u or -) (Laporte selection rules [57]). Although the intra-$4f$ magnetic dipole transitions (MD transitions, with gerade operator parity g or +) are allowed, their transition strength is however generally 5 magnitudes lower than the former one [58]. In order to observe intra-$4f$ transitions, the lanthanide ions should be in general located in crystal surroundings with a non-centrosymmetric point group. Thereby, States of $4f^n$-configuration are mixed by $4f^{n-1}5d$-states with opposite parity. [59, 60]. The electrostatic field, which arises from the surrounding ions and interacts on the central lanthanide ion, is named as crystal field. Due to limited solid solubility [61] and luminescence concentration quenching [62, 63], concentration of lanthanide dopants in a crystalline host can only be kept in the range of several atomic percent. The small amount of lanthanide dopant complicates the determination of its lattice location by using conventional electron beam based microscopic methods. Additionally, the polycrystalline nature of deposited layers in this work makes other techniques, such as ion beam channelling or emission channelling, practically impossible. The crystal field theory is, on the other hand, a convenient instrument not only for the theoretical calculation of the electron fine structure [64], but also for the determination of the lanthanide site location with the help of available experimental investigations [65, 66]. Furthermore, analysis based thereon may be the only way so far to characterise the local symmetry of radiative lanthanide ions in a polycrystalline host.

In the first part of this chapter (section 3.1) perturbations by the crystal field on a multi-electron system will be briefly overviewed. Subsequently we use Sm^{3+} and Tb^{3+} as probes to identify their local symmetry in AlN. The corresponding experimental results and dis-

cussions are shown in section 3.2.

3.1 Influences of crystal field interactions on lanthanide $4f$-electrons

The crystal field (CF) is considered as an electrostatic perturbation, which is built by
the charge distribution of surrounding ions and interacts with the electrons of the central
ion. In case of lanthanide $4f$-electrons, the CF perturbation is a rather weak interaction
due to screening effects from outer electron shells and thus can only slightly remove
their spin-orbit coupled degeneracy (as already mentioned in section 1.2). Predictions of
this energy level splitting through *ab-initio* calculations, e.g., Hartree-Fock method, are
sometimes in less consistency with experimental results. One of the main reasons is that
the considerations for the calculation are not comprehensive enough, because the physical
processes lying behind are not fully understood [67]. A more common approach in the
practice is to use a semi-empirical method by introducing a crystal field Hamiltonian
operator $\hat{H}_{\mathrm{CF}}$. It contains the parameters relating to the symmetry of surrounding ions,
and can be achieved with the following steps (for more details see reference [67]):

1. *Expression of crystal field Hamiltonian*
   The point charge model is one of the most adequate expressions for the crystal field
   Hamiltonian, where $\hat{H}_{\mathrm{CF}}$ is defined as a summation of crystal field potentials $V(\vec{r}_i)$
   felt by each $4f$ electron of the central lying lanthanide ion:

   $$\hat{H}_{\mathrm{CF}} = -e \sum_{i=1}^{n} V(\vec{r}_i). \tag{3.1}$$

   $\vec{r}_i$ is the position vector of electron i and e the elementary charge. If the crystal field
   perturbation in the considered system is time-independent, $V(\vec{r}_i)$ can be written as
   a summation over all electrostatic potentials, which are produced by surrounding
   discrete point charges $-Ze$ at atomic position vector $\vec{R}_L$ and act on the i-th $4f$
   electron of lanthanide ion:

   $$V(\vec{r}_i) = \sum_{L} \frac{(-Ze)_L}{|\vec{R}_L - \vec{r}_i|}. \tag{3.2}$$

2. *Expansion of the crystal field potential*
   The distance term in equation 3.2, $\frac{1}{|\vec{R}_L - \vec{r}_i|}$, can be expanded by using the *Legendre
   polynomials* and *spherical harmonic addition theorem* [68]. After tedious mathe-

matic treatments one is able to rewrite the crystal field potential as:

$$
\begin{aligned}
V(\vec{r}_i) = \sum_{k=0}^{\infty} \Bigg[& B_0^k C_0^k(i) \\
& + \sum_{q=1}^{k} \left(B_q^k \left(C_{-q}^k(i) + (-1)^q C_q^k(i) \right) + B_q'^k i \left(C_{-q}^k(i) + (-1)^q C_q^k(i) \right) \right) \Bigg],
\end{aligned}
\tag{3.3}
$$

where $C_q^k(i)$ are the tensor operator, which replace the spherical harmonics $Y_k^q(i)$ by

$$
C_q^k(i) = \sqrt{\frac{4\pi}{2k+1}} Y_k^q(i),
\tag{3.4}
$$

Further terms are defined as

$$
B_0^k = \sqrt{\frac{4\pi}{2k+1}} Y_k^0 \sum_L (-Ze)_L \frac{r^k}{R_L^{k+1}},
\tag{3.5a}
$$

$$
B_q^k = \sqrt{\frac{4\pi}{2k+1}} (-1)^q \mathrm{Re}\, Y_k^q \sum_L (-Ze)_L \frac{r^k}{R_L^{k+1}},
\tag{3.5b}
$$

$$
B_q'^k = \sqrt{\frac{4\pi}{2k+1}} (-1)^q \mathrm{Im}\, Y_k^q \sum_L (-Ze)_L \frac{r^k}{R_L^{k+1}}.
\tag{3.5c}
$$

They represent the crystal-field parameters (CF parameters) in Wybourne notation. For $4f$ electrons $k = 0, 1, ..., 7$ are allowed. Because the CF parameters must be invariant after symmetry operations, allowed values of q ($|q| \leq k$) are determined by the local symmetry of the lanthanide ion.

It can be seen from equation 3.3 that the crystal field Hamiltonian consists of three parts:

$$
\hat{H}_{\mathrm{CF}} = \hat{H}_{\mathrm{CF}}^0 + \hat{H}_{\mathrm{CF}}' + \hat{H}_{\mathrm{CF}}'',
\tag{3.6}
$$

the part $\hat{H}_{\mathrm{CF}}^0$ with $k = 0$, which shifts the barycentre of all energy levels and contribute to the nephelauxetic effect [69]; the part $\hat{H}_{\mathrm{CF}}'$ with odd k-values, which mixes $4f^{n-1}5d$-state with opposite parity into $4f^n$-states and is responsible for the strength (namely the intensity) of induced electric dipole transitions [70]; and the part $\hat{H}_{\mathrm{CF}}''$ with non-zero even k-values, which causes the Stark splitting of $4f$-energy levels and J-mixing effect [59, 60]. In order to determine the crystal field splitting and, on this basis, the lattice location of radiative lanthanide ions, only $\hat{H}_{CF}''$ terms are need to be considered.

3. *Diagonalisation of the crystal field matrix element by operator-equivalent method*
   Once the crystal field Hamiltonian is formulated, one can calculate the Stark levels $|\Psi_{l^{n'}\tau'S'L'J'M'}\rangle$ through diagonalisation of crystal-field matrix with the matrix element in form

$$
\left\langle \Psi_{l^n \tau SLJM} \left| \hat{H}_{CF}'' \right| \Psi_{l^{n'}\tau'S'L'J'M'} \right\rangle.
\tag{3.7}
$$

Although it is theoretically possible to calculate the matrix elements in the full Hilbert space from $\hat{H}_{CF}$ in Wybourne notation, only the angular parts of them can be exactly solved [67]. Hence it is more convenient in practice to estimate the CF parameters semi-emperically, and based on this to calculate the corresponding energy positions of the Stark levels. Through comparison with experimentally determined energy levels one can adjust the CF parameters until the differences between calculated and experimental results are minimised.

If the J-mixing effect is negligible[1], one may use a so-called "operator-equivalent method" to obtain an effective crystal field Hamiltonian $\hat{H}_{CF}''^{*}$, which is approximate to the crystal field Hamiltonian [71, 72, 73, 74]:

$$\hat{H}_{CF}'' \approx \hat{H}_{CF}''^{*} = \sum_{q=2,4,6} \sum_{k=-q}^{k=q} a_k A_q^k \langle r^k \rangle \hat{O}_q^k = \sum_{q=2,4,6} \sum_{k=-q}^{k=q} B_q^k \hat{O}_q^k, \qquad (3.8)$$

where a_k are the Stevens coefficients $\langle J||\alpha||J \rangle$, $\langle J||\beta||J \rangle$ and $\langle J||\gamma||J \rangle$ for $k = 2$, 4, 6 respectively, and can be calculated based on the doubly reduced matrix element values [75], $\langle r^k \rangle$ expectations of radial integral of electrons in free lanthanide ion and $\hat{O}_q^k$ the equivalent angular momentum operators, whose expressions can be found in [71, 76]. A_k^q is the CF parameter in Stevens notation and follows:

$$A_q^k = \frac{4\pi}{2k+1} c_{kq} (-1)^k \sum_{i=1}^{N} \frac{Z_i e^2 Y_k^q(\theta_i, \varphi_i)}{R_i^{k+1}}. \qquad (3.9)$$

Here c_{kq} indicates a transformation coefficient, which relates the irreducible operators $C_q^{k}(\theta_i, \varphi_i)$ and equivalent operators $\hat{O}_q^k$, Z_i is the effective point charge of the surrounding ions felt by $4f$-electrons of central lying lanthanide ion and θ_i, φ_i, R_i their polar coordinates.

Over years many experimental studies were performed on spectroscopic properties of trivalent lanthanide ions, which are doped into different crystalline host matrices substitutionally [65, 66, 77, 78, 79, 80]. The CF parameters in Wybourne notation, B_q^k, were determined by direct fitting of optic and magnetic results, inferring the local symmetry of the lanthanide ions in the host. And based on the physical and structural model of undoped host material, the values of B_q^k calculated by operator-equivalent method (equation 3.8 and 3.9) were used as initial set for the fitting procedure. Since the number of non-vanishing CF parameters depend on the local symmetry, this strategy, however, will lead to an immense complexity by analysing the systems of a lower point group. The lower is its symmetry, the more is the total number of CF parameters (e.g. 4 for O_h, 27 for C_1)[2].

---

[1] This effect highly depends on the atomic number of the lanthanide elements, the $4f$-levels to be considered and the local symmetry etc. In General, the J-mixing effect is stronger in "light" lanthanide elements than in the "heavy" ones, stronger at lower $4f$-levels and weaker for higher symmetry.

[2] Although the restriction of a constant B_q^k/B_0^k ratio (because of identical radial part of B_0^k and B_q^k in a given configuration) can be used to reduce the number of variable CF parameters, it may cause additional errors in the fitting procedure. A slight lattice distortion inflicted by lanthanide dopant leads to considerable deviation of the experimentally determined B_q^k/B_0^k ratio from the one predicted by crystal model [81] (as an example see the discussions in section 3.2.2).

More importantly, CF parameters are unobservable quantities and vary with different selections of the Cartesian system. They also imply a variety of other physical factors, which are indistinguishable from the values of the CF parameters. Hence comparing the fitted CF parameters to the references under different assumptions and pre-conditions is confusing and sometimes even misleading for the analysis of the local symmetry of the lanthanide environment.

Very recently E. Coronado and his co-workers [82, 83] had proposed an effective point charge to calculate the CF parameters, so as to fit the ground state Stark splitting of lanthanide ions. The results extracted thereby contain clear physical and structural information, and thus are capable to be used as reference for further studies. In the next section we will also apply this method to find out the site location of radiative lanthanide ions in the AlN host.

3.2 Determination of radiative lanthanide site location in AlN host

As corner stones for the CF analysis, we summarise in section 3.2.1 the possible substitutional and interstitial sites of lanthanide ions in the AlN matrix as well as the corresponding spectra assignment and selection rules of transitions between Stark levels with the help of references elsewhere. In section 3.2.2, the energy positions of the Stark levels in the multiplets ^5H_J ($J = 5/2$, $7/2$, $9/2$ and $11/2$) of Sm^{3+} ($4f^5$) are precisely identified through PL measurements at low temperature. We attempt for the first time to estimate the effective point charge of nitrogen ions felt by Sm^{3+} and their polar coordinates. Even though the fitting procedure was less satisfied for Tb^{3+} ($4f^8$), its local symmetry is still able to be determined by spectra analysis in section 3.2.3.

3.2.1 Physical and structural considerations on lanthanide site in AlN

Substitutional site

XRD and TEM results in present work (see figure B.2 in appendix B and figure 4.4 in chapter 4) as well as our previous studies [63, 84, 85, 86] indicate that the AlN:Ln layers produced by reactive co-sputtering exhibit columnar grains with wurtzite structure (w-AlN, space group P63mc). Although the lattice location of lanthanide dopants is microscopically not verifiable, theoretical and experimental works elsewhere [87, 88] suggested that they substitute preferentially the position of cations in III-nitrides host material (as shown in figure 3.1 (a)). In the same way as Al, the lanthanide ion (ion labelled by Ln in figure 3.1 (b)) is under a C_{3v} local symmetry, which is arranged by tree equivalent N ions on basal plane (ions N2, N3 and N4) with identical bond length and one N ion with a different bond length along c-axis (ion N1). The corresponding CF Hamiltonian $\hat{H}''_{CF}(C_{3v})$ is determined by six CF terms [67]:

$$\hat{H}''_{CF}(C_{3v}) = B_0^2 C_0^2 + B_0^4 C_0^4 + B_3^4(C_{-3}^4 - C_3^4) + B_0^6 C_0^6 + B_3^6(C_{-3}^6 - C_3^6) + B_6^6(C_{-6}^6 + C_6^6). \quad (3.10)$$
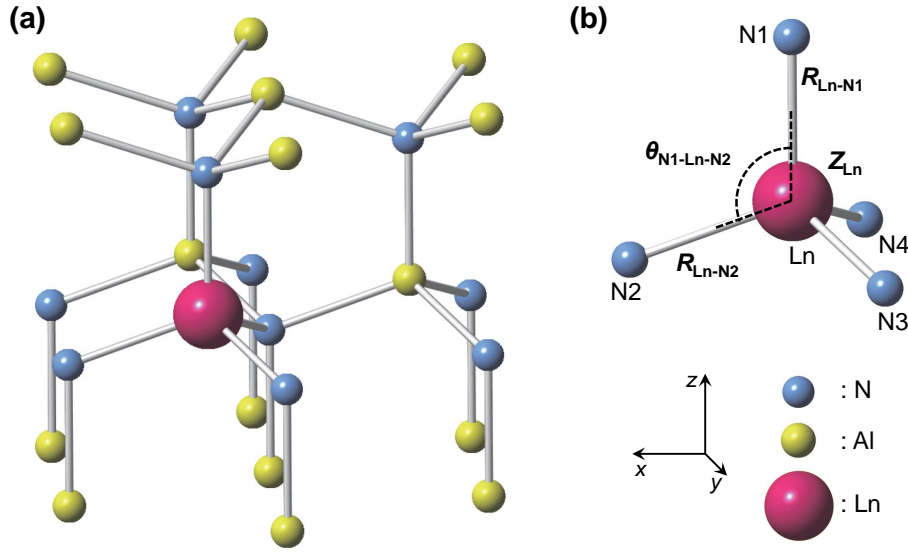
Figure 3.1: (a) Atomic structure of lanthanide doped w-AlN. One aluminium ion (yellow) is here substituted by a lanthanide ion (pink). (b) C_{3v} local symmetry of a lanthanide ion (labelled as Ln). Selection of the Cartesian system as well as the independent physical and structural parameters as discussed in the text are marked on the figure.

In order to calculate CF parameters we applied Prather's conventions [89] to settle the Cartesian coordinate system for these surrounding nitrogen ions: As can be seen in figure 3.1 (b), the 3-fold rotation axis, which correlates the c-direction of w-AlN, is chosen as z-axis. The x-axis coincide one nitrogen ion on the basal plane (here is ion N2). And y-axis is perpendicular to x- and z-axes with the direction follows right-hand rule. Through converting the Cartesian coordinates into polar coordinates, only four independent physical and structure variables (marked in figure 3.1 (b)) are needed to be considered in the calculation of effective CF Hamiltonian $\hat{H}''^{*}_{\mathrm{CF}}$ (equation 3.8 and 3.9). They are the effective point charge of surrounding nitrogen ions felt by $4f$-electrons of centre lying lanthanide ion Z_{Ln}, their radial displacements relate to $4f$-shell of lanthanide ion $R_{\mathrm{Ln\text{-}N1}}$ and $R_{\mathrm{Ln\text{-}N2}}$ ($R_{\mathrm{Ln\text{-}N2}} = R_{\mathrm{Ln\text{-}N3}} = R_{\mathrm{Ln\text{-}N4}}$) and the angle $\theta_{\mathrm{N1\text{-}Ln\text{-}N2}}$ ($\theta_{\mathrm{N1\text{-}Ln\text{-}N2}} = \theta_{\mathrm{N1\text{-}Ln\text{-}N3}} = \theta_{\mathrm{N1\text{-}Ln\text{-}N4}}$).

Due to the polycrystalline nature of the AlN layers the lanthanide local symmetry can be reduced to C_1, if, e.g., one or two nitrogen ions on the basal plane are missed at the grain boundary or replaced by point defects, such as unintentional O impurities (O_N) or N vacancies (V_N, with less probability due to large formation energy [87]). As a result, 27 CF terms are required to describe $\hat{H}''_{\mathrm{CF}}(C_1)$:

$$
\begin{aligned}
\hat{H}''_{\mathrm{CF}}(C_1) = {} & B_0^2 C_0^2 + B_1^2(C_{-1}^2 - C_1^2) + B_1'^2 i(C_{-1}^2 - C_1^2) + B_2^2(C_{-2}^2 - C_2^2) + B_2'^2 i(C_{-2}^2 - C_2^2) \\
& + B_0^4 C_0^4 + B_1^4(C_{-1}^4 - C_1^4) + B_1'^4 i(C_{-1}^4 - C_1^4) + B_2^4(C_{-2}^4 - C_2^4) + B_2'^4 i(C_{-2}^4 - C_2^4) \\
& + B_3^4(C_{-3}^4 - C_3^4) + B_3'^4 i(C_{-3}^4 - C_3^4) + B_4^4(C_{-4}^4 - C_4^4) + B_4'^4 i(C_{-4}^4 - C_4^4) \\
& + B_0^6 C_0^6 + B_1^6(C_{-1}^6 - C_1^6) + B_1'^6 i(C_{-1}^6 - C_1^6) + B_2^6(C_{-2}^6 - C_2^6) + B_2'^6 i(C_{-2}^6 - C_2^6) \\
& + B_3^6(C_{-3}^6 - C_3^6) + B_3'^6 i(C_{-3}^6 - C_3^6) + B_4^6(C_{-4}^6 - C_4^6) + B_4'^6 i(C_{-4}^6 - C_4^6) \\
& + B_5^6(C_{-5}^6 - C_5^6) + B_5'^6 i(C_{-5}^6 - C_5^6) + B_6^6(C_{-6}^6 - C_6^6) + B_6'^6 i(C_{-6}^6 - C_6^6).
\end{aligned}
$$

$$(3.11)$$

Interstitial sites

In spite of energetic instability [90, 91] a very small part of lanthanide ions might be located at interstitial sites [88]. Taking their huge ionic radii into account, tetrahedral (T) and octahedral (O) positions of AlN, both with C_{3v} symmetry, may be the proper interstitial sites for them. As shown in figure 3.2 (a), a lanthanide ion on the T site locate at the middle point between two nearest Al and N ions, Al1 and N1, along z axis. And Al2, Al3, Al4, N2, N3 and N4 are the second nearest neighbour ions. Interstitial lanthanide ion on the O site, on the other hand, is located in a pentahedral constructed by Al and N ions. Three Al ions (Al1, Al2 and Al3) and three N ions (N1, N2 and N3) are its closest neighbours (see figure 3.2 (b)).
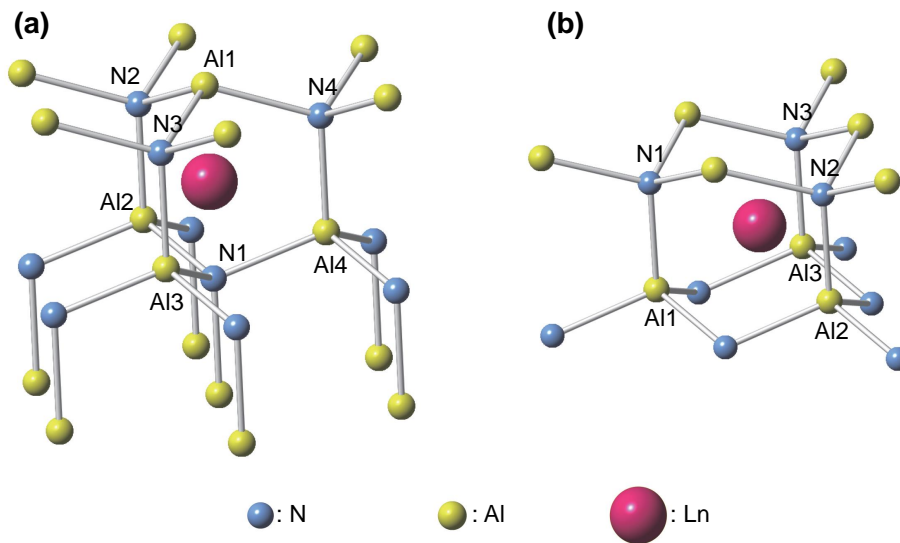
Figure 3.2: Atomic structure of lanthanide doped w-AlN, in which the lanthanide ions are placed at interstitial site T (a) and O (b). Two first and six second nearest neighbour ions, Al1, N1 and Al2, Al3, Al4, N2, N3, N4, related to lanthanide ion at T site and six first nearest neighbour ions, Al1, Al2, Al3, N1, N2 and N3, related to lanthanide ion at O site are marked.

3.2.1.1 Spectra assignment and selection rules

The splitting of lanthanide $4f$-levels due to CF perturbation (Stark levels) is in general assigned according to the local symmetry, the parity of the $4f$-electron number and total angular momentum J. Within a C_{3v} local symmetry, the Stark levels of even-electron lanthanide ions are singly and/or doubly degenerated, and labelled by their irreducible representations with Bethe notation Γ_1, Γ_2 and (Γ_3, Γ_3) respectively [92, 93]. In case of odd-electron lanthanide ions, all the Stark levels are Kramers doublets (Γ_4, Γ_4) and (Γ_5, Γ_6). Detailed energy splitting in each J-level are enumerated in table 3.1, where the symbols Γ_3, Γ_4 and $\Gamma_{5,6}$ represent (Γ_3, Γ_3), (Γ_4, Γ_4) and (Γ_5, Γ_6) for short.

In C_{3v} symmetry the x- and y-directions are equivalent to each other whereas the z direction (c-axis) is not. This means that z-direction exhibits an irreducible representation different to that of x- and y-directions. Induced electric dipole (ED) transitions between Stark levels are therefore only allowed in certain directions. As listed in table 3.2, under

C_{3v} symmetry the ED transition $\Gamma_1 \leftrightarrow \Gamma_2$ is forbidden in even-electron system, and in odd system all transitions are allowed.

As mentioned above, the C_{3v} symmetry of lanthanide ion in AlN could be reduced into C_1 due to presence of certain crystal defects. Depending on their J-number, each $4f$-level will be in this case $2J+1$ fold degenerated. And no forbidden ED transition exists.

Table 3.1: Full-rotational group compatibility table of $4f$-levels in even- and odd-electron systems under C_{3v} symmetry [67].

C_{3v}^{even}		C_{3v}^{odd}	
J	irreducible representations	J	irreducible representations
0	Γ_1	1/2	Γ_4
1	$\Gamma_2 + \Gamma_3$	3/2	$\Gamma_4 + \Gamma_{5,6}$
2	$\Gamma_1 + 2\Gamma_3$	5/2	$2\Gamma_4 + \Gamma_{5,6}$
3	$\Gamma_1 + 2\Gamma_2 + 2\Gamma_3$	7/2	$3\Gamma_4 + \Gamma_{5,6}$
4	$2\Gamma_1 + \Gamma_2 + 3\Gamma_3$	9/2	$3\Gamma_4 + 2\Gamma_{5,6}$
5	$\Gamma_1 + 2\Gamma_2 + 4\Gamma_3$	11/2	$4\Gamma_4 + 2\Gamma_{5,6}$
6	$3\Gamma_1 + 2\Gamma_2 + 4\Gamma_3$	13/2	$5\Gamma_4 + 2\Gamma_{5,6}$
7	$2\Gamma_1 + 3\Gamma_2 + 5\Gamma_3$	15/2	$5\Gamma_4 + 3\Gamma_{5,6}$
8	$3\Gamma_1 + 2\Gamma_2 + 6\Gamma_3$	17/2	$6\Gamma_4 + 3\Gamma_{5,6}$

Table 3.2: Selection rules for induced intra-$4f$ electric dipole transitions in even- and odd-electron systems under C_{3v} symmetry [67].*

	C_{3v}^{even}				C_{3v}^{odd}	
	Γ_1	Γ_2	Γ_3		Γ_4	Γ_5
Γ_1	π	forbidden	α, σ	Γ_4	α, σ, π	α, σ
Γ_2	forbidden	π	α, σ	Γ_5	α, σ	π
Γ_3	α, σ	α, σ	α, σ, π			

* The optical spectra resulted by ED transitions depend on the polarization direction of electric field vector $\vec{E}$ and magnetic field vector $\vec{H}$ related to the crystallographic c-axis: in α spectrum the light propagates parallel to c-axis with $\vec{E} \perp c$ and $\vec{H} \perp c$; in σ spectrum the light propagates perpendicular to c-axis with $\vec{E} \perp c$ and $\vec{H} \parallel c$; in π spectrum the light propagates perpendicular to c-axis with $\vec{E} \parallel c$ and $\vec{H} \perp c$.

3.2.2 Crystal field analysis on Sm^{3+} ($4f^5$) in AlN

Experimental results and determination of local symmetry

Trivalent Sm ion is an appropriate indicator to determine the lanthanide doping location in AlN host by using crystal field analysis. It is not only due to the fact that, though optical excitation at low temperature, strong luminescence can be generated through intra $4f$-transitions from a single multiplet $^4G_{5/2}$ to the ground and low energetic multiplets (see figure C.1 (b) in appendix C), but also because the luminescence peaks are well energetically separated. Moreover, Sm^{3+} has odd electrons (five) in its $4f$ orbital and
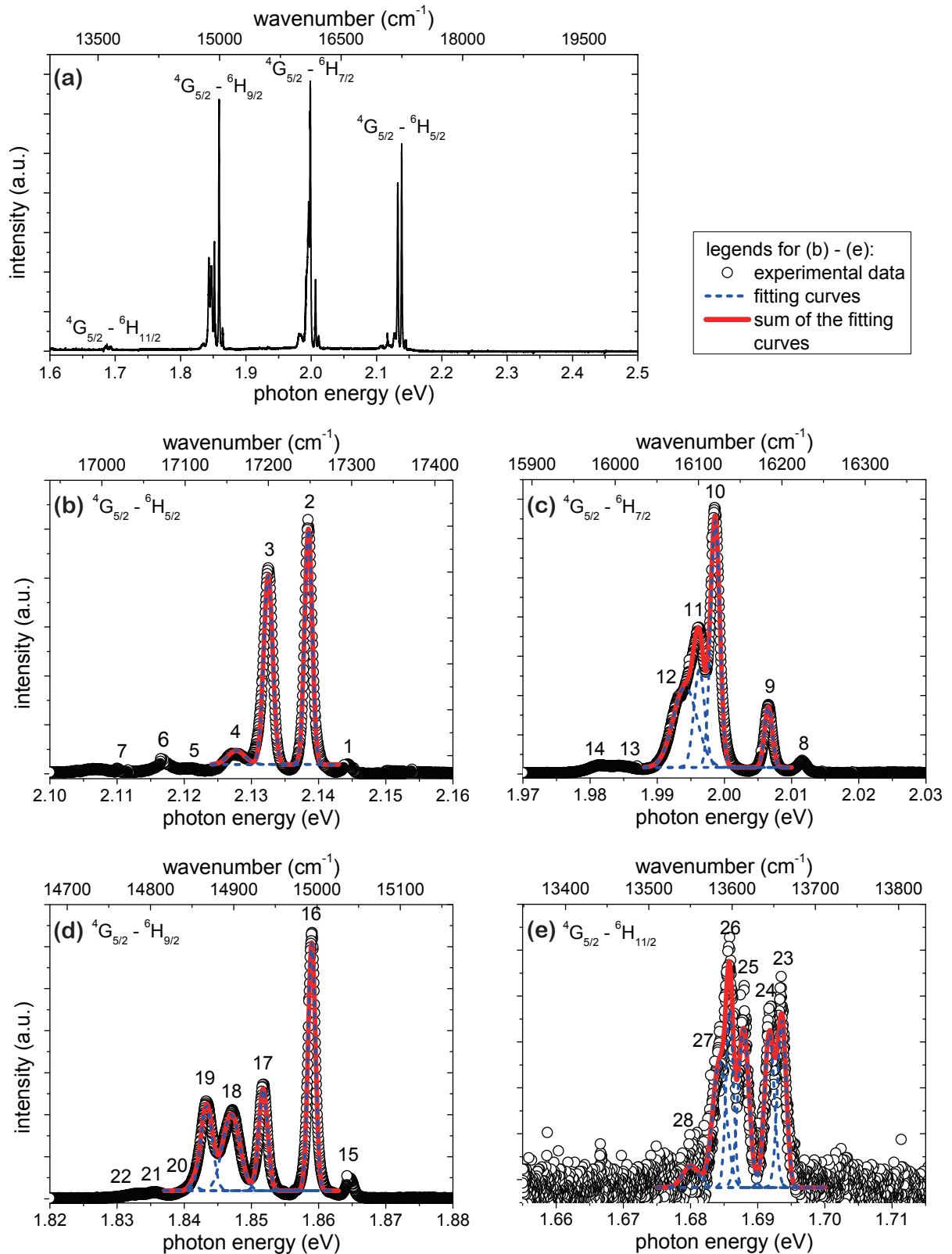
Figure 3.3: (a): High-resolution PL spectrum of AlN:Sm at 10.3 K and (b) - (e): detailed spectra indicating the transitions $^4G_{5/2}$ - ^6H_J ($J = 5/2$, $7/2$, $9/2$ and $11/2$). The layer was annealed at 1000 °C for 30 minutes. All distinguishable luminescence peaks are numbered. In order to obtain more accurate energy position, main peaks are fitted by Gaussian. Red solid lines are the fitted spectra and blue dashed lines the fitting curves to each individual peak. The energy positions are listed in table 3.3.

thus all the Stark levels are Kramers doublets. According to selection rules listed in table 3.2 there is no forbidden transition between its Stark levels in C_{3v} local symmetry.

In order to enhance the luminescence intensity (more details see chapter 4), AlN:Sm layer was annealed at 1000 °C for 30 minutes before the PL measurements at 10.3 K (by using the experimental setup described in section 3.5.2) carried out. Radiative transitions $^4G_{5/2}$ - ^5H_J ($J = 5/2$, $7/2$, $9/2$ and $11/2$) can be clearly identified in the high-resolution PL spectrum (figure 3.3 (a)). Figure 3.3 (b) - (e) show the detailed luminescence peak splitting of each transition. All distinguishable peaks are thereby numbered on the spectra, and the corresponding energy positions of peak maxima are listed in the third column of table 3.3. As can be seen from those spectra, several much weaker and relatively broader satellite lines exist next to or coincide with the intense and sharp main peaks. Energy positions of main peaks with No. 2-4, 9-12, 16-20 and 23-28 are extracted by Gaussian fitting (represented as blue dashed lines in 3.3 (b) - (e)) and listed in the fourth column of table 3.3. In lanthanide ions, the electron relaxation between different Stark levels within an individual $4f$-multiplet is much faster as compared to intra-$4f$ transitions. And under the cryogenic condition used for PL measurements the possibility of thermal population becomes very small, even though the energy positions of Stark levels are only dozens of wave numbers apart from each other. Hence it is reasonable to believe that before the intra-$4f$ transition, $4f$ electrons of lanthanide ion are all in the lowest Stark level of the excited multiplet. Setting the luminescence line at 17248 cm^{-1} (No. 2) as the transition from the lowest energy Stark level of $^4G_{5/2}$ to the ground state Stark level of $^4H_{5/2}$, other Stark levels can be determined (fifth column of table 3.3). These results are in excellent agreement with the reference published by U. Vetter et. al. (sixth column of table 3.3), in which Sm^{3+} centres were implanted into single crystalline AlN host and the Stark levels were measured from low temperature cathodoluminescence (CL) spectra [65]. Supported by the results of emission channelling and crystal field analysis they believed that the Sm^{3+} are located on substitutional Al site with C_{3v} symmetry. Relatively larger aberrations of the line number 11 and 12 (seventh column of table 3.3) are very probably due to the overlap of these two luminescence peaks as shown both in the present work (figure 3.3 (c)) and the reference [65].

On the base of this and the considerations discussed in previous section, we could deduce that the majority of radiative Sm^{3+} doped in polycrystalline AlN host also occupy the Al sites and have a C_{3v} local symmetry with the surrounding N ions. Although the existence of lanthanide ions on the interstitial site with same crystal symmetry (O and T site, cf. section 3.2.1) should not be excluded, due to their energetic instability [90, 91] they could be easily recovered by thermal annealing. The satellite lines are very probably generated by the Sm^{3+}, which are associated with crystal defects, such as vacancies and impurity ions. In this case, conditions of the C_{3v} symmetry are broken. The disturbed crystal field changes the splitting of $4f$-levels and the strength of selected ED transitions [70] and thus results additional emission lines deviated from the expectation referred to C_{3v} symmetry [94].

Table 3.3: Energy of the radiative transitions from $^4G_{5/2}$ to ^5H_J ($J = 5/2, 7/2, 9/2$ and $11/2$) of Sm^{3+} doped in AlN and the energy positions of Stark levels.

levels $^{2S+1}L_J$	No.[a]	E_m[b] cm^{-1} (eV)	E_{fit}[c] cm^{-1} (eV)	E_{Stark}[d] cm^{-1}	E_{Stark}^{ref}[e] cm^{-1}	ΔE[f] cm^{-1}
$^6H_{5/2}$	1	17295 (2.144)				
	2	17248 (2.138)	17248 (2.138)	0	0	0
	3	17200 (2.133)	17200 (2.134)	48	44	4
	4	17162 (2.128)	17162 (2.128)	86	90	-4
	5	17108 (2.121)				
	6	17071 (2.117)				
	7	17019 (2.110)				
$^6H_{7/2}$	8	16224 (2.012)				
	9	16184 (2.007)	16184 (2.007)	1064	1063	1
	10	16119 (1.999)	16120 (1.999)	1128	1128	0
	11	16100 (1.996)	16101 (1.996)	1147	1171	-24
	12	16081 (1.994)	16084 (1.994)	1164	1225	-61
	13	16004 (1.984)				
	14	15982 (1.981)				
$^6H_{9/2}$	15	15040 (1.865)				
	16	14994 (1.859)	14994 (1.859)	2254	2253	1
	17	14936 (1.852)	14935 (1.852)	2313	2308	5
	18	14899 (1.847)	14898 (1.847)	2350	2346	4
	19	14867	14867	2381	2375	6

Table 3.3 – continued from previous page

levels $^{2S+1}L_J$	No.[a]	E_m[b] cm^{-1} (eV)	E_{fit}[c] cm^{-1} (eV)	E_{Stark}[d] cm^{-1}	E_{Stark}^{ref}[e] cm^{-1}	ΔE[f] cm^{-1}
		(1.843)	(1.843)			
	20	14851	14851	2397	2402	-5
		(1.841)	(1.841)			
	21	14805				
		(1.836)				
	22	14787				
		(1.833)				
^{6}H$_{11/2}$	23	13659	13660	3588	3586	2
		(1.693)	(1.694)			
	24	13647	13645	3603	3598	5
		(1.692)	(1.692)			
	25	13615	13614	3634	3630	4
		(1.688)	(1.688)			
	26	13597	13597	3651	3649	2
		(1.686)	(1.686)			
	27	13587	13585	3663	3661	2
		(1.685)	(1.684)			
	28	13549	13551	3697	3693	4
		(1.680)	(1.680)			

[a] The label number of luminescence peak assigned in figures 3.3 (b) - (e).

[b] Energy positions of all distinguishable luminescence peaks in figures 3.3 (b) - (e). They correspond to the positions of maximal intensity.

[c] Fitted energy positions of the main luminescence peaks by using a Gaussian approximation (blue dashed lines in figures 3.3 (b) - (e)).

[d] Energy positions of Stark levels as determined in this work related to the ground state of multiplet ^{5}H$_{5/2}$.

[e] Energy positions of Stark levels of Sm^{3+}, which is implanted in single-crystalline AlN from reference [65].

[f] Energy difference between Stark levels determined in the present work and reference [65] $\Delta E = E_{Stark} - E_{Stark}^{ref}$.

CF fitting results and discussions

The computer assisted fitting program used in this work basically follows the routine map published in [83] and has been developed with MATLAB 2014b. The CF parameters (both in Stevens and Wybourne notation) and the CF Hamiltonian were firstly calculated by an initial set of input data, which include bond length and bond angle of wurtzite AlN (R_{Al-N1} = 0.192 nm, R_{Al-N2} = 0.188 nm and $\theta_{N1-Al-N2}$ = 107.68°) and valence of N ions Z_N = 3. The energy positions of Stark levels obtained through diagonalisation of CF Hamiltonian matrix were compared with our experimental results. Subsequently, the input dataset was varied continuously until the difference between calculated and experimental results was minimised. Due to a smaller number of Stark levels and a higher J-mixing effect expected at lower $4f$-levels of Sm^{3+}, we adopted the experimentally determined Stark levels of $^6H_{11/2}$ (peak number 23 - 28 in table 3.3) for this comparison. The lowest value of the calculated Stark levels was fixed at 3588 cm^{-1} (in consistence with experimental results). After this, we have further tried to parse the data with three variables, where the angle $\theta_{N1-Sm-N2}$ was kept constant and equal to the known value of wurtzite AlN $\theta_{N1-Al-N2}$. The results of the structural information and the effective charge felt by $4f$-electrons of Sm^{3+} as well as the calculated Stark levels of multiplet $^6H_{11/2}$ and CF parameters are listed in the following tables. By fitting with 4 variables, the radial displacement from $4f$-shell of Sm ion to effective point charge of N ion along the threefold axis (R_{Sm-N1}) and to the one on basal plane (R_{Sm-N2}) is about 0.230 and 0.245 nm respectively, which is significantly extended in comparison with the corresponding bond length of wurtzite AlN. And the angle $\theta_{N1-Sm-N2}$ reduces from 107.68° for wurtzite AlN to 105.10°. Large difference of ionic radius between Sm and Al could be the main reason for these structural changes. An independent *ab-initial* calculation on the structure of AlN with substitutional Tb-dopant by using the NWChem 6.1.1 program indicated that the Tb-N bond length is 0.240 (for N along threefold axis) and 0.265 nm (for N on basal plane)[3], which are in good agreement with our results. According to the screening effect one can expect that the effective charge of surrounding N ions felt by $4f$-electrons of Sm ion should be less than its valence. Z_N with a value of 2.5 listed in table 3.4 should be therefore a rational result. And based on these, energy positions of Stark level are calculated and listed in table 3.5, with acceptable deviations from experiment results.

It is quite interesting to notice from both tables that, beyond slight extension of R_{Sm-N1}, generally no considerable changes in the results can be found through fitting with fixed $\theta_{N1-Sm-N2}$. But the CF parameters, in particular with $k = 4$, are more sensitive against the variation of R_{Sm-N1} and $\theta_{N1-Sm-N2}$ (see table 3.6). This may be, on the one hand, due to the fact that the contributions of neighbouring ions on the CF perturbation decrease strongly as the distance R elongates, and obey $1/R^{k+1}$ rule. And on the other hand, the pre-factor c_{kq} in equation 3.9 decreases significantly as decreasing k-value. CF parameters with the index $k = 2$, 4 and 6 are therefore respectively sensitive against the changes of CF perturbation at larger, intermediate and smaller distance [67]. In this spirit, 3 % elongation of R_{Sm-N1} creates 20 % reduction of B_0^4 and almost no alterations for the

---

[3] unpublished work done by Dr. Gergelz Matisz. (department of the General and Physical Chemistry, University of Pécs), with permission.

parameters with $k = 2$ and 6. The parameters with q characterise every CF perturbations on the planes, which go through the q-fold axis. Hence B_3^4 enlarges 17 % by an increase of $\theta_{\text{N1-Sm-N2}}$ about 2.6 degree. And obviously this modification of structural model changes the B_3^4/B_0^4 ratio from -0.58 (4 variable fitting) to -0.85 (3 variable fitting).

Table 3.4: Fitted distance from the $4f$-shell of Sm ion to the effective point charge of N ion on the threefold axis $R_{\text{Sm-N1}}$ and on the basal plane $R_{\text{Sm-N2}}$ (nm) as well as the angle $\theta_{\text{N1-Sm-N2}}$ (°) and the effective charge felt by Sm^{3+} Z_{Sm}. Results are obtained through fitting procedure with 3 and 4 variables.

number of variables	$R_{\text{Sm-N1}}$	$R_{\text{Sm-N2}}$	$\theta_{\text{N1-Sm-N2}}$	Z_{Sm}
4	0.230	0.245	105.10	2.5
3	0.237	0.245	107.68*	2.6

* This angle was kept as constant and equals to the bond angle of wurtzite AlN during the fitting procedure.

Table 3.5: Comparison between experimentally determined and calculated energy positions of Stark levels of Sm^{3+} multiplet $^6\text{H}_{11/2}$. Results are obtained through fitting procedure with 3 and 4 variables.

No.	E_{Stark}^{exp}	4 fitting variables		3 fitting variables	
		E_{Stark}^{cal}	ΔE	E_{Stark}^{cal}	ΔE
23	3588	3588	0	3588	0
24	3603	3605	-2	3606	-3
25	3634	3620	14	3619	15
26	3651	3633	18	3635	16
27	3663	3649	14	3649	14
28	3697	3685	12	3686	11

Table 3.6: Calculated CF parameters of Sm^{3+} in Stevens and Wybourne notation (A_q^k and B_q^k in cm^{-1}). Results are obtained through fitting procedure with 3 and 4 variables.

k	q	4 fitting variables		3 fitting variables	
		A_q^k	B_q^k	A_q^k	B_q^k
2	0	47	94	47	93
4	0	172	1378	137	1096
4	3	2359	-797	2752	-930
6	0	23	370	23	375
6	3	-282	220	-290	227
6	6	-238	-251	-229	-241

3.2.3 Crystal field analysis on Tb^{3+} $(4f^8)$ in AlN

Experimental results and determination of local symmetry

In terms of Tb doped AlN, spectra splitting due to CF perturbation is much more complicated: Because of larger J value the splitting number of the luminescence peak observed in AlN:Tb is higher than that in AlN:Sm. Furthermore, trivalent Tb ion possesses an even number of $4f$-electrons. This means that the Stark levels can be singly or doubly degenerated and one forbidden ED-transition exists (cf. table 3.1). As shown in figure 3.4 (a), two groups of radiative intra-$4f$ transitions, respectively originated from two multiplets $^5D_3$ and $^5D_4$ to ^7F_J ($J = 6$, 5, and 4), are detectable. In analogy to the spectra analysis in the previous section the energy positions of each distinguishable luminescence peaks are graphically determined on figure 3.4 (b) - (g) and summarised in table 3.7.

There is only one report dealing with the CF splitting of Tb luminescence in III-nitride host material hitherto. It stated that the radiative Tb ions are located at the site with D_2 instead of C_{3v} symmetry in GaN [95]. Since the energy positions of Stark level identified thereby were quite different from our experiment results, we cannot use them as an
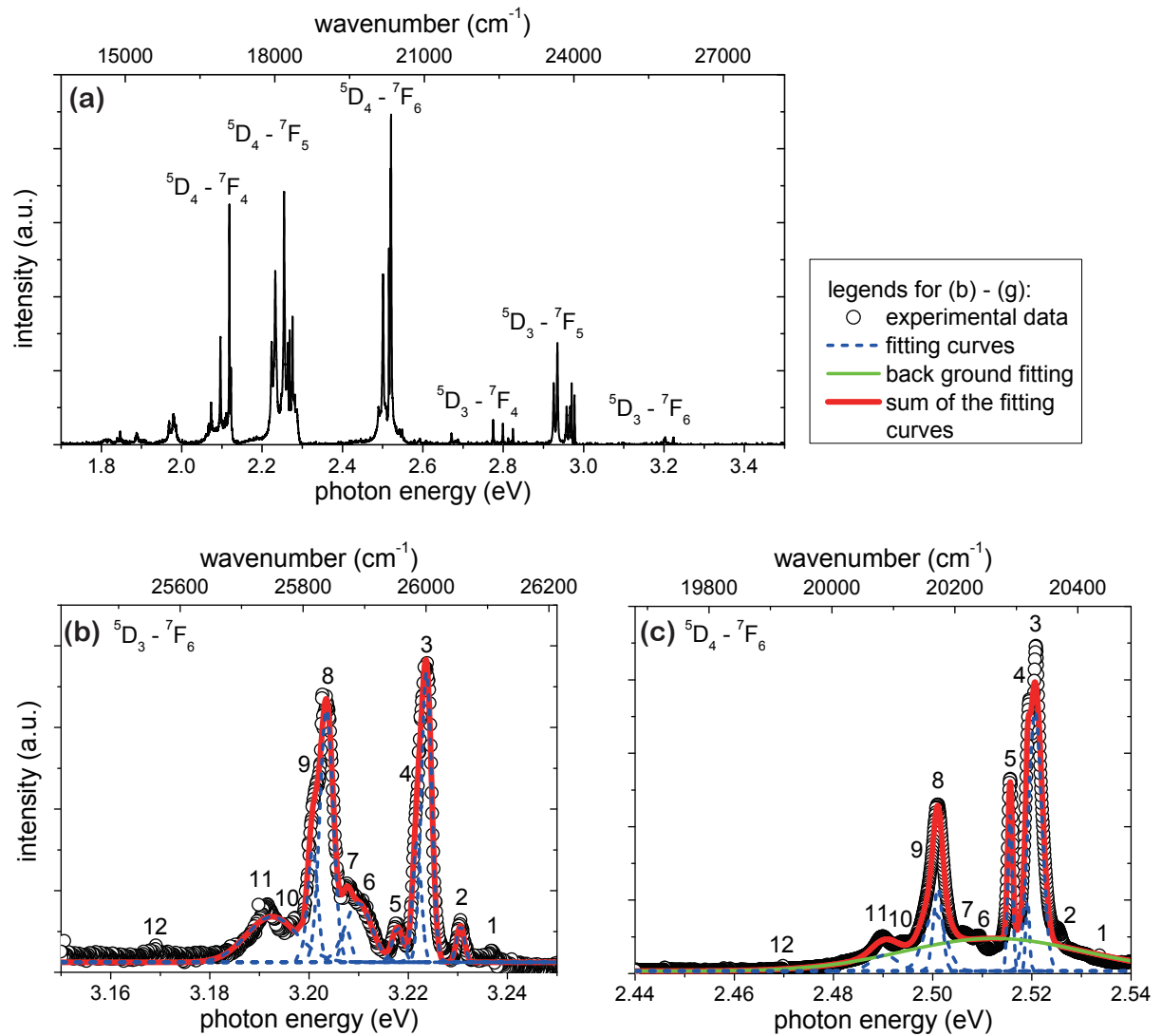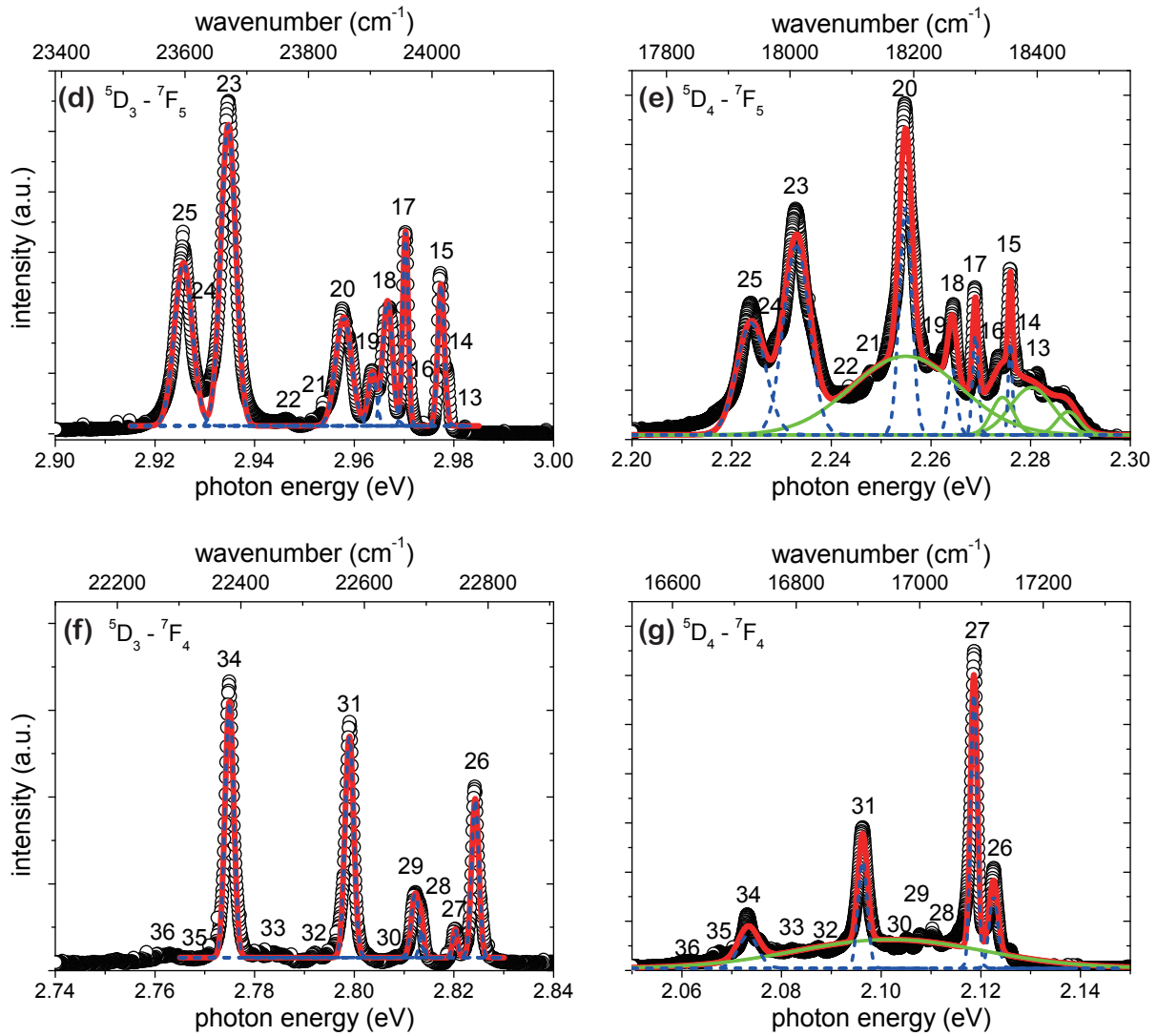
Figure 3.4: (a) High-resolution PL spectrum of AlN:Tb at 10.2 K, (b) (d) and (f): detailed spectra indicating the transitions $^5D_3$ - ^7F_J (J = 6, 5, and 4) and (c), (e) and (g): detailed spectra indicating the transitions $^5D_4$ - ^7F_J (J = 6, 5, and 4). The layer was annealed at 1000 °C for 30 minutes. All distinguishable peaks are numbered on the spectra. In order to obtain the energy position more accurately, mean luminescence peaks are fitted by Gaussian. Red solid lines are the fitted spectra, blue dashed lines the fitting curves to each individual peak and green solid lines the fitting curves to the back ground signal. The energy positions are listed in table 3.7.

adequate reference in the CF analyse. According to the selection rules of ED transition and the number of Stark levels, we may suggest that in our case the most radiative Tb ions in polycrystalline AlN are positioned in C_{3v} local symmetry:

Because the transition $\Gamma_1 \leftrightarrow \Gamma_2$ is forbidden in C_{3v} local symmetry, the total number of observable ED-transitions depends on the irreducible representation of the initial Stark level (see table 3.2). As clearly indicated from PL spectra and table 3.7, nine intense peaks (no. 2 - 9 and 11) are distinguishable in the transition $^5D_3$ - $^7F_6$, seven (no. 15, 17 - 20, 23 and 25) in $^5D_3$ - $^7F_5$ and six (no. 26 - 29, 31 and 34) in $^5D_3$ - $^7F_4$, whereas three peaks (no. 2, 6 and 7) are supressed in $^5D_4$ - $^7F_6$, one (no. 19) in $^5D_4$ - $^7F_5$ and two (no.

28 and 29) in $^5D_4$ - $^7F_4$. Numbers of those observed transitions are in consistence with the last two rows enumerated in table 3.8. On this basis we suppose that the irreducible representation of the lowest Stark level of $^5D_3$ is Γ_3 and the one of $^5D_4$ is Γ_2. The suppressed (or vanished) peaks may therefore relate to the Stark levels with Γ_1 in multiplets $^7F_6$, $^7F_5$ and $^7F_4$, and labelled in the fifth column of tables 3.7.

Table 3.7: Energy of the radiative transitions from $^5D_3$ and $^5D_4$ to ^7F_J ($J = 6$, 5, and 4) of Tb^{3+} doped in AlN and the energy positions of Stark levels.

levels $^{2S+1}L_J$	No.[a]	transition $^5D_3$ - ^7F_J			transition $^5D_4$ - ^7F_J			ΔE [h]
		E_m[b] cm^{-1} (eV)	E_{fit}[c] cm^{-1} (eV)	E_{Stark}[d] cm^{-1}	E_m[e] cm^{-1} (eV)	E_{fit}[f] cm^{-1} (eV)	E_{Stark}[g] cm^{-1}	cm^{-1}
$^7F_6$	1	26231 (3.252)						
	2	26056 (3.231)	26056 (3.231)	0 (Γ_1)			0	0
	3	26002 (3.224)	26001 (3.224)	55	20332 (2.521)	20332 (2.521)	55	0
	4	25984 (3.222)	25985 (3.222)	71	20321 (2.520)	20318 (2.519)	67	4
	5	25951 (3.218)	25954 (3.218)	102	20290 (2.516)	20290 (2.516)	95	7
	6	25897 (3.211)	25890 (3.211)	166 (Γ_1)	20237 (2.509)			
	7	25871 (3.208)	25870 (3.207)	186 (Γ_1)	20211 (2.506)			
	8	25837 (3.203)	25838 (3.204)	218	20171 (2.501)	20172 (2.501)	213	5
	9	25822 (3.202)	25816 (3.201)	240		20167 (2.500)	218	22
	10	25787 (3.197)			20115 (2.494)			
	11	25742 (3.192)	25749 (3.193)	306	20083 (2.490)	20085 (2.490)	300	7
	12	25561 (3.169)			19920 (2.470)			
$^7F_5$	13	24053 (2.982)			18400 (2.281)			
	14	24022 (2.978)						
	15	24013 (2.977)	24015 (2.977)	2041	18356 (2.276)	18357 (2.276)	2029	13
	16				18338 (2.274)			

Table 3.7 – continued from previous page

| levels $^{2S+1}L_J$ | No.[a] | transition $^5D_3$ - ^7F_J | | | transition $^5D_4$ - ^7F_J | | | ΔE [h] cm^{-1} |
		E_m [b] cm^{-1} (eV)	E_{fit} [c] cm^{-1} (eV)	E_{Stark} [d] cm^{-1}	E_m [e] cm^{-1} (eV)	E_{fit} [f] cm^{-1} (eV)	E_{Stark} [g] cm^{-1}	
	17	23957 (2.970)	23957 (2.970)	2099	18299 (2.269)	18300 (2.269)	2085	14
	18	23931 (2.967)	23928 (2.967)	2128	18264 (2.264)	18263 (2.264)	2122	5
	19	23903 (2.964)	23903 (2.964)	2153 (Γ_1)	18251 (2.263)			
	20	23855 (2.958)	23857 (2.958)	2199	18186 (2.255)	18187 (2.255)	2198	1
	21	23829 (2.954)			18132 (2.248)			
	22	23764 (2.946)						
	23	23670 (2.935)	23670 (2.935)	2386	18009 (2.233)	18010 (2.233)	2375	11
	24				17978 (2.229)			
	25	23597 (2.926)	23597 (2.926)	2459	17937 (2.224)	17937 (2.224)	2448	10
$^7F_4$	26	22779 (2.824)	22779 (2.824)	3277	17120 (2.123)	17120 (2.123)	3266	11
	27	22747 (2.820)	22747 (2.820)	3309	17088 (2.119)	17088 (2.119)	3298	12
	28	22688 (2.813)	22692 (2.814)	3363 (Γ_1)	17022 (2.111)			
	29	22682 (2.812)	22682 (2.812)	3374 (Γ_1)	17000 (2.108)			
	30	22651 (2.808)			16979 (2.105)			
	31	22576 (2.799)	22576 (2.799)	3480	16908 (2.096)	16908 (2.096)	3478	3
	32	22520 (2.792)			16836 (2.087)			
	33	22452 (2.784)			16794 (2.082)			
	34	22381 (2.775)	22381 (2.775)	3675	16721 (2.073)	16722 (2.073)	3663	12
	35				16678 (2.068)			

Table 3.7 – continued from previous page

levels $^{2S+1}L_J$	No.[a]	transition $^5D_3$ - ^7F_J			transition $^5D_4$ - ^7F_J			ΔE [h] cm^{-1}
		E_m [b] cm^{-1} (eV)	E_{fit} [c] cm^{-1} (eV)	E_{Stark} [d] cm^{-1}	E_m [e] cm^{-1} (eV)	E_{fit} [f] cm^{-1} (eV)	E_{Stark} [g] cm^{-1}	
	36	22285 (2.763)			16623 (2.061)			

[a] The label number of luminescence peak assigned in figures 3.4 (b) - (g).

[b] and [e] Energy positions of all distinguishable luminescence peaks in figures 3.4 (b) - (g). They correspond to the positions of maximal intensity.

[c] and [f] Fitted energy positions of the main luminescence peaks by using a Gaussian approximation (blue dashed lines in figures 3.4 (b) - (g)).

[d] and [g] Energy positions of the Stark levels of ^7F_J (J = 6, 5, and 4) as determined in this work related to the ground state of multiplet $^7F_6$. Values in [d] and [g] were determined through the transition originated from multiplet $^5D_3$ and $^5D_4$ respectively. The levels with irreducible representation Γ_1 are labelled in the parentheses.

[h] Energy difference between Stark levels determined by radiative transitions from multiplet $^5D_3$ and $^5D_4$.

Table 3.8: Number of possible ED-transitions from initial states Γ_1, Γ_2 and Γ_3 to multiplets with J = 6, 5, 4.

irreducible representation of initial level	multiplet of final level		
	$J = 6$	$J = 5$	$J = 4$
Γ_1	7	5	5
Γ_2	6	6	4
Γ_3	9	7	6

Fitting results and discussion

Unfortunately, efforts of computer fitting didn't provide any convincing local structural and physical information on radiative Tb ions in AlN. Some of the calculated Stark levels have quite large deviations (50 - 100 cm^{-1}) from the experimental results. Strong J-mixing effects on those low energetic multiplets may be the reason for this.

3.3   Conclusions

In order to exploit the radiative intra-$4f$ transitions of lanthanide ions in light emission applications, the ions must be located in a non-centrosymmetric environment. This is a basic prerequisite for the design of lanthanide phosphor materials. In this chapter, splitting of characteristic luminescence peaks from AlN:Sm and AlN:Tb layers under cryogenic conditions were analysed according to crystal field theory. We conclude that most of the radiative ions are placed in a C_{3v} local symmetry. Results of computer assisted fitting procedure indicate that the displacement of $4f$-shell of substitutional Sm ion to the effective point charge of N ions along three fold axis and on the basal plane ($R_{\text{Sm-N1}}$ and $R_{\text{Sm-N2}}$) is about 0.230 and 0.245 nm respectively, and the angle $\theta_{\text{N1-Sm-N2}}$ 105.10°. The effective charge of 4 surrounding N ions felt by Sm ion Z_{Sm} is 2.5. Unsatisfying fitting results of AlN:Tb system calls for further considerations of other effects on the spectral splitting (e.g. J-mixing effect), which should be solved in future works.

Chapter 4

Lanthanide luminescence enhancement via trivial procedures - thermal treatment and collateral effects

According to the discussions in last chapter, one should keep in mind that the radiative intra-$4f$ transitions of trivalent lanthanide ion are allowed, only if the wave functions of those electrons are electrostatically disturbed by the non-centrosymmetric surrounding ions. We may define the radiative lanthanide ions with this kind of ionic architecture as "*lanthanide luminescence centres*" (LLC). The lanthanide luminescence intensity is intrinsically proportional to the strength of the corresponding ED transition, which is determined by the CF parameters with odd k values. Although the "intrinsic" intensity can be predicted by *ab-initio* calculations [70], these theoretical values are hardly consistent with experimental results, especially in the case of lanthanide-doped semiconductor systems. This is essentially related to the type of excitation (direct, above or below band gap excitation) and all electron processes competing with the lanthanide excitation and consecutive radiative relaxation. All of them can "extrinsically" affect the observed luminescence intensity. Therefore, once the host material is selected according to crystal field theory, the task for the material scientists is to find out proper procedures to suppress the competing processes. Restriction of doping concentration in an appropriate range, choosing of wide band gap semiconductor as host material and reduction of operating temperature etc. are well-understood methods to prevent concentration quenching [63] and thermal quenching [96].

On the other hand, it is widely accepted that thermal annealing is a trivial post-treatment method to activate the lanthanide luminescence centres and increase their luminescence intensity through atomic rearrangement of lanthanide dopants [97] and the host [98]. It may further regulate energy states within the band gap, which are in particular formed by the native crystal defects of the semiconductor host. Because the physical processes lying behind are extremely complicated, a quantitative description on the thermal enhancement of the lanthanide luminescence intensity is still lacking.

In this chapter we try to solve this problem in the case of the AlN:Ln system. Based on photoluminescence results we confirm in section 4.1 that the luminescence intensity

of Pr^{3+}, Sm^{3+}, Tb^{3+} and Tm^{3+} in AlN can be significantly enhanced through appropriate thermal treatment. Additionally we find a correlation of intensity between the luminescence originated from lanthanide centres and that from defect states, which are collaterally formed by the unintended oxygen impurities during thermal treatment. This may reveal a substantial path to excite lanthanide luminescence centres in AlN with an optical pumping below the band gap (section 4.2). Combined with excitation and relaxation mechanisms, effects of thermal treatment on lanthanide luminescence are discussed and modelled by introducing a concept of "*extended lanthanide luminescence centres*" (ELLC) at the end of this chapter (section 4.3).

4.1 General Photoluminescence results of AlN:Ln (Ln = Pr, Sm, Tb, Tm)

Using the sputtering parameters listed in the table A.1 of appendix A, doping concentration of AlN:Ln layers (Ln = Pr, Sm, Tb, Tm) is kept approximately 1 at.-% (results of ICP-OES, see table B.1 in appendix B). According to our previous results [63, 99], the influence of concentration quenching on the lanthanide luminescence can be neglected. The as-prepared layers were put into a quartz tube furnace with nitrogen protective gas and annealed for 30 minutes at different temperatures[1] respectively (for details see section 2.2).

Room temperature PL measurements on the AlN:Ln layers before and after annealing were performed by using the equipment setup introduced in section 2.5.2. The resulting spectra of selected layers (as-prepared as well as annealed at 400 °C, 600 °C, 800 °C and 1000 °C) are shown in figure 4.1 as examples. It can be seen from figure 4.1 (a) that, despite of broad defect luminescence peaks the transition $^3P_1$ - $^3H_5$, which corresponds to a pure green line centered at the photon energy 2.36 eV (525 nm), is the main radiative transition of Pr^{3+} doped in AlN. In addition, luminescence peaks with much lower intensity originated from the transitions $^3P_0$ - $^3H_5$ at 2.27 eV (545 nm), $^3P_2$ - $^3F_2$ at 2.14 eV (579 nm) and $^3P_0$ - $^3F_2$ at 1.93 eV (643 nm) are detectable. In agreement with the low temperature PL spectra analysed in section 3.2.2 and 3.2.3, pink-red luminescence of Sm^{3+} arise from the transitions $^4G_{5/2}$ - ^6H_J, with $J = 5/2$, $7/2$, $9/2$ and $11/2$, and multi-coloured luminescence of Tb^{3+} from $^5D_4$ - ^7F_J, with $J = 3$, 4, 5 and 6, are dominant at room temperature as well (figure 4.1 (b) and (c)). At room temperature, effects of thermal population of excited $4f$-electrons into higher Stark levels and lattice vibration are much stronger [67]. Additionally due to the limited detector resolution the detected luminescence peaks are comparatively broader and the fine structure of CF splitting is hardly to be identified. In figure 4.1 (d) two blue sharp peaks in visible region ($^1D_2$ - $^3F_4$ and $^1G_4$ - $^3H_6$) and one in ultra violet region ($^1D_2$ - $^3H_6$) emitted by Tm^{3+} are easily to be found[2].

In order to analysis the effect of thermal annealing on the activation of lanthanide lu-

---

[1] 150 °C, 300 - 800 °C with interval of 100 °C and 850 - 1000 °C with interval of 50 °C.
[2] Details about the energy positions of these lanthanide $4f$-levels related to the band gap energy of AlN host are illustrated in figure C.1 (appendix C).
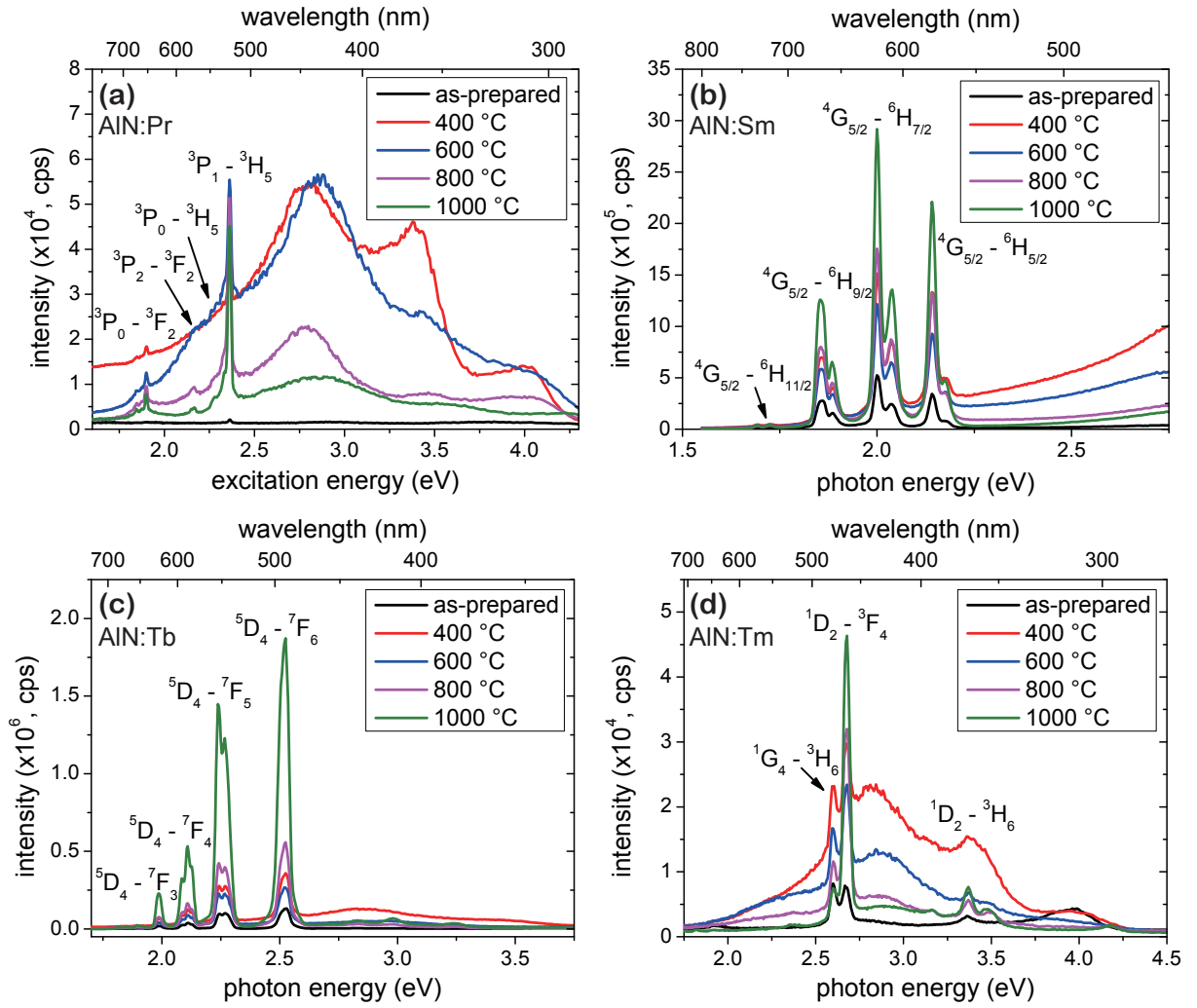
Figure 4.1: Room temperature PL spectra of (a) AlN:Pr, (b) AlN:Sm, (c) AlN:Tb and (d) AlN:Tm layers before and after annealing at selected temperatures. The main peaks are labeled with the corresponding intra $4f$-transitions. According to the PLE spectra (cf. figure 4.9), excitation energy (E_{exc}) are chosen as 4.6 eV for AlN:Pr, 4.5 eV for AlN:Sm, and AlN:Tb and 4.8 eV for AlN:Tm.

minescence centres, the temporal development of luminescence intensities during thermal annealing (kinetics) must be clarified. For this propose, the as-prepared layers were separately encapsulated in quartz tube with nitrogen protective gas as shown in figure 2.3 (b) and annealed at different temperatures. After selected annealing durations (5, 10, 20, 30, 45 and 60 minutes), capsules were quenched in ice-water. Such procedure allows a more precise adjustment of the annealing duration. In figure 4.2 the integrated lanthanide luminescence intensities from AlN:Sm, AlN:Tb and AlN:Tm layers are plotted against annealing duration. We can conclude therefrom that basically after 10 minutes, most of lanthanide luminescence centres are well activated and "stabilised". A further annealing will not affect a considerable intensity variation. This is in general agreement with our previous approaches made by F. Benz [100].

In view of this observation, it is reasonable to analyse the relationship between annealing temperature and thermal activation of lanthanide luminescence centres, only if the layers

were annealed at selected temperatures for at least 10 minutes. Thus we can use the integrated PL intensities of the layers, which were annealed in the quartz tube furnace for 30 minutes (corresponding to the results in figure 4.1), to establish its temperature dependence. As illustrated in figure 4.3, the integrated luminescence intensity increases significantly, if the temperature is higher than 700 °C. Using the equation 4.9, discussed later in section 4.3, we attempt to mathematically fit the developments of lanthanide luminescence intensity during isothermal and isochronal annealing, as represented by dashed lines in figure 4.2 and 4.3.

Furthermore, it is necessary to notice that within an intermediate temperature interval, say 300 to 600 °C, the integrated intensity exhibits a secondary maximum. Reasons for this phenomenon will be discussed in following section.
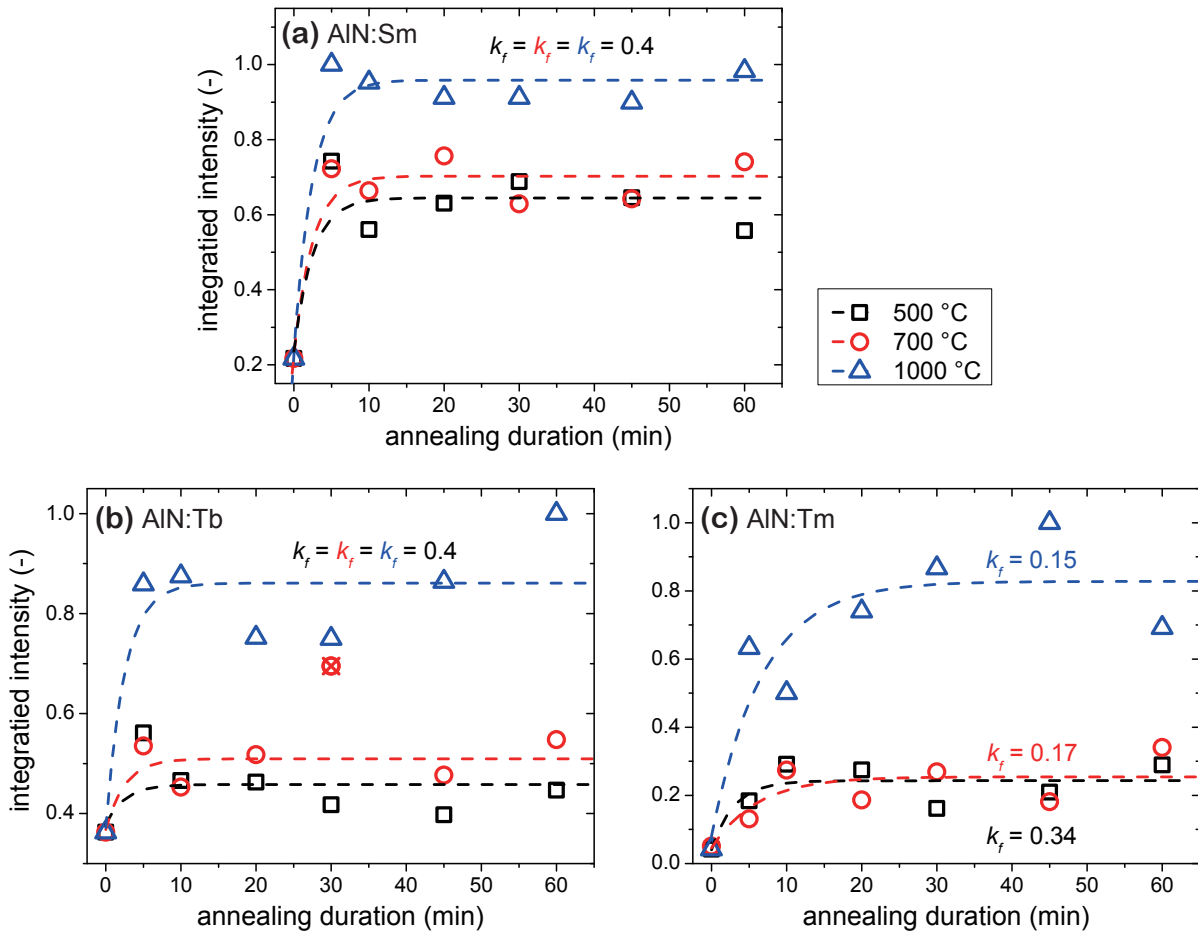
Figure 4.2: Development of luminescence intensity from (a) AlN:Sm, (b) AlN:Tb and (c) AlN:Tm layers during thermal annealing at 500 °C, 700 °C and 1000 °C. Area of visible luminescence peaks, corresponds to the transitions $^4G_{5/2}$ - $^6H_{5/2,7/2,9/2}$ in AlN:Sm (E_{exc} = 4.6 eV), $^5D_4$ - $^7F_{3,4,5,6}$ in AlN:Tb (E_{exc} = 4.6 eV), $^1D_2$ - $^3F_4$ and $^1G_4$ - $^3H_6$ in AlN:Tm (E_{exc}= 4.8 eV), is integrated and plotted against annealing duration. The dashed lines are fitting curves by using equation 4.9. Data with cross (on figure (b)) is considered as a test error and excluded for the fitting.
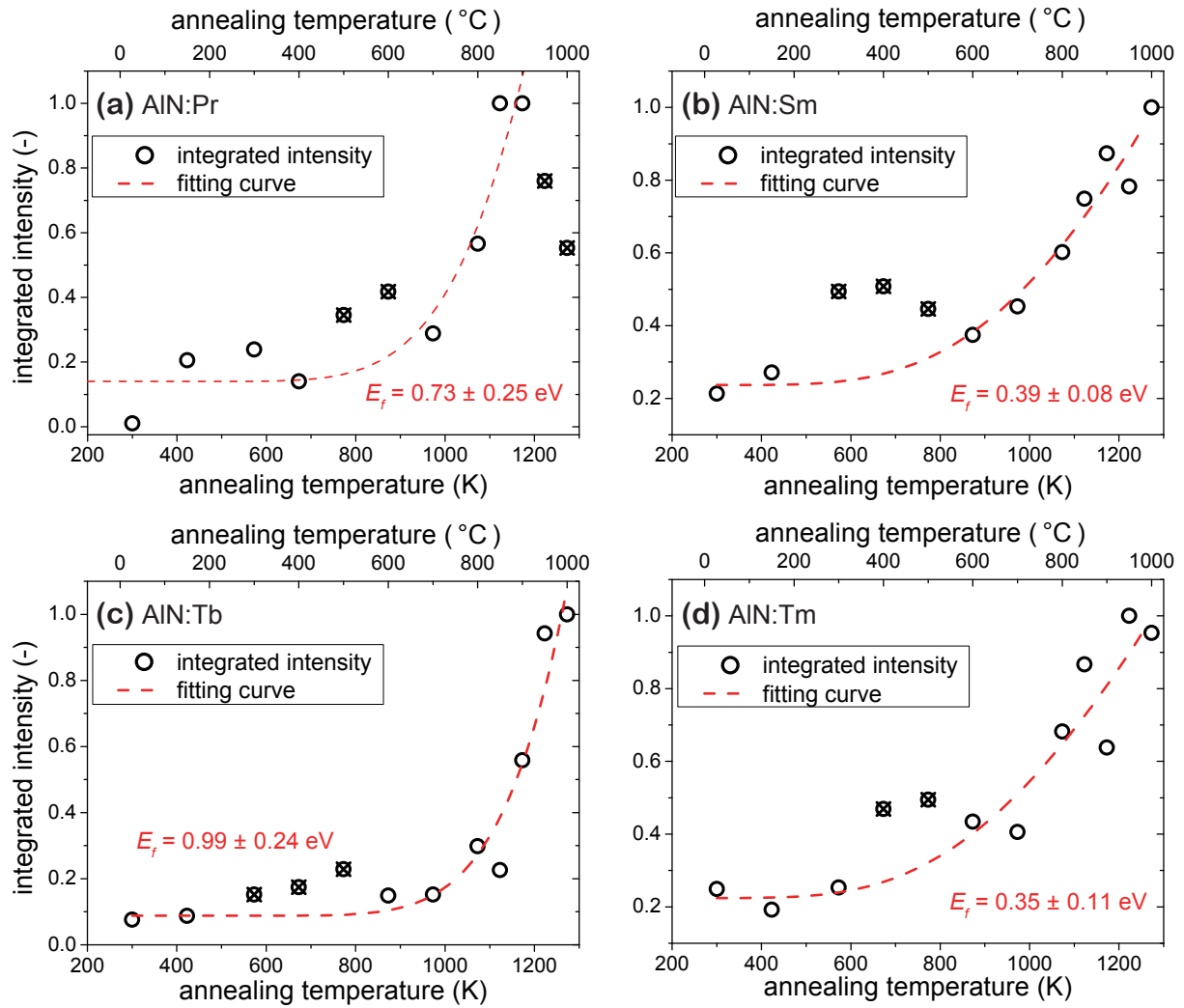
Figure 4.3: Plots of integrated visible luminescence intensity of (a) AlN:Pr, (b) AlN:Sm, (c) AlN:Tb and (d) AlN:Tm layers against annealing temperature (from room temperature to 1000 °C). The thermal enhancements of lanthanide luminescence are fitted by using equation 4.9 (red dashed curves). Crossed data are excluded from the evaluation.

4.2   Excitation of lanthanide luminescence centres assisted by O-associated defect states

Combining our microscopic and chemical analytical results with the models postulated in the references, oxidation on the surface and grain boundaries of AlN host before and after thermal annealing is represented in section 4.2.1. We suppose on the basis of our PL and PLE investigations that the pronounced defect luminescence in AlN host after annealing at intermediate temperatures originate from O-associated defect states within the band gap. These states are keys to efficiently generate specific lanthanide luminescence under below band gap excitation (see section 4.2.2).

4.2.1   Surface and grain boundary oxidation of AlN

Because of the higher affinity of Al for O than that for N, the small ionic radius mismatch between O and N, and the high thermal stability of Al-O bond up to at least 1500 °C, AlN can easily reacts with moisture and O_2 in the air to form oxidation shells even at room temperature [101]. Hence it is extremely difficult by conventional production processes to obtain O-free AlN.

Oxidation of AlN is followed by O substitutions on N sites. At low O concentrations ($<$ 0.75 at.-%), every three O ions incorporated on N sites will generate one Al vacancy to conserve the charge neutrality. With increasing O concentration, an Al_2O_3 phase, where Al ions are octahedrally bound with surrounding O ions, becomes more and more stable in the AlN phase [102]. According to the phase diagram of the pseudo-binary AlN-Al_2O_3 system established by J. W. McCauley and N. D. Corbin [103], both phases co-exist in the whole composition range at temperatures below 1700 °C. Furthermore, it has been demonstrated that they form a long period polytypoid structure in their homogeneous mixture and the Al_2O_3 phase is identified as planar oxygen-containing stacking faults in AlN phase [102]. In an AlN-Al_2O_3 system with 95 mol.-% AlN, for instance, an oxygen-free 2H-AlN (Ramsdell notation) is modified into a 32H polytype with c-periodicities of 8.3 nm, in which sequences of 31 repeated AlN layer are separated by 1 Al_2O_3 layer [104]. According to our previous investigations by XPS and AES, AlN layers, which were stored in air, contain already approximately 10 at.-% O before thermal annealing [84, 105, 106, 107]. This high concentration of O contamination is essentially attributed to the layer structure. As shown in figure 4.4 (a), the as-prepared AlN:Pr layer deposited by sputtering exhibits a polycrystalline structure constructed of columnar grains with a diameter of about 20 - 30 nm. If the layers are annealed in the quartz tube furnace, no changes in grain size are observed (see figure 4.4 (b) - (d)[3]), whereas the content of O increases. It rises from about 13 at.-% after 30 minutes annealing at 100 °C to 15 at.-% at 500 °C and reaches approximately 24 at.-% at 1100 °C [107]. Limited gas tightness of furnace and decomposition of seal oil at higher temperatures may be the main source of these O impurities. As confirmed by EELS based elemental mapping, the O impurities are inhomogeneously distributed in AlN, regardless of whether the layers were annealed or not, or even annealed under pure O atmosphere (figure 4.4 (e) - (i)). They are localised on the layer surface and grain boundary and establish an oxidation shell, which intuitively prevents further oxidation into the AlN rich core. This observation is in accordance with the report of G.A. Slack [101]. Hence we may assume that the oxidation shells in our layers are built by an assembly of AlN-Al_2O_3 sequences with different periodicities, even though the accurate evidence on atomic structure of our oxidation shell is lacking.

Obviously, the AlN layer annealed under oxygen atmosphere is more severely oxidised on the surface and grain boundaries than the one under nitrogen (cp. Figure 4.4 (k) and (l)). Because the symmetry of lanthanide ions, which are located in the Al_2O_3 phase, is different to that in the AlN phase, one may expect a distinct set of spectral splitting. However, not only in the room temperature PL spectra of AlN:Pr as shown in figure 4.5

---

[3] Contrast of the TEM BF-image in figure 4.4 (d) is dark above the layer surface, because after the annealing it was additionally coated with gold.
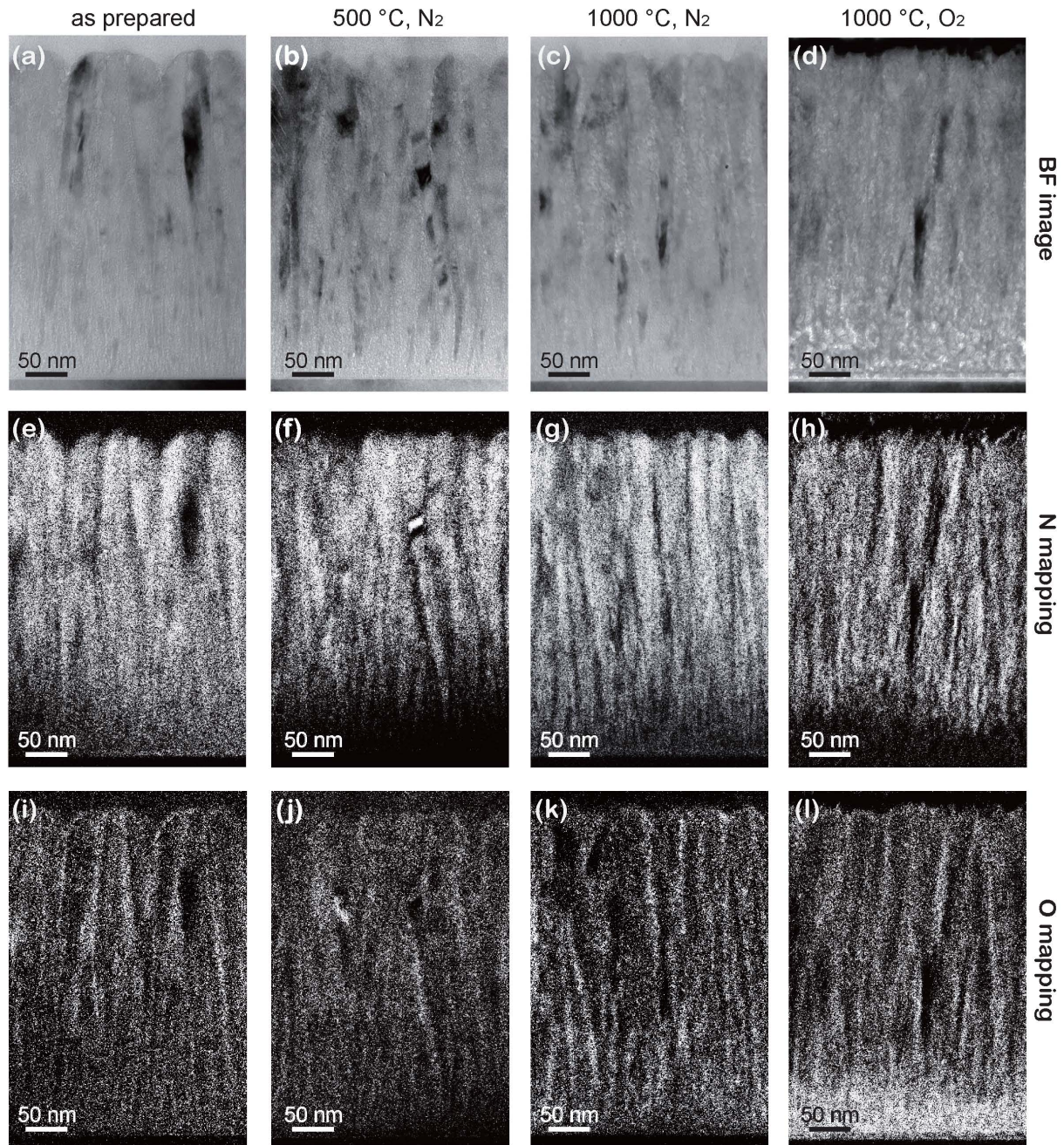
Figure 4.4: TEM bright field (BF) imaging of AlN:Pr layers before (a) and after 30 minutes thermal annealing at 500 °C under nitrogen (b), 1000 °C under nitrogen (c), 1000 °C under oxygen (d). The figures (e) - (h) and (i) - (l) are the corresponding elemental mapping of N and O by using EELS at same position.

but also in the low temperature PL spectra of AlN:Sm, AlN:Tb and AlN:Tm [108], merely no difference in the luminescence intensity and spectral shape can be found. Hence we conclude that the oxidation shell has minor influence on the lanthanide luminescence. And the majority of radiative lanthanide centres are located in the AlN phase.

It's worth mentioning that although O impurities are believed to form stable periodic structures at the layer surface and the grain boundaries, a little amount of them are able to diffuse into the AlN-rich core and segregate to other crystal defects. As will be
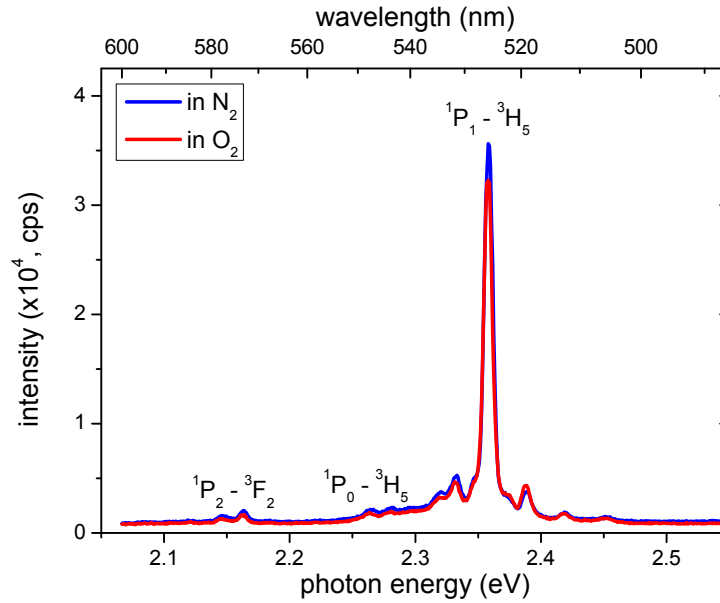
Figure 4.5: Room temperature PL spectra of AlN:Pr after 30 minutes annealing at 1000 °C under nitrogen (blue) and oxygen (red) atmosphere. In order to obtain more accurate spectral resolution to identify the luminescence splitting the scanning parameters are different from the other room temperature spectra presented in this work (excitation slit: 4 nm, emission slit: 1 nm, scan step: 0.2 nm pro second).

discussed in the next section, the energy states generated by such extended defects would emit defect luminescence under optical pumping and support the excitation of lanthanide luminescence centres.

4.2.2 Correlation between luminescence arising from O-associated defects and lanthanide centres

Luminescence from oxygen-related defects in AlN

Despite of the lanthanide luminescence, the AlN host can also emit defect luminescence with conspicuous broader peaks, especially after annealing at intermediate temperatures (300 - 600 °C). Figure 4.6 (a) compares the PL spectra of AlN and AlN:Sm layers in their high-energetic region, which were respectively annealed at 500 °C and 1000 °C for 30 °C minutes. Energy position of this luminescence centred at 2.8 eV (ca. 440 nm, marked with arrows) is basically independent of whether the AlN layers are doped with lanthanide ions or not. PLE spectra monitored at this peak indicate that it can be very efficiently generated by excitation energy of around 4.5 eV (see figure 4.6 (b)).

Similar results were also reported in the literatures, in which the lanthanide ions were implanted into single crystalline AlN grown by molecular beam epitaxy (MBE) [97, 109]. The authors suggested that the interconfigurational $4f^{n-1}5d \rightarrow 4f^n$ transitions and recombination of bound excitons in isovalent carrier traps induced by lanthanide dopants might be responsible. According to the numerous investigations on the AlN defect luminescence since the end of 1960s, which will be briefly reviewed as follows, we by contrast deduce
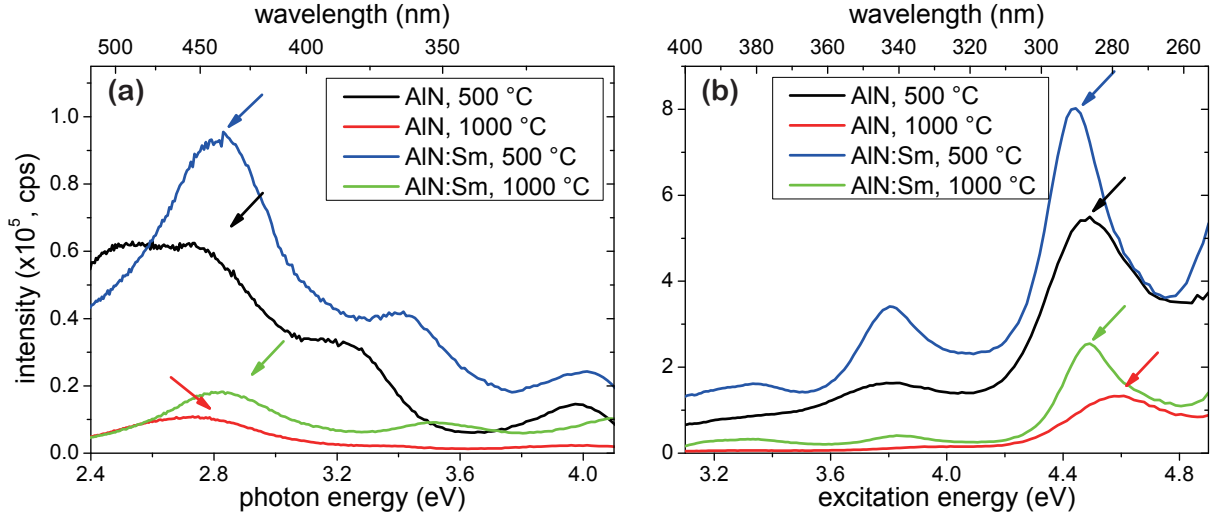
Figure 4.6: Room temperature (a) PL (excited by 4.5 eV) and (b) PLE spectra (monitored at 2.8 eV) of the broad luminescence generated in AlN layers with and without Sm doping. Layers were annealed at 500 °C and 1000 °C for 30 minutes respectively. The peaks centred at about 2.8 eV in PL spectra and centred at about 4.5 eV in PLE spectra are marked with arrows. Spectra of AlN doped with other lanthanides are similar to the spectra of AlN:Sm presented here.

that those peaks are originated from the O-associated defect states within the band gap of AlN.

In w-AlN the isolated O impurities reside substitutionally on a N site. The neutral state of O_N is unstable due to the negative-U effect in their formation energy [110]. Two of them will "react" with each other and result one negatively charged and one positively charged defect centre, O_N^- and O_N^+ [111]. O_N^- with a reduced distance to one of its second nearest Al ion can generate a donor level deeply below the conduction band (DX-centre, see figure 4.7 (a)) [112]. Therefore a high ionisation energy (about 1.6 eV theoretically calculated in [112] and more than 2 eV experimentally extrapolated in [113]) is required to obtain a sufficient n-type electrical conductivity. The positively charged defects, O_N^+, are located in undistorted matrix. Through Coulomb interaction they can be easily attracted by the triply negative charged Al vacancies, V_{Al}^{3-}, and thus produce a defect complex $(V_{Al}\text{-}O_N)^{2-}$ (see figure 4.7 (b)) [110], which generate an acceptor level above valence band of AlN.

By measuring the absorption coefficient of single crystalline AlN, J. Pastrnak and L. Roskovcova pointed out for the first time that the broad absorption band observed below the AlN band gap correlates with O-associated defect [115]. Its energetic position varies from about 4.80 eV (258 nm) for lower O concentration to 4.53 eV (274 nm) for higher O concentration. Recent spectral characterisations revealed that optical excitation of those two bands results in two independent defect luminescence peaks located in UVA and blue-violet region respectively, which call for two individual excitation paths [116, 117, 118, 119]. By using electron paramagnetic resonance (EPR), electron nuclear double resonance (ENDOR) and optically-detected EPR S. Schweizer reported that the UVA luminescence, excited by higher energy, involves the carrier recombination between above mentioned O_N^--donor and $(V_{Al}\text{-}O_N)^{2-}$-acceptor (donor-acceptor-pair (DAP)) [114]. As delineated in figure 4.8 (a) extracted from the reference [119], a photonic energy E_{exc}

(a) O_N^- **(b)** $(V_{Al} - O_N)^{2-}$ **(c)** $(V_{Al} - 2O_N)^-$

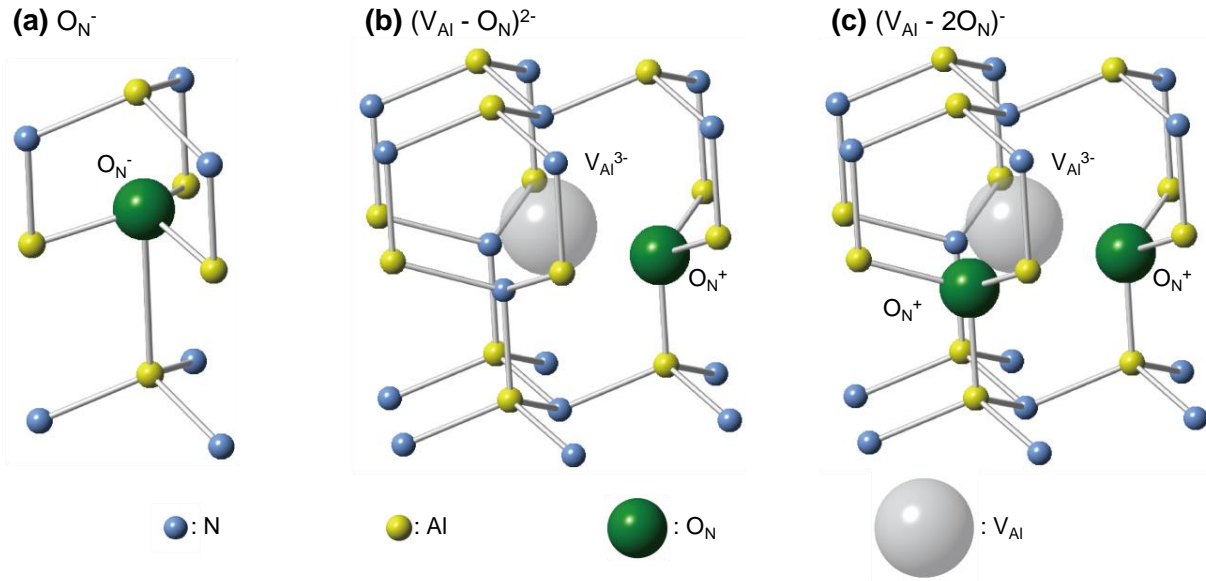● : N   ● : Al   ● : O_N ● : V_{Al}

Figure 4.7: Atomic structures of O-associated defects in AlN (redrawn on the base of the references [112, 114]): (a) singly negative charged O_N^- (DX-centre), defect complex formed by triply negative charged Al vacancy with one and two singly positive charged O: (b) $(V_{Al}\text{-}O_N)^{2-}$ and (c) $(V_{Al}\text{-}2O_N)^-$.

of about 4.80 eV is sufficient to ionise $(V_{Al}\text{-}O_N)^{2-}$-centres and excite electrons into the conduction band of AlN (step 1). The hot electrons are free moveable for a short period of time (step 2) until they are captured by O_N^--traps (step 3). Finally, the UVA light emission follows with the carrier recombination from O_N^--traps to its nearby ionised $(V_{Al}\text{-}O_N)^{2-}$-centres (step 4).

Despite the lack of experimental evidences on the atomic structure it is reasonable to speculate that in terms of higher O concentration, formation of the defect complex, which combines more than one O_N^+ with V_{Al}^{3-}, e.g. $(V_{Al}\text{-}2O_N)^-$, will be more preferential (see figure 4.7 (c) as an assumed atomic structure of this complex). In energy band diagram illustrated in figure 4.8 (b) the $(V_{Al}\text{-}2O_N)^-$-centre may form an acceptor level lying slightly above the $(V_{Al}\text{-}O_N)^{2-}$-level. Through DAP recombination process (as shown in figure 4.8 (b)), a blue-violet defect luminescence, which were observed not only in the references [115, 119, 120] but also in present work (figure 4.6), can be generated by the excitation energy of ca. 4.5 eV.

Excitation of lanthanide luminescence centres via O_N^--$(V_{Al}-2O_N)^-$-pair

As mentioned above, defect luminescence arising from carrier recombination in O_N^--$(V_{Al}\text{-}2O_N)^-$-pairs has a broad peak centred approximately at 2.8 eV. Through comparison with the energy diagram of lanthanide $4f$-levels (figure C.1), it is compelling to denote that this luminescence peak overlaps with the energy required to directly excite the $^1P_2$-level of Pr^{3+} (2.75 eV), ^4I_J-levels of Sm^{3+} ($J = 7/2, 11/2, 13/2$ at 2.7 - 2.8eV), $^5D_4$-level of Tb^{3+} (2.54 eV) and $^1G_4$-level of Tm^{3+} (2.59 eV). Figure 4.9 shows the PLE spectra of these lanthanide doped AlN layers. The lanthanide luminescence intensities are thereby integrated and plotted against excitation energy (as mentioned in section 2.5.2). After
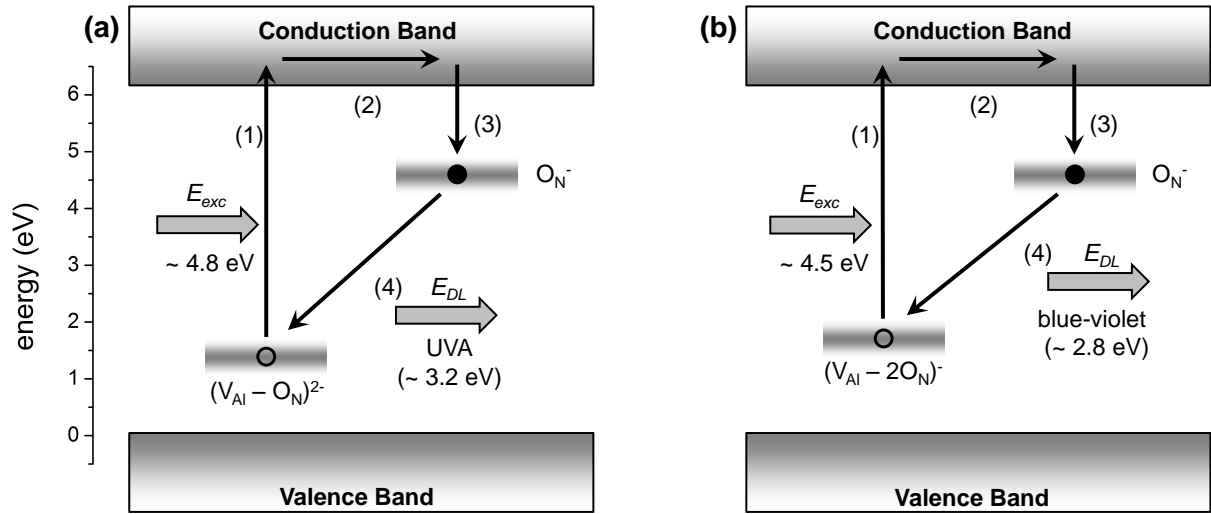
Figure 4.8: Schematic illustration of excitation mechanism of O-associated defect luminescence in AlN: (a) O_N^--$(V_{Al}$-$O_N)^{2-}$-pair and (b) O_N^--$(V_{Al}$-$2O_N)^-$-pair. Description is given in the text.

30 minutes annealing at 500 °C and 1000 °C one can clearly observe an excitation peak located at about 4.5 eV (see figure 4.9 (a) and (b)). This energy is coincident with the one to excite the defect luminescence from O_N^--$(V_{Al}$-$2O_N)^-$-pair (figure 4.6 (b)). In figure 4.10 (a) and (b), integrated intensity of the luminescence originated from defects, Sm^{3+} and Tm^{3+} centres are plotted against annealing temperatures. They are obtained through Gaussian fitting as illustrated in figure 4.10 (c) and (d) for instance. We can conclude from these figures, as well as figure 4.1, 4.3 and 4.6, that at intermediate annealing temperatures (300 - 600 °C), the defect luminescence intensity reaches its maximum (black line in figure 5.10 (a) and (b)), and the luminescence from $^4G_{5/2}$ - ^6H_J ($J = 5/2, 7/2, 9/2$) transitions of Sm^{3+} (red line in figure 4.10 (a)) and $^1G_4$ - $^3H_6$ transition of Tm^{3+} (blue line in figure 4.10 (b)) are also intensified.

Intensity of defect luminescence is proportional to the number of excited O_N^--$(V_{Al}$-$2O_N)^-$ pairs. Based on its temperature-dependence as shown in figure 4.10 (a), (b) and the discussions in section 4.2.1, we may speculate that, if annealing temperature rises, more and more O_N^--$(V_{Al}$-$2O_N)^-$ pairs are formed and they are thermally stable up to the temperature of approximately 500 °C. By further temperature increase, not only the concentration of O ions in AlN but also their mobility increases. The O impurities, which were relatively isolated in the inner AlN core at lower temperatures, may precipitate or diffuse to the O-rich outer shell and build AlN-Al_2O_3 polytypoid structure with fewer periods. Thus, the density of isolated O ions decreases and so the intensity of defect luminescence reduce. Because there are merely no differences between the excitation spectra shown in 4.9 (a) and (b)[4], we must conclude that even after annealing at 1000 °C there are still an adequate amount of O_N^--$(V_{Al}$-$2O_N)^-$ pairs remained to excite the lanthanide centres.

The correlated development of lanthanide and defect luminescence in AlN may reveal that the lanthanide luminescence centres can be resonantly excited by O-associated defect pairs as descript as follows:

---

[4] Except for AlN:Tm, which will be discussed at the end of this section.
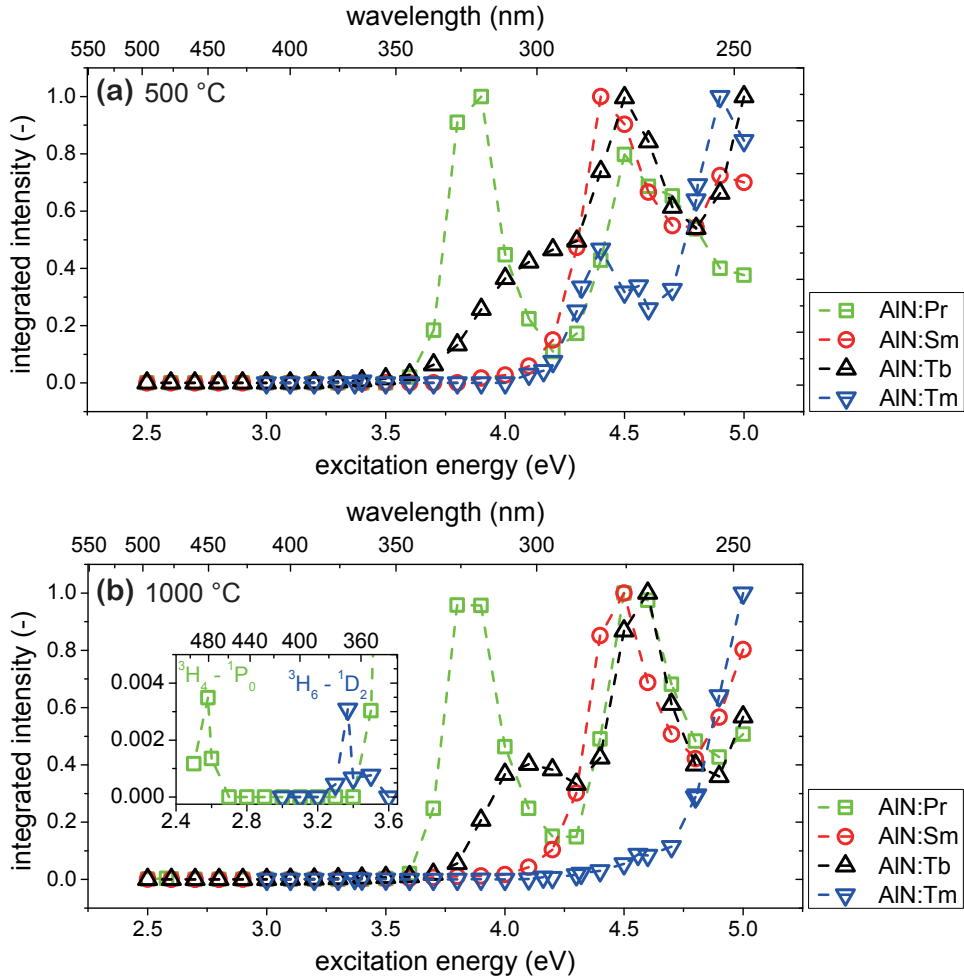
Figure 4.9: Room temperature PLE spectra of AlN:Pr-, AlN:Sm-, AlN:Tb- and AlN:Tm-layers annealed at (a) 500 °C and (b) 1000 °C for 30 minutes. Luminescence peaks of the visible transitions ($^1P_1$ - $^3H_5$ and $^1P_0$ - $^3H_5$ of Pr^{3+}; $^4G_{5/2}$ - $^6H_{5/2,7/2,9/2}$ of Sm^{3+}, $^5D_4$ - $^7F_{3,4,5,6}$ of Tb^{3+}; $^1D_2$ - $^3F_4$ and $^1G_4$ - $^3H_6$ of Tm^{3+}) are integrated and plotted against excitation energy. The intensity maxima of each layer are normalised to unity. The peaks shown in the enlarged part of PLE spectra between 2.4 - 3.6 eV (sub-diagram in (b)) correspond to the direct excitation.

1. *Excitation of O_N^--$(V_{Al}$-$2O_N)^-$ defect pairs*
   The O_N^--$(V_{Al}$-$2O_N)^-$ pairs are optically excited according to the mechanism illustrated in figure 4.8 (b).

2. *Energy transfer from excited O_N^--$(V_{Al}$-$2O_N)^-$ pairs to lanthanide luminescence centres*
   Because the decay time of O-associated defect luminescence (ca. 10 minutes [119]) is five to eight magnitude times than the typical value of lanthanide luminescence (in the order of several microseconds or even milliseconds [121, 122, 123]), energy released by carrier recombination of O_N^--$(V_{Al}$-$2O_N)^-$ pairs should be preferentially transferred into lanthanide luminescence centres. We believe that a non-radiative energy transfer, e.g. Förster resonance energy transfer (FRET, for more details see section 5.2.1) [124], plays a dominant role. The smaller is the difference between the
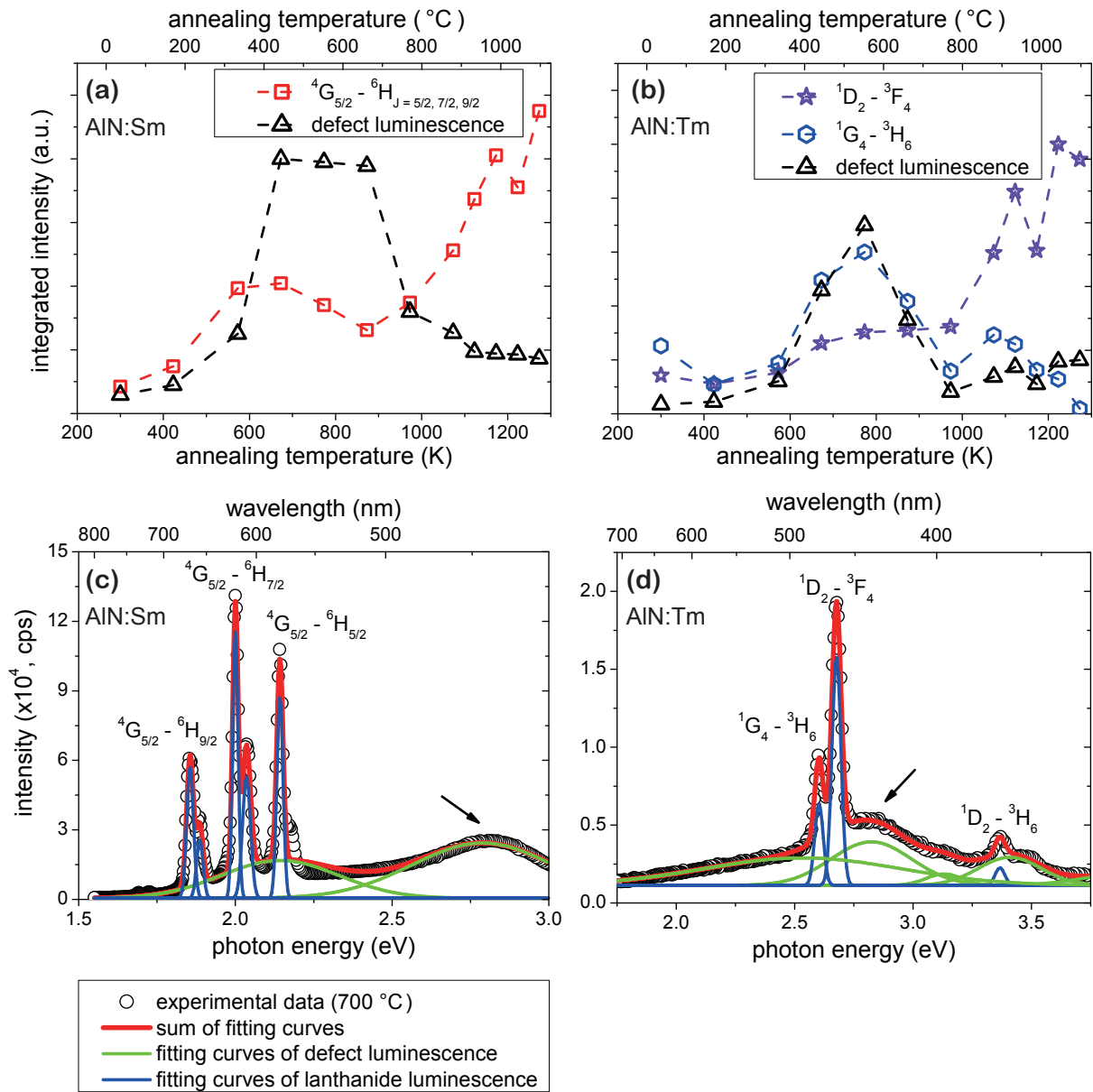
Figure 4.10: Correlation between the temperature-dependence of integrated photoluminescence intensity originating from lanthanide luminescence centres and O-associated defect in AlN (O_N^--$(V_{Al}$-$2O_N)^-$ pairs, centred at 2.8 eV). Results of (a) AlN:Sm and (b) AlN:Tm are shown here for example. Due to different behaviour respect to the defect luminescence, the luminescence intensity stemming from the transitions $^1G_4$ - $^3H_6$ and $^1D_2$ - $^3F_4$ in AlN:Tm are plotted separately. (c) and (d) are PL spectra and fitting curves of the corresponding layers which were annealed at 700 °C. The arrow points to the considered defect luminescence.

energy released by the defect complex and the energy required to directly excite the $4f$-electrons of lanthanide ions, the higher is the energy transfer probability between them.

3. *Radiative relaxation of excited lanthanide luminescence centres*
   The excited $4f$-electrons of lanthanide centres are relaxed to their ground state or lower energetic states by emitting light.
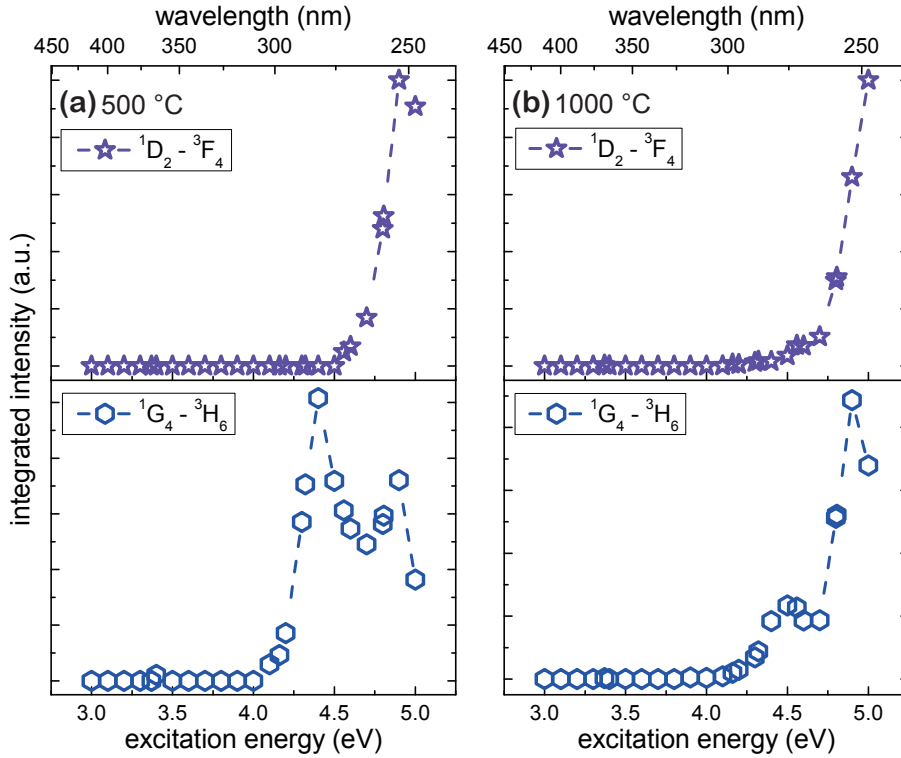
Figure 4.11: PLE spectra of two blue lines generated by the transitions $^1D_2$ - $^3F_4$ and $^1G_4$ - $^3H_6$ in the AlN:Tm layer after 30 minutes annealing at (a) 500 °C and (b) 1000 °C.

An important evidence to support this resonant excitation is the different response of the two blue luminescence peaks of Tm to defect pair assisted excitation: Exciting the O_N^--$(V_{Al}$-$2O_N)^-$ pairs with photonic energy of 4.5 eV, the energy released thereby (ca. 2.8 eV) is sufficient to populate the $^1G_4$ level of Tm (2.59 eV). PLE spectra of the transition $^1G_4$ - $^3H_6$ exhibit therefore an excitation peak centred around 4.5 eV (cf. blue lines in figure 4.11 (a) and (b)). And its temperature-dependence is in consistent with that of O_N^--$(V_{Al}$-$2O_N)^-$ pairs (cf. blue and black lines in figure 4.10 (b)). In case of another blue luminescence generated by the transition $^1D_2$ - $^3F_4$, however, the energy stored by O_N^--$(V_{Al}$-$2O_N)^-$ pairs is insufficient to populate the $^1D_2$ level (3.37 eV), hence no correlation between them can be found (cf. violet lines in figure 4.10 (b), 4.11 (a) and (b)). As the luminescence intensity of this transition is dominant in the layers annealed at 1000 °C, an excitation peak around 4.5 eV in the corresponding PLE spectra is hardly to be observed (figure 4.9 (b)).

Due to limitation of utilised xenon light source the AlN:Ln layers cannot be excited if the photon energy is higher than 5.0 eV. But the PLE spectra of them exhibit an increasing tendency. Energy transfer from the excited band-tail levels and O_N^--$(V_{Al}$-$O_N)^{2-}$ defect complexes to lanthanide centres may play an important role therein. We can thence conclude at the end of this section that, in the case of below band gap excitation the defect states associated with O impurities in the AlN host are essential to generate lanthanide luminescence.

4.3 Effects of thermal annealing on lanthanide luminescence intensity

Based on our experimental results (cf. section 4.1) and literature [98, 125, 126] we confirm that through a short-time thermal annealing, the lanthanide luminescence in AlN:Ln can be significantly intensified. This is most likely because of the thermally activated atomic rearrangement and recovery processes of host material, which, for example, facilitate the formation of new lanthanide luminescence centres and assist the excitation and radiative relaxation processes by reducing band tail states and quenching centres (see section 4.3.1). In section 4.3.2 we define a concept of "extended lanthanide luminescence centres" to simplify the description on the thermal enhancement of lanthanide luminescence intensity.

4.3.1 Thermally activated atomic recovery of host material and its potential influences on lanthanide luminescence

Despite of different production processes it is commonly agreed that the existence of a large number of native point defects and unintentional impurities is unavoidable in the as-prepared AlN [127, 128]. In general, energy states formed thereby are perfect carrier traps. Depending on the nature of those defects (the atomic structure, the position of corresponding energy states in the band gap and the lifetime of trapped carriers etc.), they can either enhance or suppress the lanthanide luminescence intensity.

As demonstrated in figure 4.1 - 4.3, luminescence of lanthanide ions doped in AlN appears intensified after annealing, in particular at higher temperatures. A.R. Zanatta suggested that the thermal treatments initiate considerable atomic rearrangement and short range diffusion in AlN [98]. The interstitial ions, for example, may diffuse to their energetically favourable substitutional sites. In addition, the N vacancies introduced during the layer deposition may annihilate with the Al vacancies, which are incorporated by unintentional
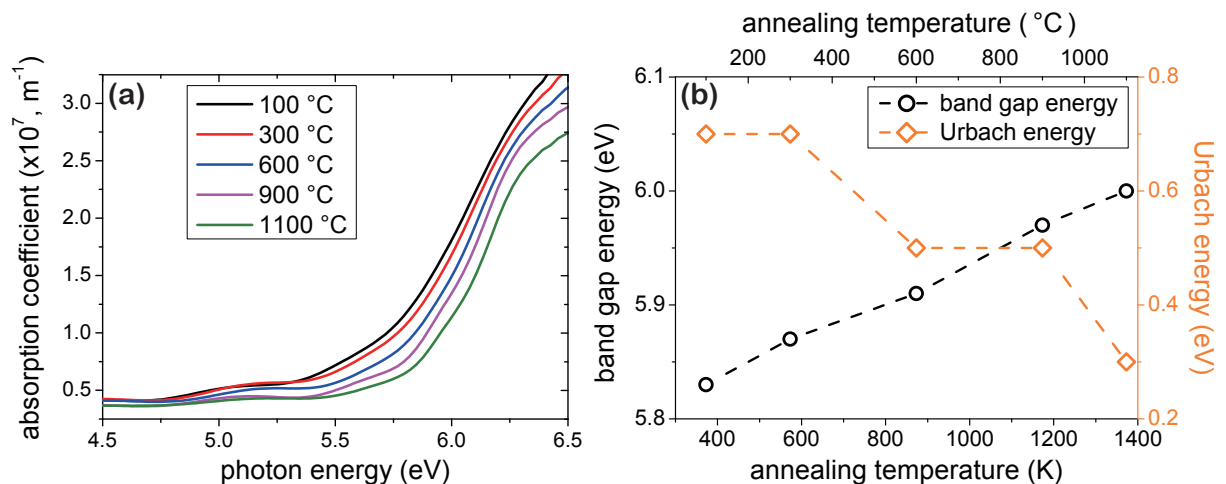

Figure 4.12: (a) Optical absorption coefficient of AlN:Tm layers after annealing at different temperatures and (b) development of the optical band gap energy and the Urbach energy as temperature increases (results are adopted from [129]).

O impurities [102]. Since these native defects build shallow states within the band gap of AlN [127], effects of thermal recovery can be experimentally confirmed. Figure 4.12 (a) shows the plots of absorption coefficients of AlN:Tm layers against its photon energy after 30 minutes annealing at different temperatures. The absorption coefficients are calculated from the results of optical transmission measurements (cf. section 2.5.1). With increasing annealing temperature the optical absorption at low-energetic region reduces (curves shift to the right). And as graphically fitted by using equation 2.8a and 2.8b, the optical band gap energy E_g of AlN host increases, whereas the Urbach energy E_U, as an indicator of band-tail states, drops (see figure 4.12 (b))[5].

Unfortunately, the detailed mechanisms of thermal recovery and their influence on the lanthanide luminescence intensity are so far not deeply understood. With the help of our results in the present and previous works, we propose three basic processes to delineate the effects of thermal annealing on luminescence intensity of lanthanide in AlN:

1. *Enhancement of the number of lanthanide luminescence centres by reordering their local symmetry*

   Analysis on the crystal field splitting of luminescence spectra presented in the previous chapter show that the majority of radiative lanthanide ions doped in AlN are substitutionally placed on Al sites and exhibit C_{3v} symmetry. B.D. Vries implanted the radioactive lanthanide isotopes into single crystalline GaN and demonstrated by emission channelling measurements that thermal treatments increase the proportion of substitutional lanthanide ions and thus enhance their luminescence intensity [88]. Our preliminary measurements of X-ray Absorption Fine Structure (XAFS)[6] also evince little changes in the absorption spectra of in AlN doped Tb before and after annealing at 1000 ℃. This might be further evidence on thermal rearrangement of lanthanide and its neighbouring ions. Figure 4.13 (a) illustrates the diffusion of a interstitial lanthanide ion to its substitutional site in AlN.

2. *Enhancement of lanthanide excitation by establishing new excitation paths and reducing band-tail states*

   Some kinds of proper electron transitions between the energy states induced by defects and/or defect complexes provide additional paths to assist the excitation of lanthanide luminescence centres. As discussed in section 4.2.2, energy transfer from, e.g., excited O_N^--$(V_{Al}$-$2O_N)^-$ pairs, may be an essential mechanism for below-band-gap excitation of lanthanide ions. Annealing the AlN:Ln layers at appropriate temperatures benefits the formation of those defect states.

   Large number of shallow defect states below the conduction band [130, 131], on the other hand, are in competition with electron trapping in O_N^- deep state [119]. As can be seen in figure 4.13 (b), the relaxation of hot electrons in those shallow states may impede energy transfer into lanthanide centres. Atomic recovery processes activated by thermal treatments markedly reduce the density of such band-tail states

---

[5] An example how to obtain E_g and E_U is illustrated in figure B.3 (a) of appendix B.

[6] XAFS measurement was thankfully done by Dr. Stefan Mangold, who works in the institute of Synchrotron radiation (ISS), Karlsruhe Institute of Technology. The ANKA synchrotron was used thereby as excitation source. Detailed results are not shown in this dissertation.
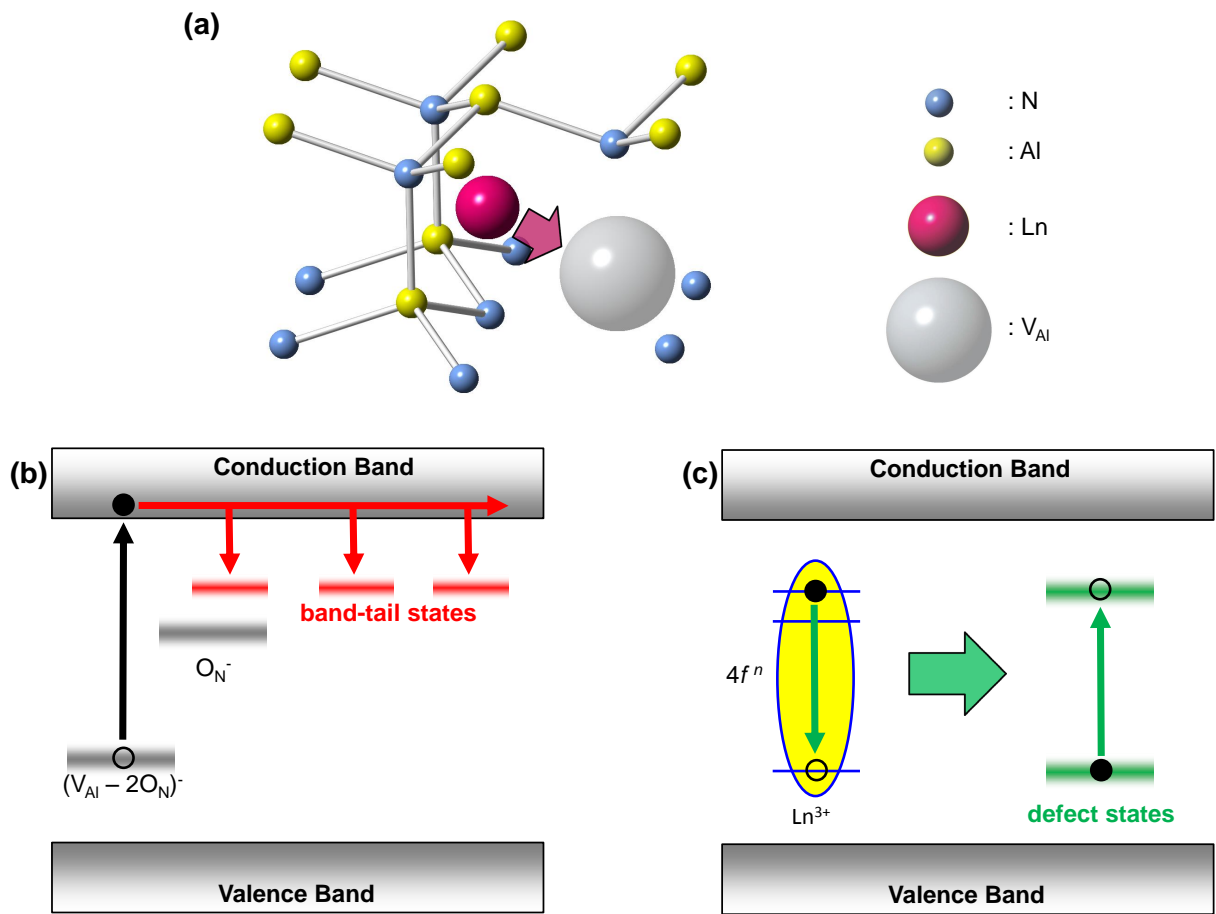
Figure 4.13: Sketch of (a) diffusion of a interstitial lanthanide ions (on the T site of AlN) to its nearby Al vacancy, (b) relaxation of hot electrons in the shallow states below conduction band edge of AlN and (c) Energy back transfer from excited lanthanide to defect states within the band gap of AlN.

(cf. figure 4.12), and thus increase the probability of electrons trapped by O_N^- states and the consecutive excitation of lanthanide centres.

3. *Enhancement of lanthanide radiative relaxation processes by suppressing the quenching centres*
   Beside the radiative relaxation, there are a lot of processes which lead to non-radiative relaxation of excited lanthanide luminescence centres. Energy back transfer from excited lanthanide to defect states, designated as quenching centres, is one of them [132] (as schematically delineated in figure 4.13 (c)). Thermal annealing may remove these defect states and therefore facilitate the radiative relaxation process.

The list of mechanisms suggested above is in fact far from comprehensive. Through elaborate investigations to identify each kind of crystal defects in a given host material, characterising its thermal stability and analyse its respective influences on the excitation and radiative relaxation of each $4f$-transition in lanthanide luminescence centre, one might be able to precisely reveal the effects of thermal annealing on lanthanide luminescence. Obviously such work is extremely complicate and tedious. Because all possible

mechanisms promoted by thermal annealing are related to the ordering of lattice structure and recovery of crystal defect, we may consider the thermal enhancement of lanthanide luminescence intensity as a generalised thermally activated process. Based on this, we propose in next section a thermodynamic and kinetic description of this general effect.

4.3.2   Model of lanthanide luminescence enhancement via thermal annealing

Energy path ways

Figure 4.14 is a schematic overview, which shows how the excitation energy absorbed in a lanthanide-doped semiconductor system can be used to generate lanthanide luminescence. In general two energy path ways need to be considered:

- *Path 1: Excitation of lanthanide luminescence centres via semiconductor host and their relaxation*
  In case of indirect excitation of lanthanide luminescence centres, the incident energy is primarily absorbed and "stored" in the semiconductor host material. As discussed in previous sections, trapping of free carriers by O-associated defect states could be one of the probable ways for this. Energy released by the carrier recombination is able to be transferred into lanthanide luminescence centres. Additionally, due to differences in the ionic radius as well as the difference in the electron negativities between lanthanide and Al ions, H.J. Lozykowski and his co-worker suggested that the trivalent lanthanide dopant and its clusters in AlN may also provide energy states within the band gap. They trap the excited carriers of opposite charge and form excitons bound to their vicinity (rare earth structured isovalent traps) [97]. Subsequent non-radiative energy-transfer process from bound exciton will lead to the excitation of lanthanide luminescence centres. Nevertheless, regardless the details of different excitation process, we may introduce a collective rate coefficient k_1 to describe the energy storage by the host material, and $k_{Ln,1}$ the subsequent non-radiative energy transfer into lanthanide luminescence centres.
  Once a centre is excited, they will relax their energy via intra-$4f$ transitions either radiatively, with rate coefficient $k_{Ln,r}$, or non-radiatively, with rate coefficient $k_{Ln,nr}$. Multi-phonon relaxation, energy back transfer process, thermalisation, Auger energy transfer into conduction band or alternative energy states for example are considered to be responsible for the latter case [132, 133].

- *Path 2: Other excitation and relaxation processes without energy transfer into lanthanide luminescence centre*
  Obviously, not all of the excitation energy can be stored in the host and further be used to excite lanthanide luminescence centres. Despite of the light reflection on the AlN:Ln layer surface and the interface between layer and substrate, all the electronic processes without subsequent energy transfer into lanthanide centres are in competition with the processes described in path 1. We set the corresponding rate coefficient as k_2.
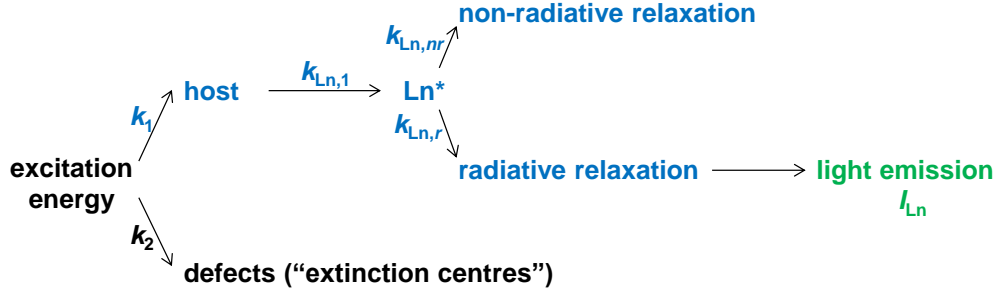
Figure 4.14: Excitation and relaxation process diagram of a lanthanide doped semiconductor system.

Description of lanthanide luminescence intensity by solving rate equation

By using the rate coefficients mentioned above and solving the rate equation formulated in our previous work [63]

$$\frac{\mathrm{d}P_{\mathrm{Ln}^*,1}(t)}{\mathrm{d}t} = k_{\mathrm{Ln},1} - k_{\mathrm{Ln},r}P_{\mathrm{Ln}^*,1} - k_{\mathrm{Ln},nr}P_{\mathrm{Ln}^*,1}, \qquad (4.1)$$

the population of excited lanthanide luminescence centres $P_{\mathrm{Ln}^*,1}(t)$ can be expressed by

$$P_{\mathrm{Ln}^*,1}(t) = \frac{k_{\mathrm{Ln},1}}{k_{\mathrm{Ln},r} + k_{\mathrm{Ln},nr}} + C_1 \exp[-(k_{\mathrm{Ln},r} + k_{\mathrm{Ln},nr})t], \qquad (4.2)$$

where C_1 is a constant and the subscript 1 denotes the energy path 1. The first term of this equation denotes the population of excited centres at steady state and the second term its relaxation to the steady state. The instantaneous luminescence intensity from one luminescence centre $\mathrm{d}I_{\mathrm{Ln},1}$ is proportional to the change in population of its excited state due to radiative relaxation:

$$\mathrm{d}I_{\mathrm{Ln},1} = k_{\mathrm{Ln},r}P_{\mathrm{Ln}^*,1}(t) = \frac{k_{\mathrm{Ln},1}k_{\mathrm{Ln},r}}{k_{\mathrm{Ln},r} + k_{\mathrm{Ln},nr}} + C_1 k_{\mathrm{Ln},r} \exp[-(k_{\mathrm{Ln},r} + k_{\mathrm{Ln},nr})t]. \qquad (4.3)$$

The exponent term in this equation describes the temporal relaxation of luminescence intensity. As introduced in section 2.5.2, in the room temperature PL measurement the layers were radiated by a xenon arc lamp without interruption. The measuring time t_m (1 s) was much longer than the decay time of lanthanide luminescence (typically μs - ms). Thus this exponent term is negligible if the instantaneous intensity is integrated over t_m. Further assuming that the part of intensity loss due to other factors, which have nothing to do with the optoelectronic processes, e.g. surface reflection, are identical for each layer and taking the competitive effect of path 2 into account, the observed luminescence intensity is a function of rate coefficients:

$$I_{\mathrm{Ln},1} \approx C_{exp} \cdot \frac{k_1}{k_1 + k_2} \cdot \frac{k_{\mathrm{Ln},1}k_{\mathrm{Ln},r}}{k_{\mathrm{Ln},r} + k_{\mathrm{Ln},nr}} \cdot N_{LLC}, \qquad (4.4)$$

where C_{exp} represents an instrumental constant and N_{LLC} the number of lanthanide luminescence centres (LLC) in host.

Thermally activated formation of "extended lanthanide luminescence centres" as a homogenous reaction

As discussed in section 4.3.1, thermal annealing activates short range atomic diffusion processes in semiconductor host, which may reorder the local symmetry of lanthanide dopants and alter their excitation and relaxation processes by modifying the related defect states within the band gap. On this account, the number of lanthanide luminescence centres and all the rate coefficients in equation 4.4 depend on annealing temperature and duration. And the prediction of lanthanide luminescence intensity by using this equation becomes extremely difficult. Fortunately we are able to evade this problem by defining the concept of "*extended lanthanide luminescence centres*" (ELLC):

The ELLC include not only the lanthanide ions, which are doped in an appropriate semiconductor host with non-centrosymmetric crystal field environment (namely the lanthanide luminescence centres), but also all processes and mechanisms, which are of assistance for and in competition to their excitation and radiative relaxation. The total number of extended lanthanide luminescence centres N_{ELLC} is therefore a function of annealing temperature T (in K) and duration t_{ann} and defined according to equation 4.4 as:

$$N_{ELLC}(T, t_{ann}) = \frac{k_1}{k_1 + k_2} \cdot \frac{k_{\mathrm{Ln},1} k_{\mathrm{Ln},r}}{k_{\mathrm{Ln},r} + k_{\mathrm{Ln},nr}} \cdot N_{LLC}. \tag{4.5}$$

In this way the thermal rearrangement of lattice structure and recovery of crystal defects can be practically interpreted as a thermally activated process to form extended lanthanide luminescence centres. Different to the traditional solid state phase transformation, this process doesn't follow the nucleation-growth mechanism. Its probability to occur is same for all positions in the system throughout. So we may adopt the thermodynamics and kinetics of homogenous reaction to describe it [134, 135], and rewrite N_{ELLC} as:

$$\begin{aligned} N_{ELLC}(T, t_{ann}) &= N_{ELLC}^i + f(t_{ann})[N_{ELLC}^f(T) - N_{ELLC}^i] \\ &= N_{ELLC}^i + f(t_{ann})\Delta N_{ELLC}(T), \end{aligned} \tag{4.6}$$

where $f(t_{ann})$ is defined as the progress of this reaction during the annealing (namely the degree of transformation in [134] with $0 \leq f \leq 1$), N_{ELLC}^i and $N_{ELLC}^f(T)$ are constants, which represent the total number of ELLC before and after annealing at temperature T respectively. The difference of them, $\Delta N_{ELLC}(T)$, quantises the maximum number of ELLC activated at T and can be represented by an Arrhenius equation:

$$\Delta N_{ELLC}(T) = \Delta N_{ELLC}(\infty) \exp\left(-\frac{E_f}{kT}\right), \tag{4.7}$$

where k is Boltzmann constant, $\Delta N_{ELLC}(\infty)$ the increase of the number of ELLC at infinite temperature and E_f the generalised formation energy of ELLC. This energy is a collective thermodynamic notion and consists of all the energies required for different kinds of atomic rearrangement and recovery processes.

In case of isothermal annealing the kinetics of thermal ordering process $f(t_{ann})$ can be descript through the Kissinger analysis for the first-order homogeneous reaction with the

form [136]

$$f(t_{ann}) = 1 - \exp(-k_f \cdot t_{ann}), \tag{4.8}$$

where k_f is the formation rate. With increasing annealing duration t_{ann}, f increases and asymptotically approaches unity.

Mathematical expression of the model and its applications

Substitute the equations 4.5 - 4.8 into 4.4, we are able to describe the effects of thermal annealing on lanthanide luminescence intensity by using only two thermodynamic and kinetic quantities, namely generalised formation energy E_f and formation rate k_f of extended lanthanide luminescence centres:

$$I_{\text{Ln},1} \approx A + B \cdot \exp\left(-\frac{E_f}{kT}\right) \cdot [1 - \exp(-k_f \cdot t_{ann})], \tag{4.9}$$

where

$$A = C_{exp} \cdot N^i_{ELLC} \tag{4.10a}$$

$$B = C_{exp} \cdot \Delta N_{ELLC}(\infty) \tag{4.10b}$$

are constants. As demonstrated in figure 4.15, if the annealing temperature is constant, the system with lower k_f value needs more time to construct ELLC and reaches its maximum luminescence intensity (cp. blue and green curves). At lower annealing temperature, the total number of ELLC decreases, which lead to a reduced maximum luminescence intensity (cp. blue and red curves).

Isothermal developments of lanthanide luminescence intensity as shown in figure 4.2 are fitted by equation 4.9, in which the term $\exp(-E_f/kT)$ is kept as a constant. Unfortunately, we are unable to obtain rational k_f values in AlN:Sm and AlN:Tb systems, because the luminescence intensity is already reached or very closed to its maximum value, even though the layer is annealed only for 5 minutes. One reason for this may be the strong assistance of O-associated defect states in the lanthanide excitation (section 4.2), which could be easily generated at the very beginning of annealing. Therefore one may expect that the resulting k_f values are relative high. In figure 4.2 (a) and (b) we set $k_f = 0.4/\text{min}$ to illustrate the trend of experimental results. In order to precisely determine those values, annealing duration should be shorter than 5 minutes.

It can be concluded by comparing the figure 4.2 (c) to 4.2 (a) and (b) that the formation rate of ELLC, and thus the rate of enhancement of luminescence intensity, in AlN:Tm layers is obviously slower than that in AlN:Sm and AlN:Tb. Insufficient assistance of O-associated defect states on the excitation of Tm ions may be an excellent explanation for this phenomenon. As experimentally demonstrated in section 4.2.2, although one of the blue luminescence emitted by $^1G_4$ - $^3H_6$ transition of Tm can be generated through energy transfer from these states, the energy released from them is not large enough to generate another transition, $^1D_2$ - $^3F_4$, which becomes more dominant in the spectrum after annealing (cf. figure 4.1 (d) and 4.10 (b)). Formation of extended luminescence centres in this case may be governed by other processes with slower rates (recovery of band-tail states and reduction of quenching centres etc.). And smaller k_f values are ob-
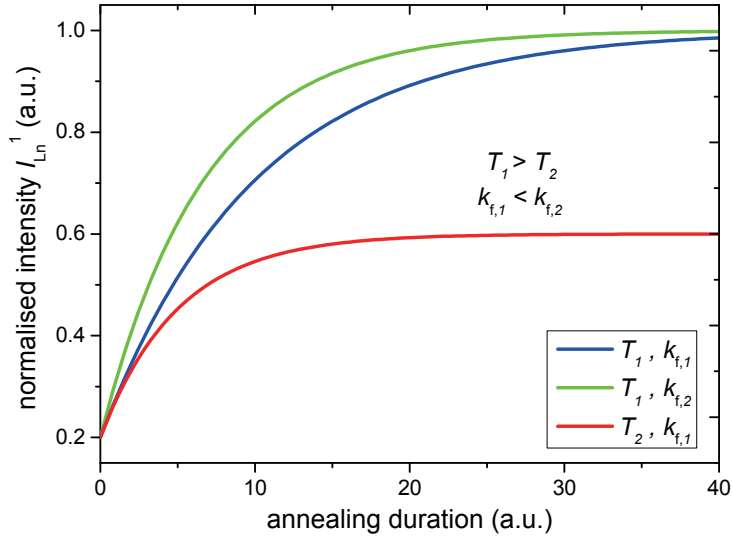
Figure 4.15: Effect of thermal annealing on luminescence intensity of lanthanide doped in AlN. The influences of temperature T and formation rate of ELLC k_f thereon are shown. The intensity maximum is normalized to unity.

tained (see table 4.1).

As can be seen in figure 4.3, integrated intensity of visible luminescence in all systems generally increases as annealing temperature rises. Annealing duration of the layers was set to be 30 minutes. Hence, according to the results in figure 4.2, it is reasonable to believe that the formation of extended luminescence centre is basically complete and the term $1 - \exp(-k_f \cdot t_{ann})$ in equation 4.9 is approximate to unity. Neglecting the intensity drop in AlN:Pr system above 950 °C and the luminescence enhancement of oxygen-associated defect states at intermediate temperatures, we are able to graphically estimate the generalised formation energies E_f. The fitted results are listed in table 4.2.

Table 4.1: Formation rate of extended lanthanide luminescence centres k_f (in 1/min) for AlN:Tm layers at different annealing temperatures. Values are graphically fitted in figure 4.2 by using equation 4.9.

temperature	500 °C	700 °C	1000 °C
k_f	0.34	0.17	0.15

Table 4.2: Generalised formation energy of extended lanthanide luminescence centres E_f (in eV) for AlN:Pr, AlN:Sm, AlN:Tb and AlN:Tm layers. Values are graphically fitted in figure 4.3 by using equation 4.9.

lanthanide ions	Pr^{3+}	Sm^{3+}	Tb^{3+}	Tm^{3+}
E_f	0.73 ± 0.25	0.39 ± 0.08	0.99 ± 0.24	0.35 ± 0.11

4.4   Conclusions

In this chapter we experimentally demonstrated that the luminescence intensity of lanthanide doped in AlN can be significantly enhanced by appropriate thermal treatments. This procedure promotes a series of local atomic rearrangements, which alter the energy states within the band gap of AlN.

Formation of defect complexes constituted by unintentional impurities is one consequence of the thermal annealing. Through comparison with the results in literatures we may confirm that the broad luminescence peak centred at about 2.8 eV in AlN with and without lanthanide doping is derived from recombination of the carriers trapped by O-associated defect pairs, O_N^--$(V_{Al}$-$2O_N)^-$. Energy released thereby overlaps the energy required to directly excite some certain $4f$ levels of lanthanide ions. On account of this the presence of these defect pairs will promote the lanthanide excitation, and therefore enhance the intensity of lanthanide luminescence. Thermal annealing at intermediate temperatures, namely 300 - 600 °C, is found to be favoured to generate this kind of defect. And the resulting luminescence intensities originating from defects and lanthanide centres are correlated and reach a maximum at this temperature region.

We further believe that the atomic rearrangement and recovery activated by thermal annealing may play an important role in the reduction of electronic processes, which compete with the excitation and radiative relaxation of lanthanide luminescence centres. This effect is more conspicuous at higher annealing temperatures. As a result, the luminescence intensity of AlN:Ln layers can be significantly enhanced. By introducing a concept of "extended lanthanide luminescence centre" (ELLC) and adopting the thermodynamics and kinetics of homogenous reaction, intricate thermal influences on lanthanide luminescence intensity are successfully simplified and modelled with only two variables: generalised formation energy and formation rate of ELLC: E_f and k_f.

Lanthanide luminescence enhancement via engineering of a new excitation path - resonance excitation by $Al_xIn_{1-x}N$ quantum dots

As investigated in previous chapter, lanthanide luminescence centres can be excited through energy transfer from the energy states within the band gap of host material, which are produced by unintentionally incorporated defects. With this inspiration one may engineer the band structure of host material by introducing some "defect states" which provide additional paths to excite the lanthanide luminescence centres. One potential way is to adopt nanocrystallite with appropriate band gap. In the last two decades, improved optoelectronic properties of transition metal ions [137] and lanthanide ions [138, 139, 140] doped in proper nanocrystals or quantum dots were frequently reported. Decreasing the size of crystallite below a certain critical dimension leads to a significant increase of luminescence intensity.

$Al_xIn_{1-x}N$ is considered to be an adequate host material for this purpose because it has a large miscibility gap of its nitride components, namely AlN and InN, under conventional conditions. Through respective selection of the concentration, annealing temperature and duration, In-rich $Al_xIn_{1-x}N$ nanoparticles can be generated due to decomposition. They exhibit a dimension of several nanometres as well as, according to their size, tunable and much smaller band gap than the surrounding Al-rich phases. Hence they can be considered as quantum dots. If the band gap energy of those In-rich $Al_xIn_{1-x}N$ nanoparticles fulfils the resonance condition with the levels to be excited in the lanthanide ions, an efficient energy transfer from the particles to the lanthanide luminescence centres may occur.

At the beginning of this chapter, thermodynamics and kinetics of decomposition of polycrystalline $Al_xIn_{1-x}N$ layers are analysed with the help of electron microscopic investigations (section 5.1). The size of resulting In-rich particles in $Al_{0.87}In_{0.13}N$:Tm layers and their coarsening during thermal annealing at 700 °C is quantified as an example. Subsequently, the quantum confinement effects of In-rich particles and its assistances in the

excitation of lanthanide luminescence centres are considered in section 5.2. A model is postulated to quantitatively describe the significant changes of luminescence intensity in $Al_{0.87}In_{0.13}N$:Tm and $Al_{0.84}In_{0.16}N$:Pr during the annealing.

5.1 Decomposition in $Al_xIn_{1-x}N$ system

In order to establish the model to describe the resonant excitation of lanthanide luminescence centres by In-rich $Al_xIn_{1-x}N$ nanoparticles, the first step is to ascertain the size and composition of decomposed particles. This can be achieved through analysis on the thermodynamics (section 5.1.1) and kinetics (section 5.1.2 and 5.1.3) of $Al_xIn_{1-x}N$ decomposition, which are based on our experimental results.

5.1.1 Thermodynamic considerations

Decomposition is essentially a phase separation process in multi-component liquid and solid state systems. According to a regular solution model, the molar Gibbs free energy of mixing ΔG_m of a binary system A_xB_{1-x} at temperature T (in K) is given by:

$$\Delta G_m = \Delta H_m - T \cdot \Delta S_m, \tag{5.1}$$

where

$$\Delta H_m = \Omega x(1-x) \tag{5.2}$$

is the molar enthalpy of mixing, and

$$\Delta S_m = -R\left[x\ln x + (1-x)\ln(1-x)\right] \tag{5.3}$$

is the molar entropy of mixing, Ω and R are the interaction parameter and gas constant respectively. If $\mathrm{d}^2\Delta G_m/\mathrm{d}x^2$ at a given temperature is negative, the system is instable against compositional fluctuation, and spinodal decomposition takes place. It consists of spontaneous formation of periodic domain structures with significant different chemical composition. The miscibility gap on the phase diagram is defined by the binodal curve, where the chemical potentials of the components in each phase are identical. A system within the concentration range between binodal and spinodal curve is metastable. The phase separation follows the conventional nucleation-growth mechanism.

Due to large lattice constant mismatch a wide miscibility gap can be expected in most of the ternary III-V alloys. Since 1950s ample theoretical works were invested to determine their enthalpy of mixing ΔH_m [141, 142]. The Delta Lattice Parameter model (DLP model) [143] is one of the most successful instrument, in which the ternary III-V alloys $A_xB_{1-x}C$ are considered as pseudo-binary systems (AC-BC). And the enthalpy of mixing $\Delta H_m^{\mathrm{DLP}}$ is determined by molar atomisation enthalpies of their solid state components, namely $\Delta H_{at,\,AC}(s)$, $\Delta H_{at,\,BC}(s)$ and $\Delta H_{at,\,A_xB_{1-x}C}(s)$:

$$\Delta H_m^{\mathrm{DLP}} = x \cdot \Delta H_{at,\,AC}(s) + (1-x) \cdot \Delta H_{at,\,BC}(s) - \Delta H_{at,\,A_xB_{1-x}C}(s). \tag{5.4}$$

Calculated curves based on equation 5.1 to 5.4 are usually considered as chemical binodal and spinodal curves [144], because additional energy barriers generated by long-wavelength modulation of composition and strain are neglected. Those energy barriers prevent the system from instability to infinitesimal compositional fluctuation and therefore decrease critical temperature and shrink miscibility gap to the coherence binodal and spinodal curves.

Another appropriate approach is the Valence Force Field model (VFF Model) [145]. It is frequently used to obtain coherent binodal and spinodal curves for a system with zink-blende structure, but its results are also applicable in their hexagonal phases [13, 146, 147, 148]. The molar enthalpy of mixing H_m^{VFF} is equivalent to the total microscopic elastic strain energy, which arises from the bond distortion. Assuming that the lattice of a ternary III-V alloy is elastically fully relaxed up to second nearest neighbour ions for example, the alloy can be considered as a mixture of five types of tetrahedral sublattice $A_x B_{1-x} C$ with $x = 0$, 0.25, 0.5, 0.75 and 1 [149] (correspond to type I - V as shown in figure D.1 of appendix D). Ions of group III (A and B) with the distance determined by the Vegard's law [150] are fixed at each vertex. And the centre-lying C ion is placed at the position where the elastic energy is minimised. The molar enthalpy of mixing equals the sum of elastic strain energy E^{VFF} over all tetrahedra:

$$\Delta H_m^{\mathrm{VFF}} = C^{\mathrm{VFF}} \cdot \sum_{n=\mathrm{I}}^{n=\mathrm{V}} E_n^{\mathrm{VFF}} P_n^{\mathrm{VFF}}, \tag{5.5}$$

where C^{VFF} is a constant to convert the result into molar unit and depends on the number of relaxed ion shell to be considered, P_n^{VFF} a concentration-dependent coefficient which presents appearance probability of each type of tetrahedron [149] and

$$E^{\mathrm{VFF}} = \frac{3}{8} \sum_{i=1}^{4} \alpha_i \frac{d_i^2 - d_{i0}^2}{d_{i0}^2} + \frac{6}{8} \sum_{i=1}^{4} \sum_{j=i+1}^{4} \frac{\beta_i + \beta_j}{2} \frac{\left(d_i d_j \cos \theta_{ij} + \frac{d_{i0} d_{j0}}{3} \right)}{d_{i0} d_{j0}}. \tag{5.6}$$

α_i and β_i represent bond-stretching and bond-bending force constant parameters of centre-lying ion to its i-th neighbor ion respectively. d_i and d_{i0} are the equilibrium bond length between them in the ternary alloy and the binary compounds, respectively. θ_{ij} is the angle between the vectors linking centre-lying ion to its i-th and j-th neighbors.

In this work we respectively use DLP and VFF model to estimate the chemical and coherent decomposition curves for $Al_x In_{1-x} N$ system. They are plotted in figure 5.1, in which solid lines denote the binodal and dashed lines the spinodal. Related details of the calculations are introduced in appendix D. Critical point of chemical decomposition is lying at AlN content $x_{\mathrm{AlN}} = 0.57$ with temperature $T_c = 4516$ K and that of coherent decomposition is at $x_{\mathrm{AlN}} = 0.53$ with $T_c = 1338$ K. The later value is in reasonable agreement with the result obtained by first principle total energy calculations ($T_c = 1485$ K) [151]. Through elaborate adjustment of sputter powers on Al and In containing target the $Al_x In_{1-x} N$ layers in whole composition region are able to be produced (cf. section 2.1), even if the composition is located in the miscibility gap. During thermal annealing phase
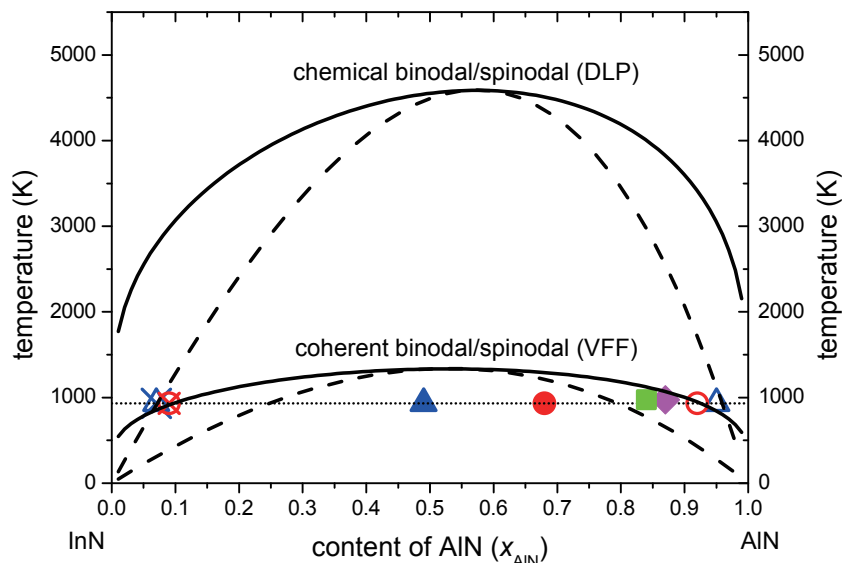
Figure 5.1: Chemical and coherent binodal (solid lines) and spinodal (dashed lines) decomposition curves of $Al_xIn_{1-x}N$ system respectively calculated by DLP and VFF model. Horizontal dotted line denotes the annealing temperature of 660 °C (933 K). Blue solid triangle and red circle represent the composition of two selected $Al_xIn_{1-x}N$:Er layers with $x_{AlN} = 0.49$ and 0.68 before annealing (determined by ICP-OES). Blue hollow triangles and red hollow circles with and without cross represent the composition of decomposed In- and Al-rich phases, which were determined by EDS analysis as shown in figure 6.2. Purple diamond and green quadrat indicate the composition of $Al_{0.87}In_{0.13}N$:Tm and $Al_{0.84}In_{0.16}N$:Pr before annealing at 700 °C (973 K), which will be discussed in following sections.

separation arises, which leads to formation of Al- and In-rich $Al_xIn_{1-x}N$ phases. This process can be demonstrated by electron microscopy. Figure 5.2 (a) shows a STEM high-angle annular dark field (HAADF) cross-sectional image of an $Al_{0.49}In_{0.51}N$:Er layer, which was annealed at 660 °C for 30 minutes [152]. Since the ionic mass and the radius of In are much larger than that of Al, the bright regions in the image represent In-rich phases. Results of an EDS line scan (yellow line on figure 5.2 (a)) clearly identified that the selected In-rich $Al_xIn_{1-x}N$ nanoparticle with about $x_{AlN} = 0.38$ and 13 nm diameter is wrapped by the Al-rich phase with about $x_{AlN} = 0.96$ (see figure 5.2 (b)). Taking the thickness of this TEM specimen[1] (about 20 nm) into account, x_{AlN} of In-rich particle is corrected to 0.08.

In comparison to $Al_{0.49}In_{0.51}N$:Er, it seems that $Al_{0.68}In_{0.32}N$:Er-layer after 30 minutes annealing at 660 °C (Fig. 5.2 (c)) exhibits finer In-rich nanoparticles with $x_{AlN} = 0.09$ (determined by EDS point measurement at point A, with specimen thickness correction) [152]. The AlN content of Al-rich phases is 0.92 (measured at point B). AlN content of In- and Al-rich phase in both layers are marked in figure 5.1 with blue hollow triangles

---

[1] Through EDS measurement one obtains integrated compositional information through the specimen. If the diameter of In-rich nanoparticle is smaller than the TEM specimen thickness, the measured content of AlN within In-rich phase, $x_{AlN}^{In-rich,m}$, will be higher than what it really is. The correction is carried out by the relation $x_{AlN}^{In-rich,m}d_s = x_{AlN}^{In-rich}d + x_{AlN}^{Al-rich}(d_s - d)$, where $x_{AlN}^{In-rich}$ and $x_{AlN}^{Al-rich}$ denote the actual AlN contents at In-rich and Al-rich region, d_s and d are TEM sample thickness and diameter of In-rich nanoparticle.
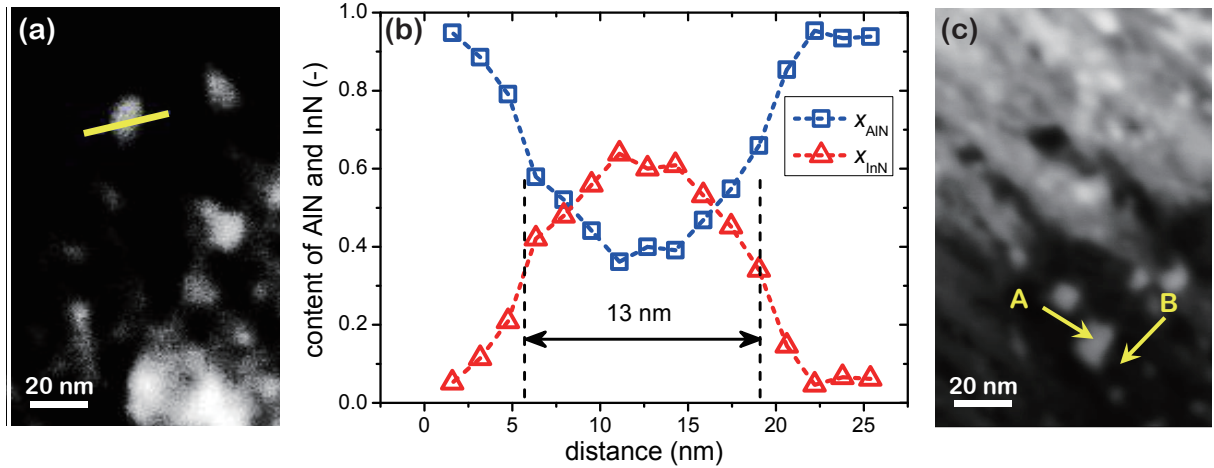
Figure 5.2: STEM HAADF cross-sectional image of a $Al_xIn_{1-x}N$:Er film with $x_{AlN} = 0.49$ after annealing at 660 °C (a). Variations of metallic concentration measured by EDS line scan along the yellow line are plotted in (b). (c) is a STEM HAADF cross-sectional image of a $Al_xIn_{1-x}N$:Er film with $x_{AlN} = 0.68$ after annealing at 660 °C. Two EDS point measurements were carried out at position A and B. These results are adopted from [152].

and red hollow circles with and without cross. They are in perfect accordance with the calculated coherent binodal curve.

As will be further discussed in section 5.2, the resonant excitation of lanthanide luminescence by Al-rich nanoparticles can be detected in $Al_{0.87}In_{0.13}N$:Tm and $Al_{0.84}In_{0.16}N$:Pr systems. The composition of them before annealing at 700 °C, as shown in figure 5.1 (purple diamond and green quadrat), lie between the coherent spinodal and binodal curves. Hence one might expect that the decomposition during the annealing should follow the nucleation-growth mechanism. Although some more detailed microscopic investigations are required, due to columnar polycrystalline structure of the layers we may by contrast deduce that the spinodal decomposition (or a mixture of spinodal and binodal decomposition) occurs. According to the Surface mode of Coherence Spinodal Decomposition model (SCSD model) suggested by M. Tang [153], sample surface and grain boundary are preferred nucleation sites for spinodal decomposition. At those areas the elastic strain energy is significantly relaxed. As a result, the corresponding critical temperature shifts to higher temperature and the spinodal decomposition range becomes wider and closes to the chemical one. In the following two sections, formation and coarsening of decomposed In-rich nanoparticles in $Al_{0.87}In_{0.13}N$:Tm layers will be experimentally and, based on spinodal decomposition, theoretically analysed.

5.1.2 Formation of the decomposed In-rich $Al_xIn_{1-x}N$ particles

Experimental observations of rapid decomposition

The decomposition process in $Al_xIn_{1-x}N$ is observable by appropriate experimental investigations. Figure 5.3 (a) - (e) present *in situ* TEM bright field cross section images of an $Al_{0.87}In_{0.13}N$:Tm layer during thermal annealing at 700 °C. Combined with STEM-HAADF investigation it can be demonstrated that the In-rich $Al_xIn_{1-x}N$ nanoparticles (correspond to dark points in bright field and bright points in HAADF image, figure 5.3 (f)) are created at the very beginning of the annealing procedure 5.3 (a)[2]. And intuitively they are located preferentially on the grain boundary, which satisfies the condition to use SCSD model. As further annealing, formation of new particles are hardly to be detected (cp. Figure 5.3 (b) - (f) to 5.3 (a)).
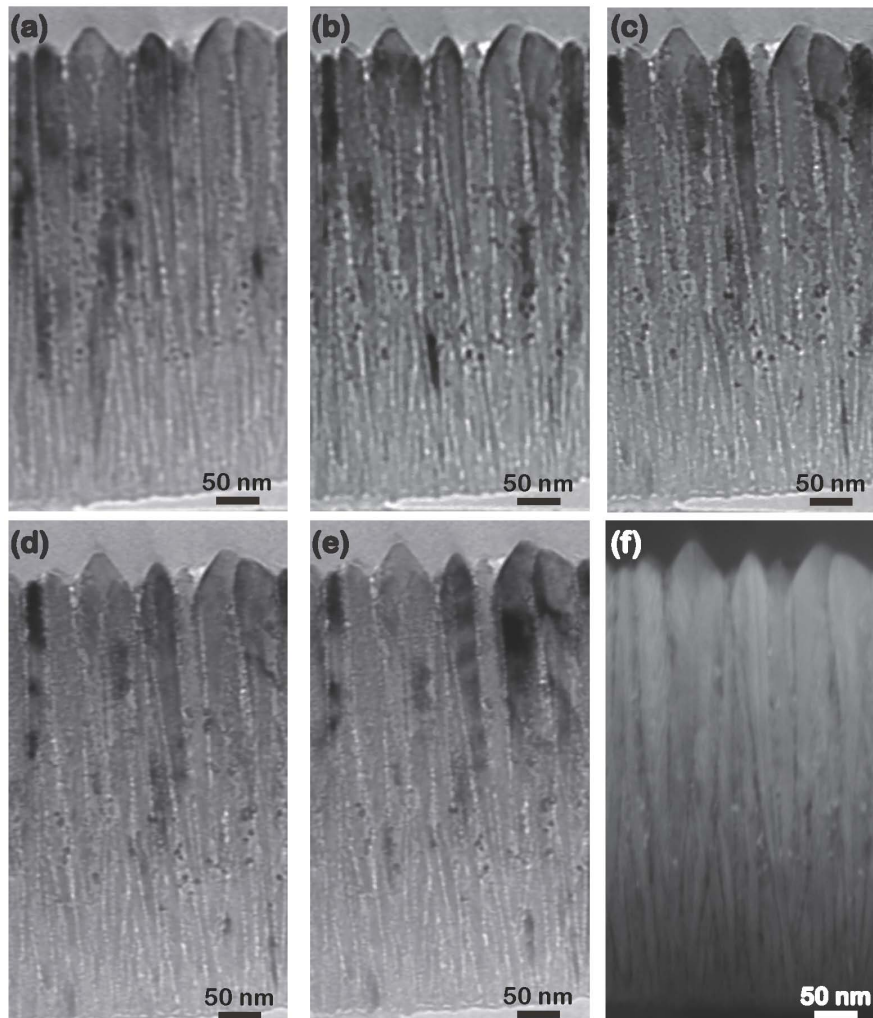

Figure 5.3: *in-situ* TEM bright field cross section images of spinodal decomposition of $Al_{0.87}In_{0.13}N$:Tm layer annealed at 700 °C: (a) 0s; (b) 1min 44s; (c) 2min 34s; (d) 4min 41s; (e) 10min 20s and (f) the STEM-HAADF imaging after 10min 30s annealing at same position.

---

[2] Actually, In-rich $Al_xIn_{1-x}N$ nanoparticles were already formed before the annealing temperature reaches 700 °C (heating duration: 2 min). But due to thermal expansion the sample holder was not stable during the heating and thus no clear image can be collected.
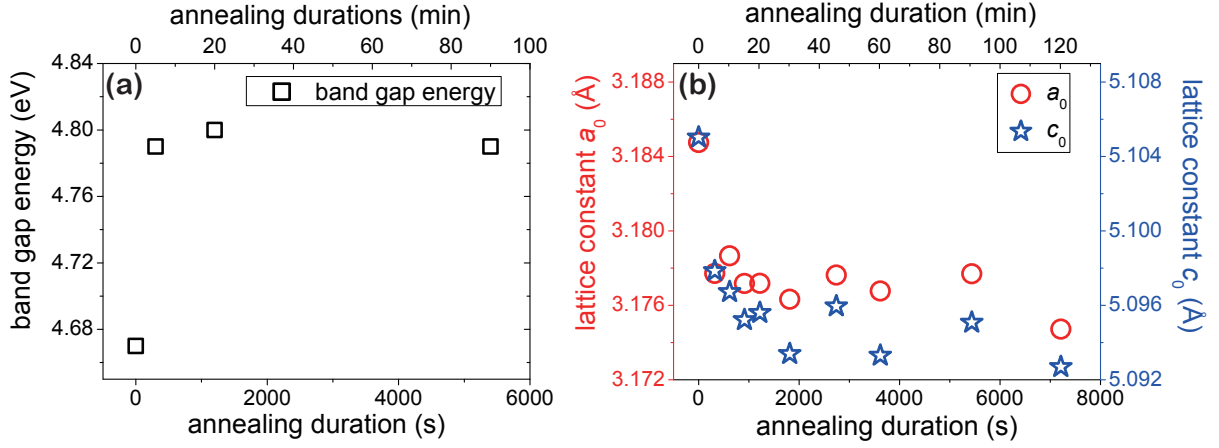
Figure 5.4: Variation of strain-free lattice constants and optic band gap energy of $Al_{0.84}In_{0.16}N$:Pr layers in dependence of annealing duration at 700 °C. Results are recorded from [155].

If the content of AlN in as-prepared $Al_xIn_{1-x}N$ layer is much higher than that of InN, volume fraction of decomposed Al-rich phase will be much larger than that of In-rich. This dominant phase changes the macroscopic features of the layers after annealing, which provide other evidences for the rapid decomposition and can be experimentally detected. One can see from Figure 5.4 (a) that as thermal annealing proceeds, the stress-free lattice constants of $Al_{0.84}In_{0.16}N$:Pr layers, a_0 and c_0, are significantly reduced at the very early stage of annealing and gradually approach saturated values ($a_0^{AlN} < a_0^{InN}$, $c_0^{AlN} < c_0^{InN}$). The results are determined by XRD with $\sin^2 \Psi$-method (see section 2.3.1) and listed in table B.2 of appendix B. In consistence with the decrease of lattice constants, we can also find an increase of band gap energy (because of $E_g^{AlN} > E_g^{InN}$) as shown in figure 5.4 (b)[3]. Obviously these results are merely qualitative information.

Calculation of In-rich $Al_xIn_{1-x}N$ embryo size

In order to precisely predict the coarsening of In-rich nanoparticles during annealing and on this basis to understand their assistance in the excitation of lanthanide luminescence centres (for details see section 5.2), it is inevitable to understand the formation kinetics of these particles. However, the rapid decomposition as shown above and simultaneous coarsening make the experimental determination of particle size at initial stage of decomposition (as $t_{ann} \rightarrow 0$) impossible. Hence we can only use a theoretical way as described as follows to calculate it:

Consider a binary solid state system (A-B) located within spinodal decomposition curve ($d^2\Delta G_m/dx^2 < 0$), which exhibits a one-dimensional sinusoidal compositional fluctuation with amplitude C_β and wavenumber β along direction z:

$$c_B(z, o) - c_0 = C_\beta \cdot \exp(i\beta z), \tag{5.7}$$

---

[3] Thermal relaxation of internal stress is another factor to alter the band gap energy. However, the changes caused thereby are energetically much weaker than the increase as shown in figure 5.4 (b) (ca. 130 meV). During the annealing the variation of biaxial elastic internal stress in the $Al_{0.84}In_{0.16}N$:Pr layers is about 1 GPa (table B.3 of appendix B). The stress dependent band gap shift in GaN for example is 24 meV/GPa [154].

where c_0 indicates the average composition. If spinodal decomposition takes place, its compositional variation of component B with time t can be expressed as [156]:

$$c_B(z,t) - c_0 = C_\beta \cdot \exp(i\beta z) \cdot \exp(Rt). \tag{5.8}$$

The amplification factor R, which determines the decomposition rate, is a function of β:

$$R = -\tilde{D}_B \beta^2 \left(1 + \frac{2\delta^2 E}{f''(1-\nu)} + \frac{2\kappa}{f''}\beta^2 \right), \tag{5.9}$$

where $\tilde{D}_B$ is the chemical interdiffusion coefficient of component B and negative in case of spinodal decomposition, δ the fractional change in lattice parameter $d\ln a$ per unit compositional change dx_B ($\delta = d\ln a/dx_B$), E the elastic modulus, $f'' \leq 0$ the second derivation of local free energy per molecule[4] [157] against composition x_B, ν the Poisson's ratio and κ the gradient-energy coefficient (in energy per length). The second term within the braket of equation 5.9, with a negative value, represents the influences of elastic energy and adjusts the onset of spinodal decomposition from $f'' \leq 0$ to $f'' \leq -2\delta^2 E/(1-\nu)$. The third term, which is also negative, prevent occurrence of decomposition from a compositional fluctuation with larger β.

The dimension of the In-rich region due to local compositional fluctuation (defined as embryo of decomposed In-rich Phase) is represented by the half of fluctuation wavelength $\lambda/2$, which is proportional to β inversely. As can be seen in the schematic plot of R against $\lambda/2$ (figure 5.5), the spinodal decomposition occurs, only if the size of In-rich region is larger than a critical value ($\lambda_{crit}/2$). Hence we define these regions as the embryos of spinodal decomposition. If the embryo size equals a certain value, say $\lambda_m/2$, the amplification factor R, viz. the decomposition rate, reaches its maximum. One can further identify from figure 5.5 that due to smaller $\lambda_{crit}/2$ the initiation of spinodal decomposition is preferred at the region with lower elastic energy. And for a given fluctuation wavelength, the decomposition rate is significantly larger in the region with lower elastic energy than that with higher energy.

In terms of polycrystalline $Al_xIn_{1-x}N$:Ln layers with columnar grains it is reasonable to assume that the elastic energy is fully relaxed on the grain boundary and thus second term of equation 5.9 can be set as zero. The decomposition thereon may follow the chemical spinodal curve. Additionally due to low doping concentration of lanthanide ions, its influence on the spinodal decomposition is negligible. According to these considerations and equation 5.9 the critical size of embryo $\lambda_{crit}/2$ and the size with maximal decomposition rate $\lambda_m/2$ can be formulated by κ and f'':

$$\frac{\lambda_{crit}}{2} = 2\pi\sqrt{\frac{\kappa}{-2f''}} \tag{5.10a}$$

$$\frac{\lambda_m}{2} = 2\pi\sqrt{\frac{\kappa}{-f''}}. \tag{5.10b}$$

---

[4] In solid state phase transformation the volume change is often negligible. So the free energy per unit volume f is equivalent to the corresponding free enthalpy $g = \Delta g_m + (1 - x_B)g_A + x_B g_B$.
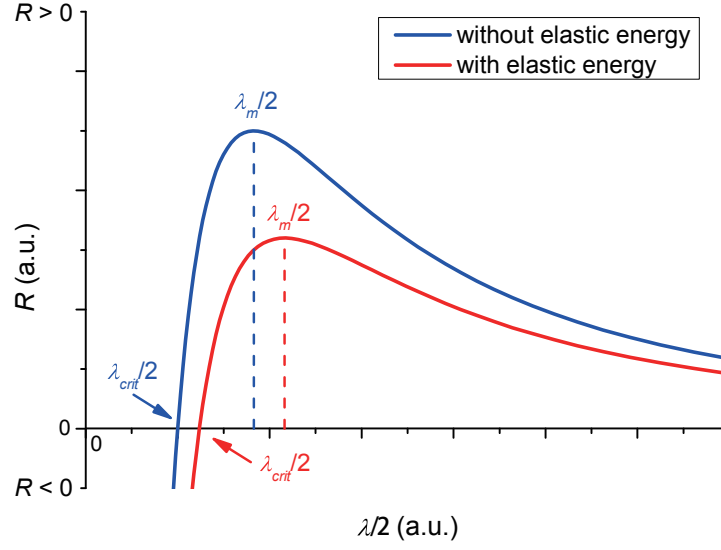
Figure 5.5: Schematic illustration of the dependence of amplification factor R on local compositional fluctuations with wavelength $\lambda/2$ without (blue line) and with (red line) the contribution of elastic energy. $\lambda_{crit}/2$ and $\lambda_m/2$ represent the critical fluctuation wavelength and the wavelength with maximal decomposition rate respectively.

Furthermore, we may consider the hexagonal ternary $Al_xIn_{1-x}N$ system as a pseudo-binary regular solution with zinc-blende structure (face-centred cubic structure)[5] and three types of bonding, Al-N-Al, Al-N-In and In-N-In, for simplification. As estimated by the pairwise interaction model developed by E.A. Lass $et~al.$ [159], κ depends on the interaction energy parameters, $\varepsilon_{Al\text{-}N\text{-}Al}$, $\varepsilon_{In\text{-}N\text{-}In}$ and $\varepsilon_{Al\text{-}N\text{-}In}$ (convert their unity from energy per bond into energy per volume) as:

$$\kappa = \frac{a^2_{c\text{-}Al_xIn_{1-x}N}}{2}(2\varepsilon_{Al\text{-}N\text{-}In} - \varepsilon_{Al\text{-}N\text{-}Al} - \varepsilon_{In\text{-}N\text{-}In}), \tag{5.11}$$

where $a_{c\text{-}Al_xIn_{1-x}N}$ denotes lattice constant of cubic $Al_xIn_{1-x}N$. Taking the enthalpy of mixing ΔH_m

$$\Delta H_m = x_{AlN}(1 - x_{AlN}) \cdot \frac{N_A \cdot a^3_{c\text{-}Al_xIn_{1-x}N}}{n} \cdot \frac{z}{2} \cdot (2\varepsilon_{Al\text{-}N\text{-}In} - \varepsilon_{Al\text{-}N\text{-}Al} - \varepsilon_{In\text{-}N\text{-}In}) \tag{5.12}$$

with the number of group III ions per unit cell $n = 4$ and the coordination number $z = 12$ into account, κ becomes:

$$\kappa = \frac{\Delta H_m}{3a_{c\text{-}Al_xIn_{1-x}N} \cdot x_{AlN}(1 - x_{AlN}) \cdot N_A}. \tag{5.13}$$

Through inserting equation 5.11 - 5.13 in 5.10a and 5.10b, determining f and ΔH_m values by DLP-model and applying the values of heat capacities from [160, 161] for the calculation of f, the resulting formulations of $\lambda_{crit}/2$ and $\lambda_m/2$ are functions of AlN

---

[5] Many references suggested that the calculated results by using thermodynamic quantities of cubic III-nitride systems can be directly transferred to their hexagonal system with less deviation [13, 158].
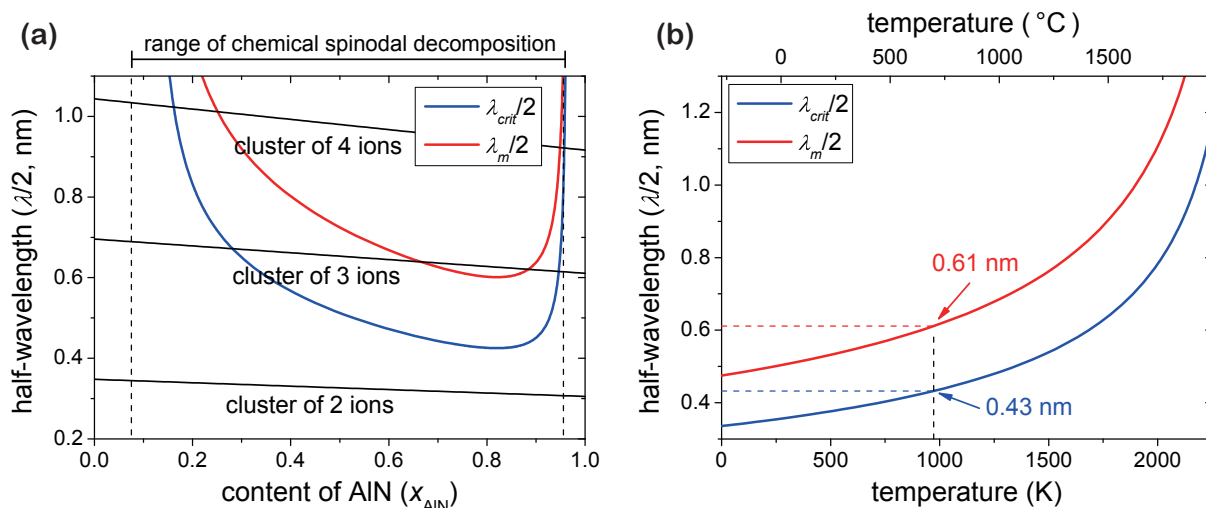
Figure 5.6: Critical half-wavelength ($\lambda_{crit}/2$, blue line) and half-wavelength with maximal decomposition rate ($\lambda_m/2$, red line) in dependence on content of AlN, x_{AlN}, at 700 °C (a) and their temperature dependence of an $Al_{0.87}In_{0.13}N$:Tm sytem (b). In addition, the solid black lines in (a) represent the lengths of 2-, 3- and 4-fold In clusters calculated by using Vegard's law with one dimensional arrangement.

content x_{AlN} and temperature T. As plotted in figure 5.6 (a), developments of calculated $\lambda_{crit}/2$ and $\lambda_m/2$ at annealing temperature of 700 °C are asymmetric within the chemical spinodal decomposition range. Both of them exhibit minimum values at $x_{AlN} \approx 0.82$ and rise to infinity at the boundaries of spinodal region. At a given x_{AlN}, they increase with rising temperature. In the case of $Al_{0.87}In_{0.13}N$:Tm layer, the critical In-rich $Al_xIn_{1-x}N$ embryo size, $\lambda_{crit}/2$, and the one with maximum decomposition rate, $\lambda_m/2$, at 700 °C (973 K) is 0.43 nm and 0.61 nm respectively (see figure 5.6 (b)).

Calculation of In-rich $Al_xIn_{1-x}N$ particle size

In order to obtain the initial In-rich particle size we suggest to consider the local compositional fluctuation as one dimensional clustering of In ions. The distance between two neighbouring In ions is assumed to follow Vegard's law [150]. And the spinodal decomposition proceeds spontaneously if the dimension of n-fold In clusters (cluster with n In ions) larger than the critical size of embryo $\lambda_{crit}/2$. As can be seen in figure 5.6 (a), a 3-fold In cluster is sufficiently large enough to initiate the spinodal decomposition within a wide composition range ($0.27 < x_{AlN} < 0.95$).

We may adopt this geometric consideration directly into three dimensions and assume that all of the group III ions in a volume, where only one 3-fold In cluster can be found, are counted to develop one spherical In-rich $Al_xIn_{1-x}N$ particle surrounded by Al-rich matrices. According to the results of EDS line scan the AlN content, x_{AlN}, of this In-rich particle at 700 °C is about 0.08 and that of its Al-rich surrounding 0.96. One can therefore establish a compositional dependency of In-rich particle diameter d at 700 °C as shown as black line in figure 5.7. With rising x_{AlN}, on the one hand, the particle diameter enlarges and reaches a maximum value at $x_{AlN} = 0.89$. And with further increase of x_{AlN}, it drops precipitously and approaches zero at the spinodal boundary. The reason for this
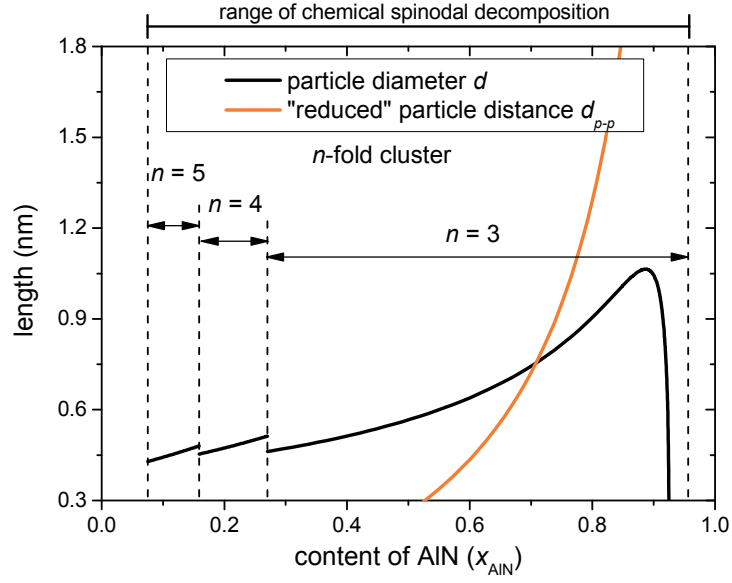
Figure 5.7: Plot of particle diameter d (black line) and "reduced" particle distance d^*_{p-p} (orange line) against Al content x_{AlN}. Because within the lower composition region the critical wavelength is larger than the 3-fold cluster length (cf. figure 5.6 (a)), higher orders of In cluster ($n = 4, 5$) are used to calculate the particle diameter.

consists in the fact that the In content in this region is too low to form the both phases with required x_{AlN}. By decreasing Al content, on the other hand, the particle diameter gradually decreases and closes to a constant value at about 0.5 nm. This is in contrast with reality and can be corrected as follows:

In the practice two In-rich particles with the size d are distinguishable from each other if they are at least separated by doubled interspace of group III ions $2d_{\text{III-III}}$ ($d_{p-p} - d \geq 2d_{\text{III-III}}$, where d_{p-p} is the centre to centre particle distance). Hence we define a "reduced" particle distance as $d^*_{p-p} = d_{p-p} - 2d_{\text{III-III}}$ and plot it against Al content (orange line in figure 5.7). The black and orange lines in figure 5.7 intersect each other at $x_{AlN} = 0.71$. This means that the particulate In-rich phases can be formed in $Al_xIn_{1-x}N$ system by spinodal decomposition at 700 °C only if $x_{AlN} \geq 0.71$. In a system with lower x_{AlN}, d^*_{p-p} is smaller than d. The decomposed In-rich particles are connected together, and a meander structure of In-rich and Al-rich phases or particulate Al-rich phases will be fund.

The calculated initial particle diameter in $Al_{0.87}In_{0.13}N$:Tm layers at the early stage of spinodal decomposition ($t_{ann} \to 0$) by using this method is about 1.0 nm with particle distance d_{p-p} of 2.6 nm.

5.1.3   Coarsening of the decomposed In-rich $Al_xIn_{1-x}N$ particles

Since the coarsening of spinodal decomposed precipitation occurs, in general, simultaneously with its formation, the size of In-rich $Al_xIn_{1-x}N$ particle theoretically predicted in last subsection can hardly be measured experimentally. However, it is an important initial value to predict the development of particle diameter during the annealing.

Coarsening of the precipitation can be considered as an Ostwald ripening process [162]. In 1961, L.M. Lifshitz et al. [163] and C. Wagner [164] solved this problem independently with the assumption that the growth of a spherical second phase precipitation is due to volume diffusion controlled material transport from supersaturated matrix. They proposed an asymptotic enlargement of mean precipitate size $\bar{d}$ with annealing duration t_{ann} as [164]:

$$\bar{d}(t) = \bar{d}(0)\left(1 + \frac{t_{ann}}{\tau}\right)^{\frac{1}{3}}.\tag{5.14}$$

Here $\bar{d}(0)$ is the initial precipitation size and τ a constant with the dimension of time. The corresponding size distribution $f(d, t_{ann})$ follows:

$$f(d, t_{ann}) \equiv \lim_{\Delta d \to 0} \frac{N(d, d + \Delta d, t_{ann})}{\Delta d}$$

$$= \frac{C_{s.d.}}{\left(1 + \frac{t_{ann}}{\tau}\right)^{\frac{4}{3}}} \left[\frac{d}{\bar{d}(t_{ann})}\right]^2 \left[\frac{3}{3 + \frac{d}{\bar{d}(t_{ann})}}\right]^{\frac{7}{3}} \left[\frac{\frac{3}{2}}{\frac{3}{2} - \frac{d}{\bar{d}(t_{ann})}}\right]^{\frac{11}{3}} \exp\left[-\frac{\frac{d}{\bar{d}(t_{ann})}}{\frac{3}{2} - \frac{d}{\bar{d}(t_{ann})}}\right],$$

$$\tag{5.15}$$

where $N(d, d + \Delta d, t_{ann})$ is the number of spherical precipitates with a diameter between d and $d + \Delta d$ per unit volume at t_{ann} and $C_{s.d.}$ a normalisation constant. As we can see in
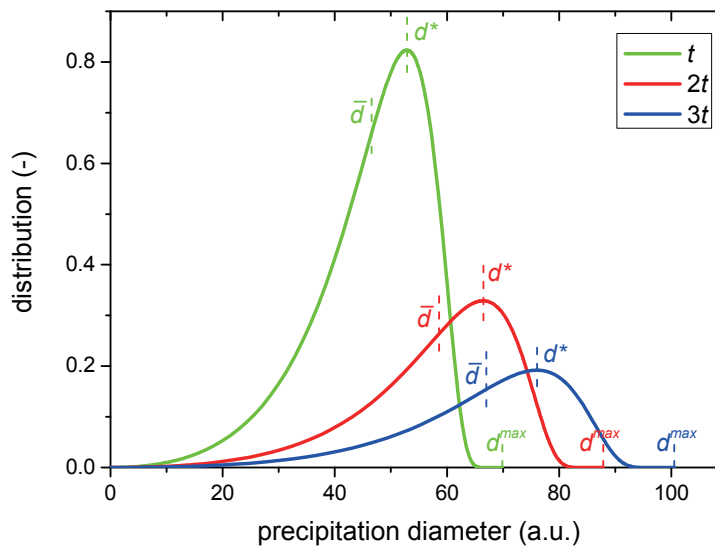

Figure 5.8: Schematic illustration of precipitation size distribution based on diffusion controlled Ostwald ripening at the arbitrary time t, $2t$ and $3t$. The corresponding mean diameter $\bar{d}$, diameter with maximum number d^* and maximum diameter d^{max} are marked on the curves.
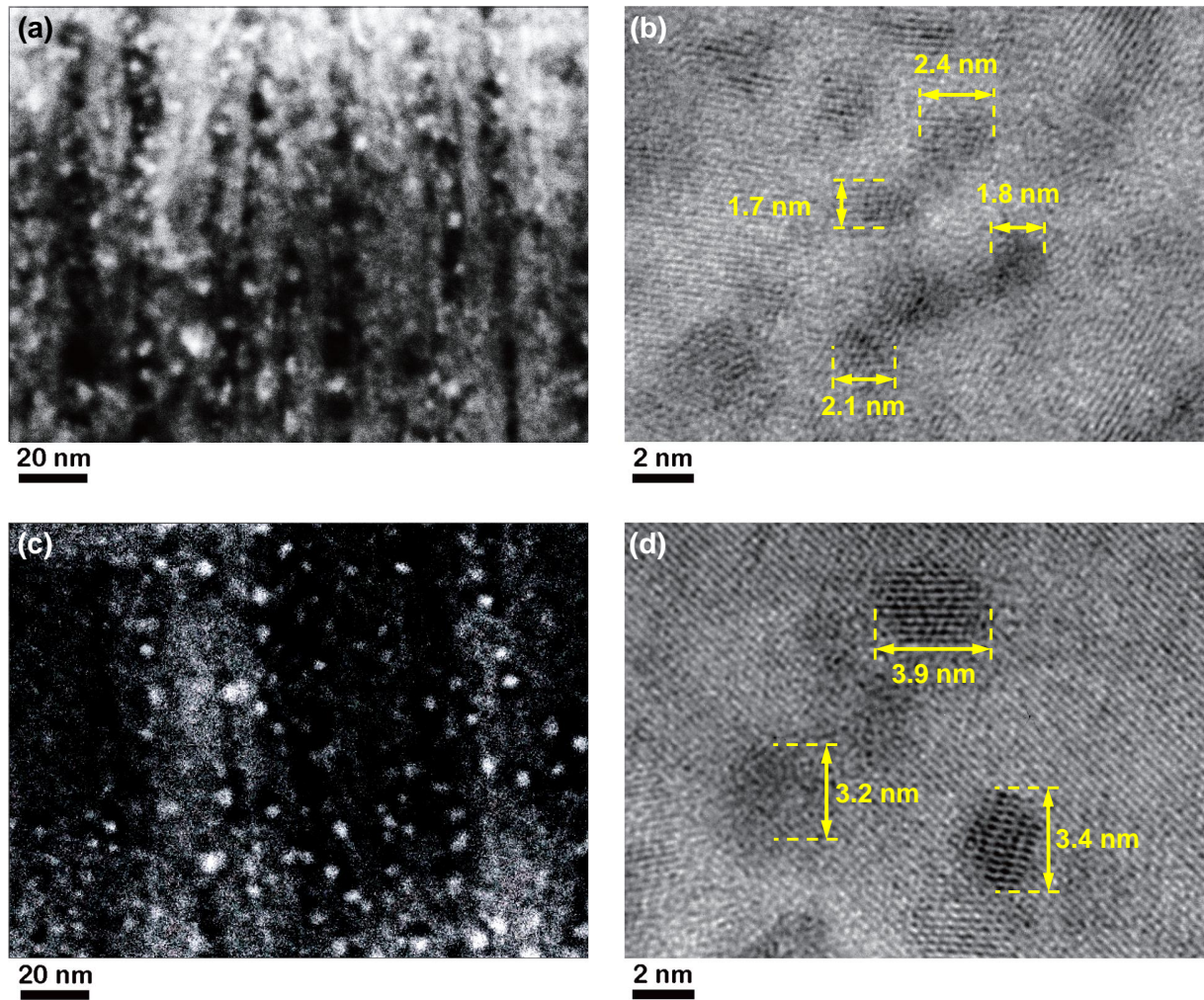
Figure 5.9: STEM-HAADF cross section imaging of $Al_{0.87}In_{0.13}N$:Tm layers annealed at 700 °C after (a) 20 min; (c) 90 min and the corresponding HRTEM imaging (b) (d).

figure 5.8, this size distribution has a cut-off at larger d. The precipitation diameter with maximum number d^* lies above the mean diameter ($d^* = 1.135 \cdot \bar{d}$) and the maximum diameter d^{max} is 1.5 times of the mean diameter.

The coarsening of In-rich $Al_xIn_{1-x}N$ particles can be demonstrated by electron microscopy. Figure 5.9 indicates the STEM-HAADF and high resolution TEM (HRTEM) cross section images of $Al_{0.87}In_{0.13}N$:Tm layers, which were annealed at 700 °C for 20 and 90 minutes. Although the In-rich particles are clearly observable by the use of STEM-HAADF (figure 5.9 (a) and (c)), resolution of this microscope is unfortunately insufficient to precisely determine the particle size. And due to instability of the layers against long exposure time and too large inner shell ionization energy of Al and In, other TEM combined analytical techniques, such as EDS and EELS mapping, are not applicable. Hence the particle size can be only determined via graphical measurement on the HRTEM images. As can be senn in figure 5.9 (b) and (d), after 20 minutes annealing it is ca. 2.0 nm and after 90 minutes 3.5 nm.

Nevertheless, we confirm according to our calculated and microscopic results that, the decomposed In-rich $Al_xIn_{1-x}N$ particles with initial mean size of 1 nm (calculated in section

5.1.2) coarsen as the thermal annealing proceeds. Furthermore we set the averaged particle diameters, which are graphically measured from the HRTEM images, as d^* and plot the corresponding mean values $\bar{d}$ against annealing duration (see figure 5.10). Through fitting with equation 5.14, the constant τ of $Al_{0.87}In_{0.13}N$:Tm system annealed at 700 °C is 3.15 ± 1.61 min. Thus, we can use this result to predict the size of In-rich particles after any annealing duration and based on this to estimate their band gap energy as discussed in next chapter.

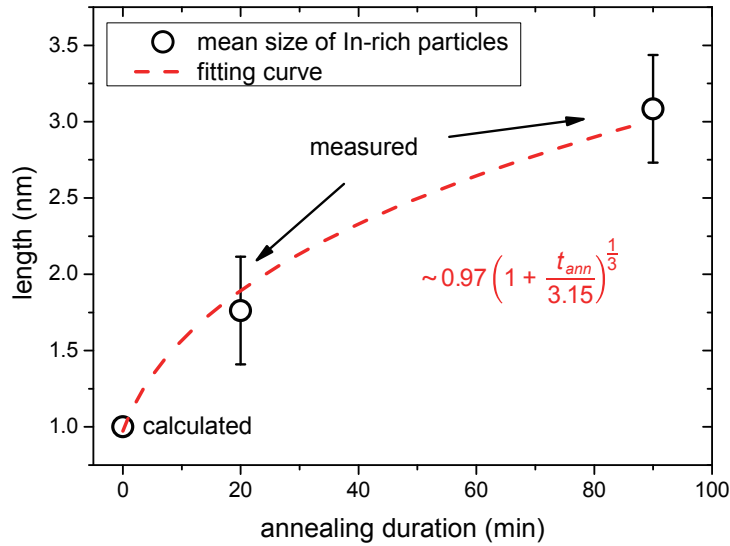
Figure 5.10: Plot of mean particle diameter of $Al_{0.87}In_{0.13}N$:Tm layers against annealing duration at 700 °C. The value for 0 minutes is calculated at the end of section 5.1.2 and the values for 20 and 90 minutes are calculated on the base of HRTEM investigations as shown in figure 5.9 (b) and (d).

5.2 Interaction between In-rich $Al_xIn_{1-x}N$ particles and lanthanide luminescence centres

In addition to epitaxial surface nanofaceting, e.g. Stranski-Krastanow and Volmer-Weber growth, the decomposition has been experimentally confirmed as another way to produce self-organized semiconductor quantum dots (QDs). And it is in particular applied in ternary and even quaternary III-V semiconductors with large miscibility gap, such as InGaN [165] and InGa(Al)As [166]. As theoretically and experimentally investigated in the previous chapter, under appropriate thermal treatment the spinodal decomposition of $Al_xIn_{1-x}N$ system with selected composition will generate an almost instantaneous formation of In-rich $Al_xIn_{1-x}N$ nanoparticles. They have a smaller band gap than their surrounding Al-rich phases and thus correspond electronically to quantum dots (QDs). The subsequent slower coarsening follows Ostwald ripening process and results in a relative narrow particle size distribution. This inspires us to engineer the band gap energy of In-rich $Al_xIn_{1-x}N$ QDs through annealing duration controlled size modification. We suggest in section 5.2.1 that these dots could be efficient energy transmitters for excitation of the lanthanide luminescence centres, once their band gap energy is in resonance with the levels to be excited in lanthanide ions. Section 5.2.2 focuses on establishing a model to describe this resonant excitation process. Our experimental results about the development of PL intensity of $Al_{0.87}In_{0.13}N$:Tm and $Al_{0.84}In_{0.16}N$:Pr, after different annealing duration indicates a good agreement with this model (discussed in section 5.2.3 and 5.2.4).

5.2.1 In-rich $Al_xIn_{1-x}N$ particles as quantum dots for lanthanide excitation

Quantum confinement effect, which arises from the restriction of charge carriers by low dimensional semiconductor nanostructure, was discovered in early 1980s [167, 168]. After that it was frequently used to achieve novel optoelectronic applications (cf. section 1.1). Quantum confinement in zero-dimensional semiconductors, as known as quantum dots (QDs), gives rise to discrete carrier states and expansion of their band gap energy. According to "particle in box model" this expanded band gap E_g^{QD} is dependent on the dot diameter d [169]:

$$E_g^{QD} = E_g^{Bulk} + \Delta E_g = E_g^{Bulk} + \frac{3}{2}\left(\frac{n\hbar\pi}{d}\right)^2\left(\frac{1}{m_{ne}^*} + \frac{1}{m_{nh}^*}\right), \quad (5.16)$$

where E_g^{Bulk} represents the band gap energy of the corresponding bulk semiconductor, ΔE_g the band gap increment due to quantum confinement, n the quantum number, $\hbar$ the Dirac constant, m_{ne}^* and m_{nh}^* the effective mass of electrons and holes respectively. The effective mass of heavy holes m_{1hh}^* is commonly used for the calculation (heavy-hole type of QDs, m_{1e}^*-m_{1hh}^*), because the quantum confinement raises the energy position of valence band degeneration and thus shift the heavy hole states above the light hole states. A recent report [170] suggested on the other hand that the elastic stress may further modify
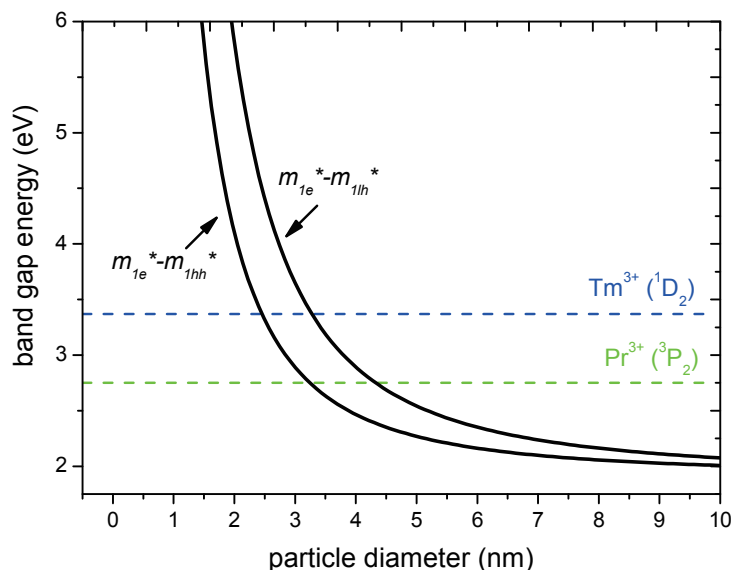
Figure 5.11: Extended band gap extension E_g^{QD} of $Al_{0.08}In_{0.92}N$ particle due to quantum confinement. Both types of QDs, heavy-hole and light-hole, are considered for the calculation. Dashed lines indicate the selective $4f$ energy levels of Tm^{3+} ($^1D_2$) and Pr^{3+} ($^3P_2$) relative to their corresponding ground states, which can be resonantly excited by QDs (see section 5.2.2, 5.2.3 and 5.2.4).

the band structure, which favours the formation of light-hole exciton in QDs (light-hole type of QDs, m_{1e}^*-m_{1lh}^*). Since elastic internal stress in annealed $Al_xIn_{1-x}N$ layers with the magnitude of several hundred MPa is confirmed by XRD investigations (see table B.3 in appendix B), it may be necessary to survey both cases in the determination of extended band gap energy[6].

The inverse dependence of the extended band gap energy of $Al_{0.08}In_{0.92}N$ on the second power of particle diameter is clearly illustrated in figure 5.11[7]. The AlN content corresponds to the In-rich phase after spinodal decomposition estimated by EDS line scan (figure 5.2 (b)). It can be seen that the quantum confinement effect becomes significant, if the size of nanoparticles falls short of 6 nm.

According to the results shown in figure 5.9, the diameter of In-rich nanoparticles is about 2 nm after 20 minutes annealing and 3.5 nm after 90 minutes. Hence a strong quantum confinement effect can be expected. In the room temperature PL spectra of annealed $Al_xIn_{1-x}N$ layers without lanthanide doping, however, no light emission from QDs can be observed. This is very likely related to the strong sensitivity of radiative carrier recombination in quantum dots against structure defects, such as stacking faults and grain boundaries. They serve as non-radiative recombination centres [176, 177] and are unavoidable during the layer preparation. Moreover, due to high density of nanoparticles the inter-dot

---

[6] As will be discussed in section 5.2.3, the heavy-hole type is still the dominant one in present In-rich $Al_xIn_{1-x}N$ QDs.

[7] In order to obtain both curves in this figure, value of E_g^{Bulk} is calculated by using the relationship between band gap energy of polycrystalline $Al_xIn_{1-x}N$ and AlN content determined by P. Gehring ($E_g^{Bulk} = 5.78x_{AlN} + 1.89(1-x_{AlN}) - 3.99x_{AlN}(1-x_{AlN})$) [171]. The effective masses of charge carriers for $Al_xIn_{1-x}N$ are assumed to be $m_{Al_xIn_{1-x}N}^* = x_{AlN} \cdot m_{AlN}^* + (1-x_{AlN}) \cdot m_{InN}^*$. Values of m_{AlN}^* and m_{InN}^* are taken from the references [172, 173, 174, 175].

carrier transfer, which includes temperature induced transfer [178], Auger carrier-carrier scattering [179] and Phonon-assisted tunnelling [180], must not be neglected. The corresponding characteristic time (several tens of ps) is substantially shorter in compare with the lifetime of radiative recombination in QDs ($\sim$ 1 ns). Hence the measured rise time of QD luminescence decreases with increasing dot density [181]. Such processes widen the spatial transfer region of excited carriers and thus enhance their probability to be recombined within non-radiative centres.

Fortunately, we may suppress those negative effects by doping with lanthanide ions, and take the advantage of high density of carriers confined in QDs to excite lanthanide luminescence centres. Size of the In-rich $Al_xIn_{1-x}N$ QDs and therefore their band gap energy are well tunable through reliable thermal treatment. If a lanthanide ion exists on the vicinity or inside of suitable QDs, whose band gap energy matches the energy difference between $4f$ ground state and a $4f$ excited state of lanthanide, resonant excitation of this lanthanide ion could occur. In figure 5.11, required energy to excite $^1D_2$ level of Tm^{3+} and $^3P_2$ level of Pr^{3+} are compared with the band gap energy of QDs.

We believe that the mechanism of the Förster resonance energy transfer (FRET) is dominant in this non-radiative energy transfer process, in which the transfer rate k_{FRET} between energy donor and acceptor depends on their spatial distance r [124, 182]:

$$k_{FRET} = k_D \cdot \left(\frac{R_0}{r} \right)^n. \tag{5.17}$$

Here represents k_D the donor deactivation rate in the absence of acceptor, exponent n describes the mode of energy transfer and e.g. equals $n = 6$ for dipole-dipole transfer. R_0 is Förster distance at which the energy transfer rate equals k_D. It depends on spectra overlap of donator and acceptor, $J_{overlap}$, and a constant, C_{FRET}, which consists of the refractive index, the quantum yield of donor and the orientation factor of FRET:

$$R_0 = \sqrt[n]{C_{FRET} \cdot J_{overlap}}. \tag{5.18}$$

It can be concluded from equations 5.17 and 5.18 that the energy transfer rate between In-rich $Al_xIn_{1-x}N$ QDs with adequate size and lanthanide luminescence centres becomes infinite fast, if lanthanide ions are placed inside or very close to the dots ($r \to 0$). Therefore, the expeditious energy transfer from excited QDs will enhance the lanthanide luminescence significantly. In the following sections we develop a mathematical model to describe this kind of resonant excitation (section 5.2.2) and compare it with our experimental results (section 5.2.3 and 5.2.4).

5.2.2   Model of resonant lanthanide luminescence centre excitation via quantum dots

General model description

In order to model the enhancement of lanthanide luminescence through resonant excitation of In-rich $Al_xIn_{1-x}N$ QDs, all of the possible energy path ways must be primarily clarified. As can be seen in figure 5.12 (a), there are generally three path ways to relax the excitation energy:
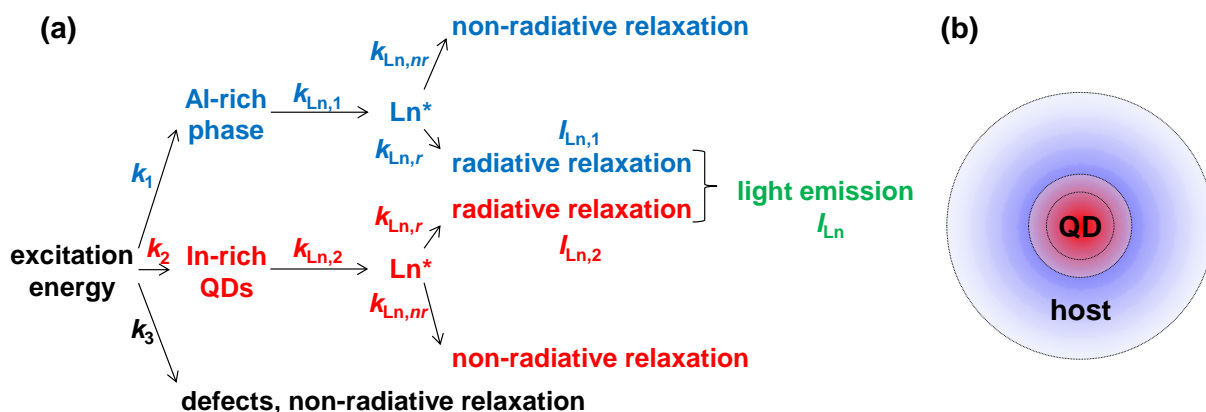
Figure 5.12: (a). Excitation and relaxation paths of lanthanide luminescence centres doped in QDs containing semiconductor host. Details for paths and coefficients are described in the text. (b). Illustration on the assumption of "uniqueness of excitation path".

- *Path 1: Excitation of lanthanide luminescence centres via Al-rich phase*
  Excited free carriers are trapped by the acceptor and/or donator-like defect levels or the lanthanide ion associated energy levels between the band gap of the host with a rate coefficient k_1, Through subsequent energy transfer with rate coefficient $k_{Ln,1}$, lanthanide luminescence centres are excited. The electronic processes within this path is basically in a similar way to the energy path 1 in AlN:Ln system discussed in section 4.3.2.

- *Path 2: Excitation of lanthanide luminescence centres via In-rich QDs*
  Excited free carriers are firstly captured by the In-rich $Al_xIn_{1-x}N$ QDs with a rate coefficient k_2. And then they transfer their residual energy non-radiatively to lanthanide luminescence centres within and close to QDs. We propose the rate coefficient of this energy transfer is determined by Föster mechanism, namely $k_{Ln,\,2} = k_{FRET}$ (cf. equation 5.17 and 5.18).

- *Path 3: Other excitation and relaxation processes without energy transfer into lanthanide centre*
  Consistent with the energy path 2 in AlN:Ln system (section 4.3.2), carriers in this path way are excited and recombine with each other by other possible processes with rate coefficient k_3. Energy released thereby is not absorbed by lanthanide luminescence centres.

Before establish a mathematic model on resonant excitation of lanthanide luminescence centres in In-rich QDs contained $Al_xIn_{1-x}N$ system and its changes during thermal annealing, we must emphasise three important presumptions to simplify the considerations:

1. *Uniqueness of excitation path*
   The model discussed in the following parts of this section is based on the presumptions that the excitation paths of lanthanide luminescence centres through Al-rich phase (path 1, blue region in figure 5.12 (b)) and In-rich QDs (path 2, red region in figure 5.12 (b)) are independent on each other. And a given lanthanide centre can be excited only by one of those two paths.

2. *Independent relaxation of lanthanide luminescence centres*
   Radiative and non-radiative relaxations of a lanthanide luminescence centre are independent on whether it was excited via Al-rich phase or In-rich QDs. The radiative relaxation rate $k_{Ln,r}$ is identical in both cases and so is the non-radiative relaxation rate $k_{Ln,nr}$.

3. *Adoption of the concept "extended lanthanide luminescence centre"*
   According to spectral analysis and discussions on AlN:Ln systems (chapter 4), it is reasonable to believe that in $Al_xIn_{1-x}N$:Ln system the number of lanthanide luminescence centres excited through path 1 and 2 ($N_{LLC,1}$ and $N_{LLC,2}$) as well as excitation and relaxation rate coefficients (k_1, $k_{Ln,1}$, k_2, $k_{Ln,2}$, $k_{Ln,r}$ and $k_{Ln,nr}$) changes during the thermal annealing. In order to reduce these variable parameters we can also adopt the concept of "extended lanthanide luminescence centres" (cf. section 4.3.2) for the present case. Instrumental parameters, including exposure time (t_m) and luminescence peak width (ΔE), are set as constants.

Path 1: excitation through Al-rich phase

Due to instantaneous decomposition the composition of Al-rich phase approaches a constant value at the very beginning of thermal annealing (figure 5.4). And based on the results in AlN:Ln (figure 4.2), we speculate that the local atomic rearrangements in $Al_xIn_{1-x}N$ should be accomplished after the first few minutes of annealing as well. Further annealing will not give rise to considerable changes in the number of the extended lanthanide luminescence centres (N_{ELLC}). Hence the resulted luminescence intensity tends to an asymptotical saturation value (see blue dashed curve in figure 5.14) with a mathematical expression analogue to equation 4.4 and 4.9:

$$I_{Ln,1} \approx \frac{k_1}{k_1 + k_2 + k_3} \cdot \frac{k_{Ln,1}k_{Ln,r}}{k_{Ln,r} + k_{Ln,nr}} \cdot N_{LLC,1} \cdot C_{exp} = A_1 + B_1\big[1 - \exp(-k_{f,1} \cdot t_{ann})\big], \quad (5.19)$$

where $A_1 = N_{ELLC,1}^i \cdot C_{exp}$ and $B_1 = \Delta N_{ELLC,1}(\infty) \cdot C_{exp} \cdot \exp(-E_{f,1}/kT)$ are constants at given annealing temperature, $E_{f,1}$ and $k_{f,1}$ the generalised formation energy and formation rate of ELLC in Al-rich phase.

Path 2: excitation through In-rich QDs

If the lanthanide ions are homogenously distributed in $Al_xIn_{1-x}N$ host and their doping concentration is very low, one may expect that no considerable segregation of lanthanide dopants will take place during thermal annealing. So the average distance between QDs and lanthanide ions $\langle r \rangle$ remains invariant. The energy transfer rate coefficient $k_{Ln,2}$ is thus only determined by the spectra overlap between them $J_{overlap}$. And this overlap is proportional to the portion of In-rich QDs, $f_{d_{res}}(t_{ann})$, whose band gap energy matches the energy required to directly excite selected $4f$-level of lanthanide luminescence centres
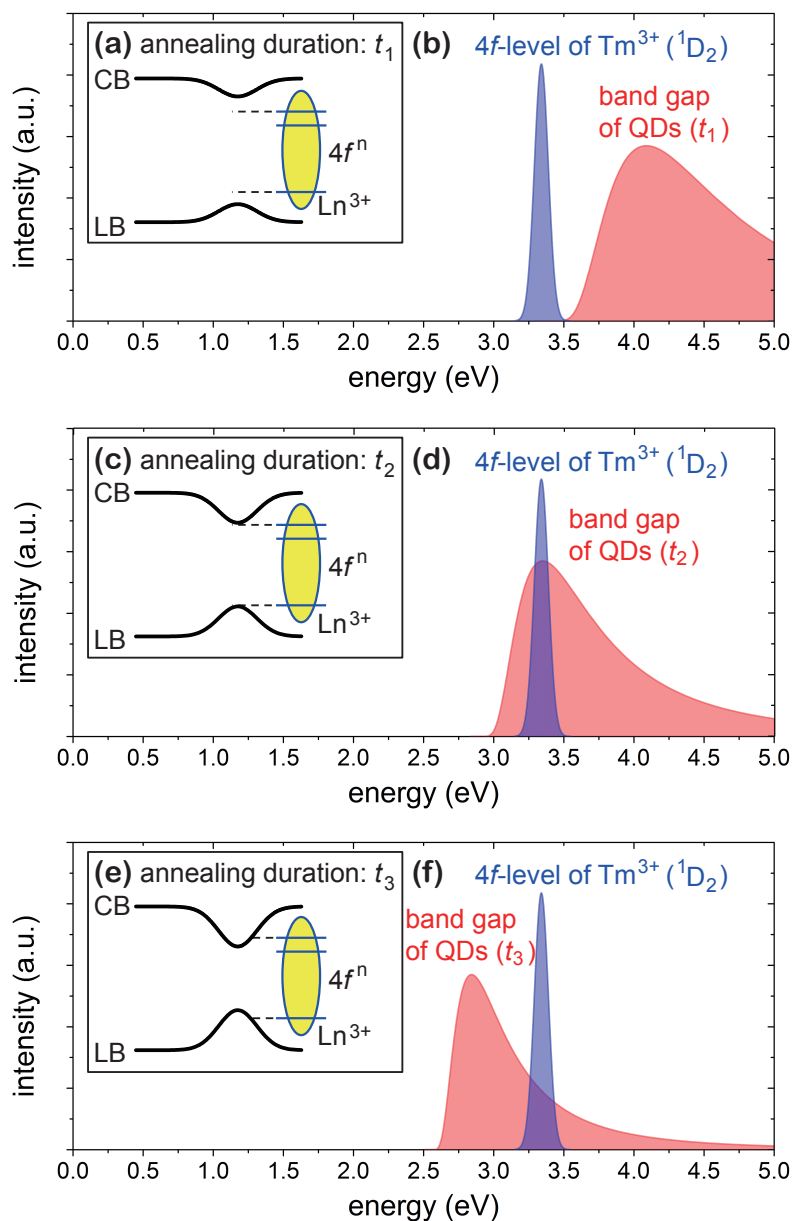
Figure 5.13: Schematic illustration of the band gap energy modification of In-rich QDs after different annealing duration (a) t_1, (c) t_2 and (e) t_3 ($t_1 < t_2 < t_3$), and their spectral overlap with the $^1D_2$ level of Tm ions (corresponds the overlapping part of two curves in (b), (d) and (f)). The spectra of the lanthanide ions are thereby assumed by a Gaussian approximation and the band gap energy of QDs is calculated by using equations 5.15 and 5.16.

(cf. equations 5.17 and 5.18):

$$J_{overlap} = C_{overlap} \cdot f_{d_{res}}(t_{ann}).$$ (5.20)

$C_{overlap}$ is a proportionality constant and d_{res} the size of the QDs appropriate for resonant excitation. The mathematical expression of $f_{d_{res}}(t_{ann})$ is given by equation 5.15 by setting $d = d_{res}$ Therefore one receives for $k_{Ln,2}$:

$$k_{Ln,2} = k_{FRET} = C_{Ln,2} \cdot f_{d_{res}}(t_{ann}),$$ (5.21)

where $C_{Ln,2} = k_D \cdot C_{FRET} \cdot C_{overlap} \cdot (1/\langle r \rangle)^n$ is a constant.

As discussed in section 5.1.3 and 5.2.1, the coarsening of In-rich nanoparticles leads to the reduction of their band gap energy in accordance with equation 5.16. One can confirm from the graphical demonstration of this tendency as shown in figure 5.13 that with thermal annealing, $J_{overlap}$, and therefore $k_{Ln,2}$, will firstly rise to a maximum value and then decrease to zero. Hence we may conclude that the luminescence intensity of lanthanide excited via In-rich QDs is predominantly determined by $k_{Ln,2}$. And appropriate modifications on the concept of "extended lanthanide luminescence centres" should be made:

$$
\begin{aligned}
I_{Ln,2} &\approx k_{Ln,2} \cdot \frac{k_2}{k_1 + k_2 + k_3} \cdot \frac{k_{Ln,r}}{k_{Ln,r} + k_{Ln,nr}} \cdot N_{LLC,2} \cdot C_{exp} \\
&= f_{d_{res}}(t_{ann}) \cdot \left\{ A_2 + B_2 \left[1 - \exp(-k'_{f,2} \cdot t_{ann}) \right] \right\},
\end{aligned}
$$ (5.22)

In equation 5.22 we place the key factor $f_{d_{res}}(t_{ann})$ in front of the product and the term within curly bracket represents the evolution of the extended lanthanide luminescence centres, in which only the capture of excited carriers by QDs and radiative relaxation of excited lanthanide centres are taken into account. At given annealing temperature the parameters $A_2 = C_{Ln,2} \cdot N^i_{ELLC,2} \cdot C_{exp} \cdot C_{s.d.}$ and $B_2 = C_{Ln,2} \cdot \Delta N_{ELLC,2}(\infty) \cdot C_{exp} \cdot \exp(-E'_{f,2}/kT) \cdot C_{s.d.}$ are invariant. Meanings of the thermodynamic and kinetic parameters, $E'_{f,2}$ and $k'_{f,2}$, as well as the numbers of extended luminescence centres $N^i_{ELLC,2}$ are different from those in excitation path 1. The red dashed line in figure 5.14 predicts the variation of $I_{Ln,2}$ during thermal annealing.

Total intensity of lanthanide luminescence (path 1 and 2)

According to the presumptions 1 and 2 mentioned in the first part of this section, measured lanthanide luminescence intensity I_{Ln} is a summation of intensity generated through Al-rich phase (path 1) and In-rich QDs (path 2):

$$
I_{Ln} = I_{Ln,1} + I_{Ln,2} = A_1 + B_1[1 - \exp(-k_{f,1} \cdot t_{ann})] + A_2 + B_2[1 - \exp(-k'_{f,2} \cdot t_{ann})] \cdot
$$

$$
\left\{ \frac{1}{\left(1 + \frac{t_{ann}}{\tau}\right)^{\frac{4}{3}}} \left[\frac{d_{res}}{\bar{d}(0)\left(1 + \frac{t_{ann}}{\tau}\right)^{\frac{1}{3}}} \right]^2 \left[\frac{3}{3 + \frac{d_{res}}{\bar{d}(0)(1+\frac{t_{ann}}{\tau})^{\frac{1}{3}}}} \right]^{\frac{7}{3}} \left[\frac{\frac{3}{2}}{\frac{3}{2} - \frac{d_{res}}{\bar{d}(0)(1+\frac{t_{ann}}{\tau})^{\frac{1}{3}}}} \right]^{\frac{11}{3}} \cdot \right.
$$

$$
\left. \exp\left[-\frac{\frac{d_{res}}{\bar{d}(0)(1+\frac{t_{ann}}{\tau})^{\frac{1}{3}}}}{\frac{3}{2} - \frac{d_{res}}{\bar{d}(0)(1+\frac{t_{ann}}{\tau})^{\frac{1}{3}}}} \right] \right\}.
$$

$$(5.23)$$

During the annealing the total intensity of lanthanide luminescence will increase to a maximum and the decreases to a finite value (black solid line in figure 5.14). Through elaborate analysis on the formation of extended lanthanide luminescence centres, spinodal decomposition, energy excitation, transfer and relaxation processes, we can simplify the tedious equation 5.23 by reducing the parameters for some special cases. For example, if $k'_{f,2}$ value is sufficient large, the number of extend lanthanide luminescence centres within In-rich QDs reaches its equilibrium before the size of QDs satisfies the resonant condition. In this way the term $A_2 + B_2[1 - \exp(-k'_{f,2} \cdot t_{ann})]$ can be regarded as a constant. In previous sections we have theoretically and experimentally determined the values of $\bar{d}(0)$, d_{res} and τ for system $Al_{0.87}In_{0.13}N$:Tm. We may further assume with less impreciseness that the generalised formation energy and formation rate of extended
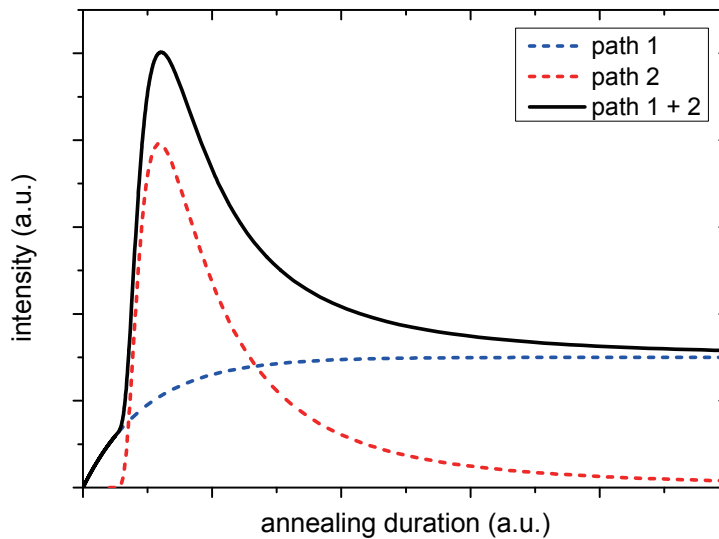

Figure 5.14: Development of lanthanide luminescence intensity excited by Al-rich phases (blue dashed line), In-rich QDs (red dashed line) and its total intensity (black solid line) during thermal annealing predicted by the model described in the text.

lanthanide luminescence centres are approximately invariant in path 1 and 2 ($E_{f,1} \approx E'_{f,2}$, $k_{f,1} \approx k'_{f,2}$). Comparisons between this model and PL results as well as the relating discussions are delineated in the next sections.

5.2.3 Luminescence enhancement of $Al_{0.87}In_{0.13}N$:Tm

As an important result we find a significant intensity enhancement of the blue luminescence emitted from Tm doped $Al_{0.87}In_{0.13}N$ layers (corresponds to $^1D_2$ - $^3F_4$ and $^1G_4$ - $^3H_6$ transitions of Tm ion) after about 30 minutes annealing at 700 °C (see figure 5.15 (a)). In addition to his, the luminescence intensity depends on excitation energy E_{exc}. In figure 5.15 (b), the intensity after different annealing duration is integrated and plotted against E_{exc}. It approaches a maximum if E_{exc} matches to the band gap energy of the Al-rich phase ($E_g = 4.8$ eV, as shown in figure 5.4 (b)).

This phenomenon can be understood with the help of the nature of QDs and the model of bound excitons mediated lanthanide ion excitation [133, 183]: During below band gap excitation ($E_g^{QDs} < E_{exc} < E_g^{Al-rich}$) merely a little portion of excitation photons are absorbed. The In-rich QDs can be directly excited only with much less efficiency due to their small size and volume fraction. In the Al-rich phase, bound excitons are created only if there are appropriate carrier traps presented in the band gap. When a Tm ion exists in their vicinity, it can be excited via non-radiative energy transfer from the bound exciton. The low photon absorption and energy transfer probability lead to the low PL intensity. In above band gap excitations ($E_{exc} \geq E_g^{Al-rich}$), almost all photons are absorbed by the Al-rich phase. The resulting free carriers exhibit a comparatively longer life time. This increases their probability to be trapped by QDs or energy states within the band gap and subsequently transfer the residual energy into the Tm luminescence centres. Our
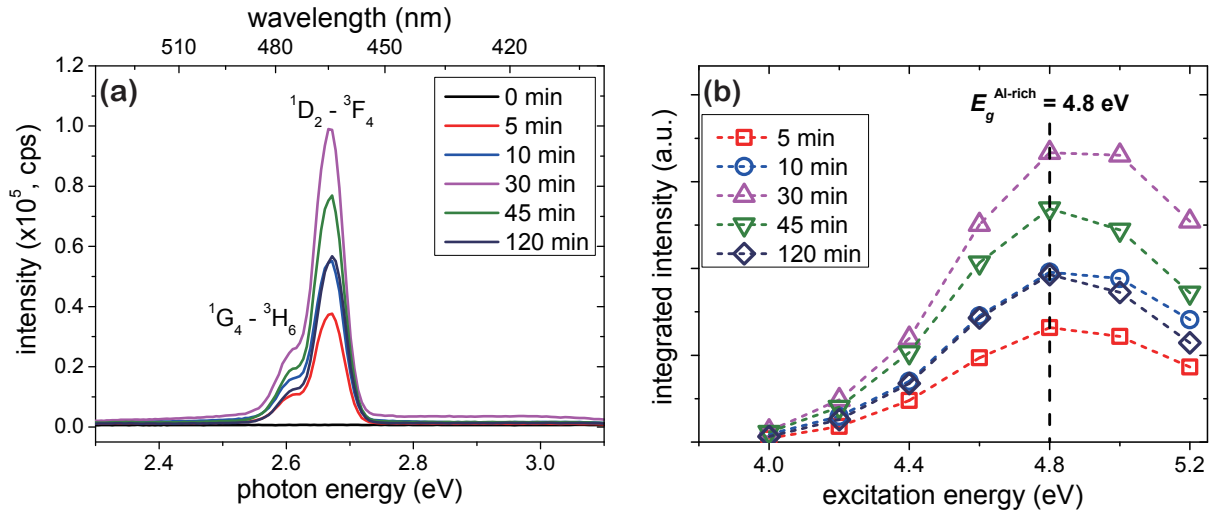
Figure 5.15: (a) PL spectra of $Al_{0.87}In_{0.13}N$ layers after annealing at 700 °C for different durations. Optical energy of 4.8 eV was selected for the excitation. The peaks are labeled with the indicated intra $4f$-transitions. (b) The corresponding integrated intensity is plotted against excitation energy E_{exc}. Maximum intensity is normalised to unity and the bang gap energy of Al-rich host is marked with black dashed line.
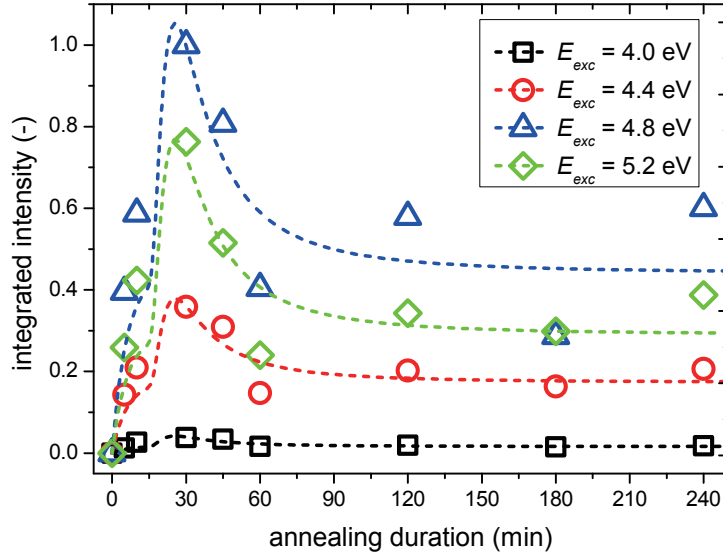
Figure 5.16:   Relationship between integrated blue luminescence intensity of Tm doped in $Al_{0.87}In_{0.13}N$ layers ($^1D_2$ - $^3F_4$ and $^1G_4$ - $^3H_6$) and annealing duration. The layers were annealed at 700 °C and excited by different photon energy E_{exc}. The value of maximal intensity is normed as unity and the dashed lines are the fitting curves by using equation 5.24.

experimental results further indicate that, if the excitation energy is much larger than the band gap energy, luminescence intensity decreases. A similar observation has been also made in SiN systems [184]. The explanation given in this report is based on the model of the demarcation lines under conduction band [185] and might hold also in the present case. Unoccupied energy states above this line capture the carriers from conduction band of the Al-rich phase. And the consecutive carrier thermalisation increases the probability of non-radiative relaxation. A more detailed assessment, however, appears premature since the exact nature of the defects in our samples is unknown.

It can be seen from figure 5.16 that the integrated intensity rises steeply at the beginning of annealing and reaches its maximum at ca. 30 minutes. Subsequently, it drops down and approaches after 60 minutes to a rather stable intensity at about 50 % of its maximal value. This experimental result is in excellent agreement with the outcome anticipated from the model introduced in the previous sections.

Because no Tm luminescence was detected before annealing (black line in figure 5.15 (a)), we set the parameters A_1 and A_2 in equation 5.23 as zero. According to equation 5.12 and the parameter $\tau = 3.15$ min fitted from the data of figure 5.10, the diameter of spherical In-rich particle with maximum number, d^*, equals 2.4 nm after 30 minutes annealing. On the other hand, if the band gap energy of In-rich QDs is in resonance with the energy required to directly excite $^1D_2$ level of Tm centres, their size d_{res} should correspond to 2.5 and 3.3 nm according to the heavy-hole type and light-hole type confinement model, respectively (figure 5.10). Obviously the former one coincides with the result determined by the coarsening kinetics of In-rich particle. Hence it is suggested that the intensified Tm luminescence in $Al_{0.87}In_{0.13}N$ layer is due to the resonant energy transfer from excited In-rich QDs with heavy-hole type. And the elastic internal stress in the layers is not sufficient to shift heavy-hole state under light-hole state. By using $\bar{d}(0) = 1.0$ nm

(calculated in section 5.1.2), $d_{res} = 2.5$ nm and $k_{f,1} = k'_{f,2} = k_f = 0.17/\text{min}$ (comparable to the value of AlN:Tm system annealed at 700 °C, table 4.1) the complex equation 5.23 can be reduced as:

$$I_{\text{Tm}}(t_{ann}) = [1 - \exp(-k_f \cdot t_{ann})] \left\{ B_1 + B_2 \frac{1}{\left(1 + \frac{t_{ann}}{3.15}\right)^{\frac{4}{3}}} \left[\frac{2.5}{\left(1 + \frac{t_{ann}}{3.15}\right)^{\frac{1}{3}}} \right]^2 \left[\frac{3}{3 + \frac{2.5}{(1 + \frac{t_{ann}}{3.15})^{\frac{1}{3}}}} \right]^{\frac{7}{3}} \right. \cdot$$

$$\left. \left[\frac{\frac{3}{2}}{\frac{3}{2} - \frac{2.5}{(1 + \frac{t_{ann}}{3.15})^{\frac{1}{3}}}} \right]^{\frac{11}{3}} \exp \left[-\frac{\frac{2.5}{(1 + \frac{t_{ann}}{3.15})^{\frac{1}{3}}}}{\frac{3}{2} - \frac{2.5}{(1 + \frac{t_{ann}}{3.15})^{\frac{1}{3}}}} \right] \right\} .$$

$$(5.24)$$

The intensity developments of Tm as shown in figure 5.16 are well described by equation 5.24 (dashed lines). Parameters B_1 and B_2 fitted thereby are listed in table 5.1. With different excitation energy there are basically no significant changes on their ratios B_2/B_1. This suggests that the contributions of excitation via Al-rich phase and In-rich QDs on the luminescence intensity depends scarcely on the excitation energy between 4.0 and 5.2 eV.

Table 5.1: Parameter of B_1 and B_2 fiited from the results illustrated in figure 5.16 by using equation 5.24.

E_{exc}	4.0 eV	4.4 eV	4.8 eV	5.2 eV
B_1	0.016	0.173	0.441	0.290
B_2	0.113	0.900	2.685	2.094
B_1/B_2	0.144	0.193	0.164	0.139

5.2.4 Luminescence enhancement of $Al_{0.84}In_{0.16}N$:Pr

The model of resonant excitation of lantahnide luminescence centres via QDs can be further supported by investigations on $Al_xIn_{1-x}N$ layers doped with other lanthanide ions. Similar to $Al_{0.87}In_{0.13}N$:Tm we find in figure 5.17 that the intensity of green luminescence of $Al_{0.84}In_{0.16}N$:Pr layers (corresponds to the transition $^3P_1$ - $^3H_5$ of Pr^{3+}) reaches a maximum after 20 minutes annealing at 700 °C. An optical energy of 4.2 eV was selected for the excitation, which lies below the band gap energy of Al-rich phase. We confirm on the base of discussions in section 5.1.2 that the initial In-rich particles size $\bar{d}(0)$ of about 1 nm also holds for this system, even though the microscopic analyses on its decomposition are lacking. Despite of the $^1S_0$ level, which lies above 6 eV, the second highest $4f$-level of Pr^{3+} is $^3P_2$ with an energy of 2.78 eV related to ground state (see figure C.1 (a)). Hence, In-rich QDs with $d_{res} = 3.2$ nm (heavy-hole type) can be used to excite Pr luminescence centres resonantly.

Because the formation of extended Pr luminescence centres in AlN is very fast (cf. section 4.3.2), we apply equation 5.24 with different formation probabilities of extended luminescence centres to fit the development of Pr luminescence intensity during annealing (namely
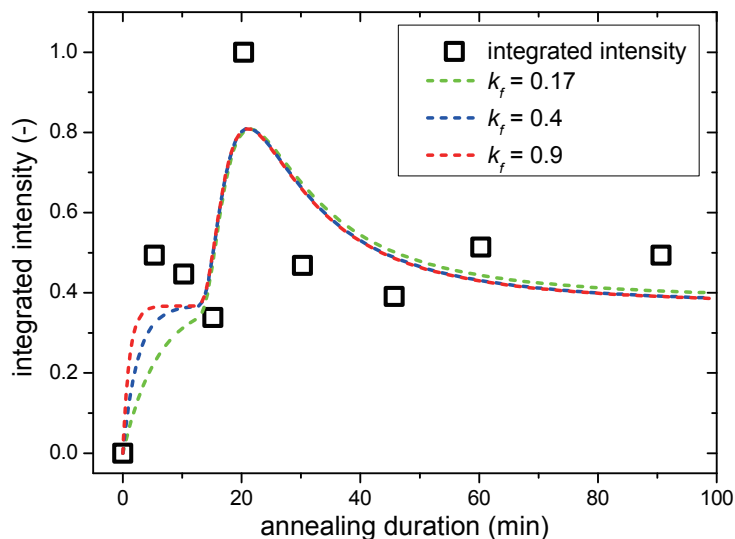
Figure 5.17: Relationship between integrated green luminescence intensity of Pr ($^3P_1$ - $^3H_5$) doped in $Al_{0.84}In_{0.16}N$ layers and annealing duration (recorded from [155]). The layers were annealed at 700 °C and excited by photon energy 4.2 eV. Maximum intensity is normalised as unity, and the dashed lines are the fitting curves by using equation 5.24 with different k_f-values.

$k_f = 0.17$, estimated from AlN:Tm, $k_f = 0.4$ used for AlN:Pr and a much larger value $k_f = 0.9$). Unfortunately, the fitted results are less satisfactory, as can be seen in figure 5.17. This is probably due to the excitation energy is too low to excite Pr centres efficiently, and thus increases the possible error of the measurement. Nevertheless, we find that the fitted parameters, B_1, B_2 and τ, are generally independent of the k_f-values (see table 5.2). This may imply that most of extended Pr luminescence centres are formed before the resonant excitation via QDs takes place[8].

Table 5.2: Parameter of B_1, B_2 and τ fitted from figure 5.17 by using equation 5.24 with different k_f-values.

	B_1	B_2	τ
$k_f = 0.17$	0.381	5.094	1.188
$k_f = 0.4$	0.368	5.003	1.191
$k_f = 0.9$	0.367	5.002	1.188

Before closing this chapter, it is worth noticing that the carrier recombination within QDs without lanthanide doping is very fast (in ns range [186, 187]), whereas the decay time of radiative lanthanide relaxation is in general at least three orders of magnitude longer [121, 122, 123]. So the former case should take precedence over the later one. To the contrast, many studies reported that QDs can be considered as luminescence intensifier not only for lanthanide [138, 188] but also for transition metal ions [137]. And by increasing concentration of the lanthanide dopants luminescence intensity of QDs reduces [140]. According to the temperature dependence of PL intensity from Eu-doped GaN QDs, Y. Hori and his co-workers proposed that the localised carriers in QDs are much easier trapped

---

[8] Actually this is also the case for $Al_{0.87}In_{0.13}N$:Tm system.

by Eu ions than in the case of simply Eu-doped GaN layers. This results more sufficient energy transfer and higher priority of radiative relaxation of luminescence centres [139]. In order to fully understand the physical mechanisms behind the enhancement of lanthanide luminescence by QDs, further elaborate studies are imperative.

5.3   Conclusions

In the first part of this chapter the thermodynamics and kinetics of decomposition in the $Al_xIn_{1-x}N$ system are discussed quantitatively. Based on microscopic analyses using *in-situ* TEM, HRTEM as well as HAADF cross-sectional imaging and EDS compositional scanning in a STEM, we confirm in the studied systems an almost instantaneous formation of nano-sized In-rich $Al_xIn_{1-x}N$ particles with subsequent comparatively slow coarsening. Combining the results of mathematical calculations and microscopic investigations, the development of In-rich particle size distributions in $Al_{0.87}In_{0.13}N$:Tm during thermal annealing at 700 °C is reliably estimated.

The slow coarsening of the In-rich particles permits us in the second part of this chapter to engineer their sizes and thereby their band gap energy (according to size-dependent quantum confinement effect) by alteration of annealing temperature and duration. If this energy overlaps with an excited $4f$-level of lanthanide luminescence centres, a resonant energy transfer between them may take place. We develop a quantitative model, which is based on time-dependent coarsening of In-rich particles at the selected temperature and the corresponding decrease of the band gap energy, spectral overlapping between In-rich particles and lanthanide luminescence centres as well as the thermal activation of extended lanthanide luminescence centres, to describe the corresponding resonant excitation and predict the resulting luminescence intensity. The model is in good agreement with our PL data, which indicate significant intensity enhancements of the blue luminescence from $Al_{0.87}In_{0.13}N$:Tm ($^1D_2$ - $^3F_4$ and $^1G_4$ - $^3H_6$) and the green luminescence from $Al_{0.84}In_{0.16}N$:Pr ($^3P_1$ - $^3H_5$) after annealing at 700 °C for about half an hour.

Chapter 6

Concluding remarks and outlooks

Conclusions

The present work focuses on the optoelectronic properties of III-nitride semiconductors doped with lanthanide ions, mainly AlN:Pr, AlN:Sm, AlN:Tb and AlN:Tm as well as $Al_xIn_{1-x}N$:Tm and $Al_xIn_{1-x}N$:Pr systems with selected AlN contents and relative low doping concentration. Reactive magnetron co-sputtering was employed for the sample preparation. Through elaborate approaches on the base of experimental analysis and theoretical modelling, five central themes were addressed: (1) local symmetry of radiative Sm^{3+} and Tb^{3+} in AlN host; (2) luminescence generated by O-associated defect states in AlN, O_N^- $(V_{Al}-2O_N)^-$ pairs, and its assistance in the excitation of lanthanide luminescence centres; (3) thermal enhancement of lanthanide luminescence intensity in AlN and its modelling; (4) thermodynamics and kinetics of decomposition in $Al_xIn_{1-x}N$ system at adequate annealing temperature; and (5) resonant excitation of Tm and Pr luminescence centres via In-rich $Al_xIn_{1-x}N$ QDs and its modelling.

By summarising these results we may seek for some general strategies to obtain and enhance the visible light emission from lanthanide based phosphors:

- *Selection of host material for lanthanide doping according to crystal field theory*
  As introduced in chapter 3, a prerequisite for intra-$4f$ electron transitions is that the lanthanide ions are located on the site with a non-centrosymmetric point group. This is therefore the most fundamental condition to be fulfilled by choosing host material. In addition, luminescence spectral analysis based on crystal field (CF) theory is the only way to determine the local symmetry of radiative lanthanide ions. In this work, Stark level positions of the lowest four $4f$-multiplets in AlN:Sm (^6H_J, with $J = 5/2, 7/2, 9/2, 11/2$) and three in AlN:Tb system (^7F_J, with $J = 6, 5, 4$) were determined from the peak splitting of their low temperature PL spectra. To our knowledge, it is the first detailed CF analysis for these ions doped in polycrystalline AlN. The results revealed that the most of radiative Sm and Tb ions are placed in C_{3v}-symmetric environment. By computer-assisted fitting of the spectral splitting of the AlN:Sm system we quantitatively obtained the local structural and physical information of the radiative Sm ions. The results, $R_{Sm-N1} = 0.230$ nm, $R_{Sm-N2} = 0.245$ nm, $\theta_{N1-Sm-N2} = 105.10°$ and $Z_{Sm} = 2.5$, are in good agreement with the results

of *ab-initio* calculation presented elsewhere.

- *Thermal activation of lanthanide luminescence centres*
  The layers used for CF analysis were annealed at 1000 ℃ for 30 minutes, because thermal treatment at an appropriate temperature is a convenient method to activate the lanthanide luminescence centres and therefore enhance the luminescence intensity. Structural rearrangement promoted thereby favours the reduction of crystal disorder and the formation of unintentional defect complexes, which, in term, regulate the rate coefficients of electronic processes consisting of host material excitation, energy transfer to lanthanide centres and their radiative and non-radiative relaxation.
  We have observed in chapter 4 that the visible luminescence from AlN:Pr ($^3P_1$ - $^3H_5$ and $^3P_0$ - $^3H_5$), AlN:Sm ($^4G_{5/2}$ - ^6H_J with $J = 5/2, 7/2, 9/2$), AlN:Tb ($^5D_4$ - ^7F_J with $J = 6, 5, 4, 3$) and AlN:Tm ($^1D_2$ - $^3F_4$ and $^1G_4$ - $^3H_6$) can be significantly intensified, if the annealing temperature lies above 700 ℃. Their isothermal evolutions further indicate that the intensity increases rapidly at the very beginning of annealing and then approaches a stable saturation level. Instead tedious characterisation of the dependency of each rate coefficient on annealing temperature, we considered all the sub-processes related change of the lanthanide luminescence as a whole issue and introduced a concept of "extended lanthanide luminescence centre". Thermal activation of these centres is equivalent to a joint reaction of first order. As a result, the intensity enhancement can be successfully described and predicted with only two generalised parameters, formation energy and formation rate of extended lanthanide luminescence centres, E_f and k_f. Through graphic fitting of experimental results we deduced that E_f is about 0.73 eV in AlN:Pr, 0.39 eV in AlN:Sm, 0.99 eV in AlN:Tb and 0.35 eV in AlN:Tm. Values of formation rate, k_f, in AlN:Sm and AlN:Tb system are larger than that in AlN:Tm, because the Sm and Tb luminescence centres are strongly correlated with the rapid formation of O-associated defect pairs (as delineated in the next issue).

- *Use of the existing defect states within the band gap of the host material to expand the excitation range of lanthanide luminescence centres*
  It is generally believed that the low quantum efficiency of a lanthanide doped semiconductor lighting source is mainly due to their narrow excitation spectra and the loss of excitation energy via defect states within the band gap. According to our PL measurements, however, we believed in this work that the rational use of these energy states is an efficient way to enhance the lanthanide luminescence.
  In AlN, unintentional O impurities are unavoidable. The resulting defect luminescence centred at around 2.8 eV can be easily generated by optical excitation of 4.5 eV. Through careful comparisons with literature data, this luminescence can be characterised as the result of radiative recombination of donator-acceptor-pairs constituted by O-associated defect complexes, O_N^--$(V_{Al}$-$2O_N)^-$. The energy stored therein overlaps with the energy required to directly excite the $^1P_2$-level of Pr^{3+}, ^4I_J-levels of Sm^{3+} ($J = 7/2, 11/2, 13/2$), $^5D_4$-level of Tb^{3+} and $^1G_4$-level of Tm^{3+}. As experimentally confirmed (section 4.2), energy transfer from the defect pairs en-

larges the excitation range of lanthanide luminescence centres. Moreover, proper thermal treatments between 300 °C and 600 °C strongly promote the formation of this defect states within the band gap of AlN host, which leads to a correlated enhancement of defect luminescence and selected lanthanide luminescence. As an exceptional case, blue luminescence arising from $^1D_2$ - $^3F_4$ transition in Tm centres shows no correlation effect. This is due to the fact that the energy position of $^1D_2$ level is too high to be sufficiently excited by O_N^--$(V_{Al}$-$2O_N)^-$ pairs.

- *Engineering of host material band structure to resonantly excite lanthanide luminescence centres*

  With the inspiration of lanthanide luminescence enhancement via defect states we have attempted in chapter 5 to appropriately modify the band structure of semiconductor host to improve luminescence. $Al_xIn_{1-x}N$ was chosen as host material because of the wide miscibility gap of its both nitride components, namely AlN and InN. Different techniques of electron microscopy were combined with theoretical investigations including the "Delta Lattice Parameter (DLP) Model", the "Valence Force Field (VFF) model" and the "Cahn-Hilliard gradient theory" to analyse the decomposition in polycrystalline $Al_xIn_{1-x}N$ layers during the annealing at about 700 °C.

  In $Al_{0.87}In_{0.13}N$:Tm layers we found an almost instantaneous formation of nano-sized In-rich precipitation with subsequent comparative slower coarsening according to the volume diffusion controlled Ostwald ripening. These nanoparticles have a smaller band gap than the surrounding Al-rich matrix. And their sizes are small enough (2.0 nm after 20 minutes annealing and 3.5 nm after 90 minutes) that they can be electronically considered as quantum dots (see section 5.1.3 and 5.2.1). The slower coarsening permits us to engineer the size of these QDs and thus their band gap energy to fit the resonance condition with the $4f$-level to be excited in lanthanide luminescence centres. We have further established a preliminary model based on the concept of extended lanthanide luminescence centres, size-dependent band gap altering of QDs and spectra overlap between QDs and lanthanide luminescence centres to demonstrate this resonant excitation and the potential enhancement of luminescence intensity. Significant intensity enhancement of $Al_{0.87}In_{0.13}N$:Tm ($^1D_2$ - $^3F_4$ and $^1G_4$ - $^3H_6$) and $Al_{0.84}In_{0.16}N$:Pr ($^3P_1$ - $^3H_5$) layers after annealing at 700 °C for 20 - 30 minutes can be well quantitatively described by this model.

Outlooks

The study in the scope of present work may be seen as cornerstones for future researches, which are concerned with luminescence enhancement of lanthanide based phosphors. Although the *ab-initio* calculations of the intra-$4f$ transition strength by using odd CF parameters is not able to precisely predict the corresponding luminescence intensity, they may still play an advisory role in the material engineering. As briefly introduced in chapter 3, all the "meaningless" CF parameters are related to some "real" parameters with explicit physical properties, including effective charge and spatial coordinates. Once the relationships between them are well understood, both qualitatively and quantitatively,

one can use them as a guidance to develop the most suitable host material.

Despite of Ce^{3+} and Yb^{3+}, plenty of possible alternative $4f$-levels exist in the other ten non-radioactive lanthanide ions. This means that more than one radiative transition may be activated after excitation. And it seems that the most preferred one (corresponds to the radiative transition with the highest intensity) also depends on the host material. For example, we observed in this work that the green luminescence stemming from $^3P_1$ - $^3H_5$ of Pr^{3+} is dominant in both AlN and $Al_xIn_{1-x}N$, whereas GaN:Pr was found as a convenient red emitter (corresponds $^3P_0$ - $^3F_2$) in the literatures [189, 190]. On this basis, we may rise the interesting question, whether and how the lanthanide luminescence spectra can be adjusted via engineering the CF perturbation. To achieve this, not only the electric dipole transitions but also electric quadrupole transitions, hypersensitive pseudoquadrupole transitions [191] and magnetic dipole transitions should be taken into account.

Another important aspect of the enhancement of lanthanide luminescence intensity by selecting a suitable host material is to sufficiently reinforce the excitation and suppress the non-radiative relaxation processes. Thermally activated ordering of host materials, assistances in the lanthanide excitation through O-associated defect states in AlN and In-rich QDs in $Al_xIn_{1-x}N$ as discussed in this work as well as up-conversion excitation in the lanthanide co-doped materials as reported in the literature [192] are successful approaches, but only valid in specific systems. Therefore, detailed and comprehensive understanding on the mechanisms of each optoelectronic process has to be developed in future works. This may provide a guideline for future target-oriented host material developments and post-treatments.

Last but not least, we highlight that the decomposition may open a new means to produce self-organised ternary III-nitride QDs in a rather narrow size distribution. Comparing with current conventional methods, such as chemical synthesis in organic solvent and epitaxial growth of three-dimensional island by molecular beam epitaxy (MBE) or metal organic chemical vapour phase epitaxy (MOVPE), formation of the QDs through decomposition may significantly simplify the production process.

Appendix A

Parameters of sample preparations and thermal treatments

Parameters used for sample preparations and thermal treatments in the present work are listed in following tables.

Table A.1: Sputtering parameters for AlN:Ln (Ln = Pr, Sm, Tb and Tm), $Al_{0.87}In_{0.13}N$:Tm and $Al_{0.84}In_{0.16}N$:Pr layers.

layers	$p(N_2)^a$ mabr	$P(Al,1)^b$ W	$P(Al,2)^c$ W	$P(Ln)^d$ W	t^e h
AlN:Ln	7×10^{-3}	150	150	3	3

layers	$p(N_2)^a$ mabr	$P(Al)^b$ W	$P(In)^f$ W	$P(Ln)^d$ W	t^e h
$Al_{0.87}In_{0.13}N$:Tm	7×10^{-3}	250	65	3	3
$Al_{0.84}In_{0.16}N$:Pr	7×10^{-3}	250	55	3	3

[a] pressure of nitrogen process gas.
[b] sputtering power of first Al target.
[c] sputtering power of second Al target.
[d] sputtering power of lanthanide target.
[e] sputtering duration.
[f] sputtering power of second Al target, on which 2 In wire were placed.

Table A.2: Applied annealing temperatures and durations for encapsulated AlN:Ln and $Al_xIn_{1-x}N$:Ln layers. N_2 with calculated pressure, which ensures that it reaches approximately 1 bar during the annealing at selected temperatures, is chosen as protecting gas.

layers	annealing temperatures °C	annealing durations min
AlN:Ln	500, 700, 1000	5, 10, 20, 30, 45, 60
$Al_{0.87}In_{0.13}N$:Tm	700	5, 10, 30, 45, 60, 120, 180, 240
$Al_{0.84}In_{0.16}N$:Pr	700	5, 10, 15, 20, 30, 45, 60, 90

Appendix B

Basic characterisations on lanthanide doped AlN and $Al_xIn_{1-x}N$ layers

Concomitant investigations on the properties of AlN:Ln and $Al_xIn_{1-x}N$:Ln layers, such as chemical concentration, crystal structure and band gap energy, were done in the present work. Even though the results are indispensable to draw a complete view on these systems, they are not the main aims of our study. For this reason, we put some representative results of them in this appendix.

Chemical compositions

The concentrations of lanthanide dopants in AlN and $Al_xIn_{1-x}N$ were measured by ICP-OES (as introduced in section 2.4.1) and summarised in table B.1. Although the physical analyses are invalid to determine these concentration and the results of other metallic components are comparatively less accurate, one is able thereby to determine the concentrations of non-metallic components and even the depth profiles. Figure B.1 shows AES depth profiles of $Al_{0.83}In_{0.17}N$ layer before and after annealing.

Table B.1: Atomic concentration of lanthanide dopants in AlN and $Al_xIn_{1-x}N$ (ICP-OES).

samples	AlN:Pr	AlN:Sm	AlN:Tb	AlN:Tm	$Al_{0.87}In_{0.13}N$:Tm	$Al_{0.84}In_{0.16}N$:Pr
c_{Ln} (at.-%)	0.73	1.88	0.73	1.21	0.72	0.80
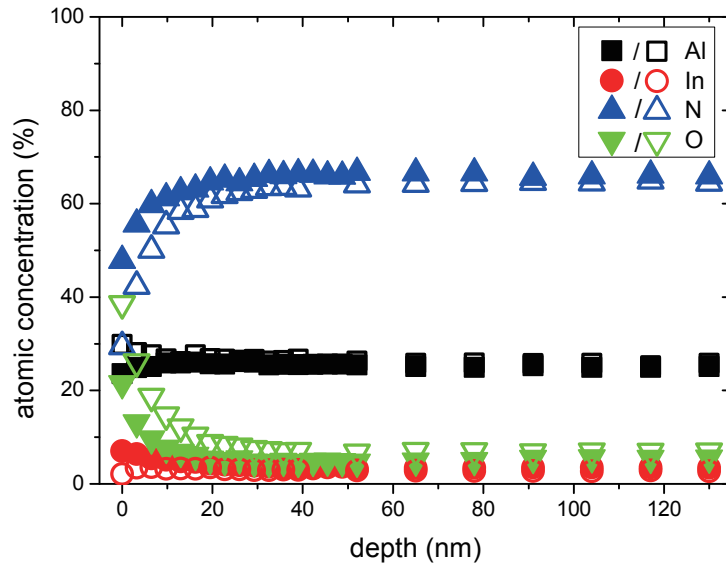
Figure B.1: AES depth profiles of Al$_{0.83}$In$_{0.17}$N layer (from layer surface to the depth of about 130 nm). Developments of atomic concentration, Al (black), In (red), N (blue) and O (green), before and after 30 minutes annealing at 700 °C (solid and hollow symbols, respectively) are shown.

Crystallographic structure and internal stress

Figure B.2 (a) represents examples of XRD spectra with different tilting angles Ψ. By using equation 2.3, the stress-free lattice parameters a_0 and c_0 as well as biaxial elastic internal stress $\sigma_\parallel$ of AlN:Pr and Al$_{0.84}$In$_{0.16}$N:Pr layers were calculated and listed in table B.2 and B.3 (sin$^2\Psi$-method, section 2.3.1). In Al$_x$In$_{1-x}$N layers the lattice constant increases with decreasing AlN content. According to equation 2.1, this leads to a shift of diffraction peaks in the direction to lower diffraction angle as shown in figure B.2 (b) (θ-2θ-measurement, section 2.3.1).
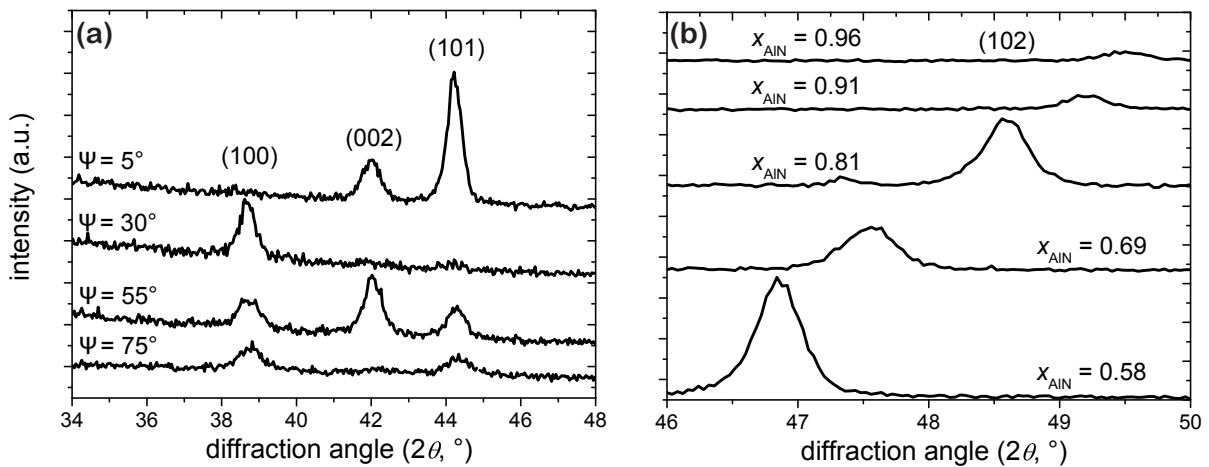
Figure B.2: (a) XRD spectra of AlN:Pr layer before annealing. (100), (002) and (101) reflexes as shown were taken with different tilting angles Ψ. (b) (102) reflex of Al$_x$In$_{1-x}$N layers with different AlN content.

Table B.2: Stress-free lattice parameters and biaxial elastic internal stress of AlN:Pr layers before and after 30 minutes annealing at 700 °C.

	a_0 nm	c_0 nm	$\sigma_\parallel$ MPa
before annealing	0.3120	0.4996	-563
after annealing	0.3115	0.4981	396

Table B.3: Stress-free lattice parameters and biaxial elastic internal stress of $Al_{0.84}In_{0.16}N$:Pr layers after annealing at 700 °C for different durations.

annealing duration t_{ann} min	a_0 nm	c_0 nm	$\sigma_\parallel$ MPa
0	0.3185	0.5105	-527
5	0.3178	0.5098	779
10	0.3179	0.5097	495
15	0.3177	0.5095	425
20	0.3177	0.5096	555
30	0.3176	0.5093	470
45	0.3178	0.5096	549
60	0.3177	0.5093	349
90	0.3178	0.5095	386
120	0.3175	0.5093	479

Optical band gap energy and Urbach energy

Optical band gap energy E_g and Urbach energy E_U of AlN and $Al_xIn_{1-x}N$ hosts were determined by graphical fitting to the plot of their optical absorption coefficient α versus photon energy (see figure B.3 (a) presenting the example of $Al_{0.58}In_{0.42}N$). Relationship between band gap energy and AlN content in $Al_xIn_{1-x}N$ is illustrated in figure B.3 (b) and compared with various references.
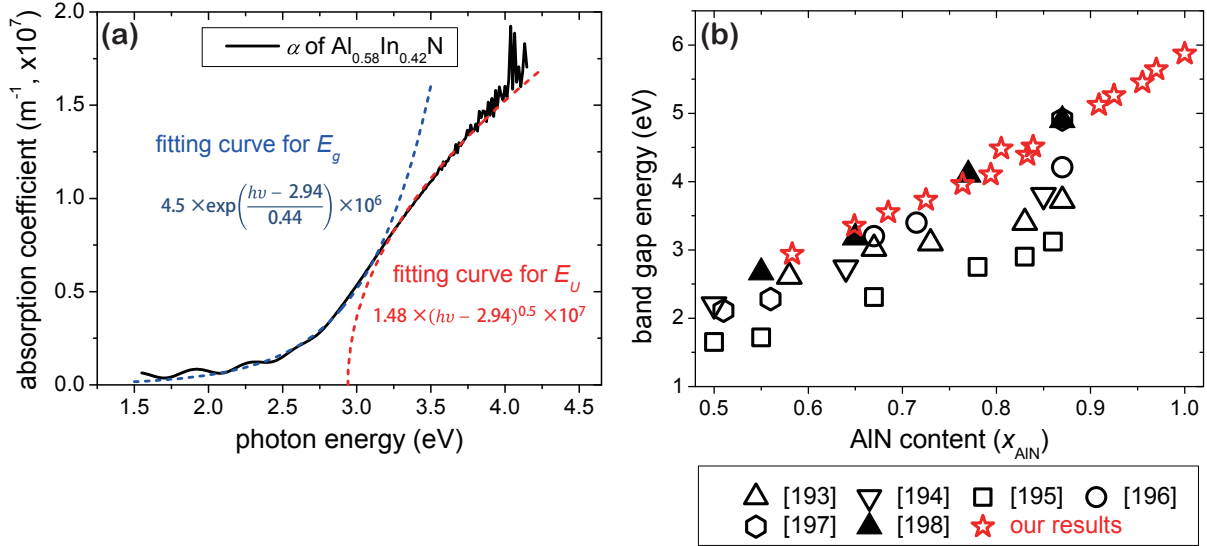
Figure B.3: (a) Dependency of optical absorption coefficient α of a $Al_{0.58}In_{0.42}N$ layer on the photon energy. Its optical band gap energy (2.94 eV) and Urbach energy (0.44 eV) is fitted by using equation 2.8a and 2.8b. (b) Dependency of optical band gap energy of $Al_xIn_{1-x}N$ layers on the AlN content x_{AlN}. Results of this work (red stars) are compared with the references [193, 194, 195, 196, 197, 198].

Appendix C

$4f$-levels of investigated lanthanide ions

(a) Pr^{3+}

band gap of AlN (6.2 eV)

energy (eV)

2.14 eV (579 nm)
2.36 eV (525 nm)
2.54 eV (488 nm)
2.27eV (545 nm)
1.93 eV (643 nm)

$^3P_2$ $^1I_6$ $^3P_1$
$^3P_0$
$^1D_2$
$^1G_4$
$^3F_4$ $^3F_3$
$^3F_2$
$^3H_6$
$^3H_5$
$^3H_4$

(b) Sm^{3+}

band gap of AlN (6.2 eV)

(c) Tb^{3+}

band gap of AlN (6.2 eV)
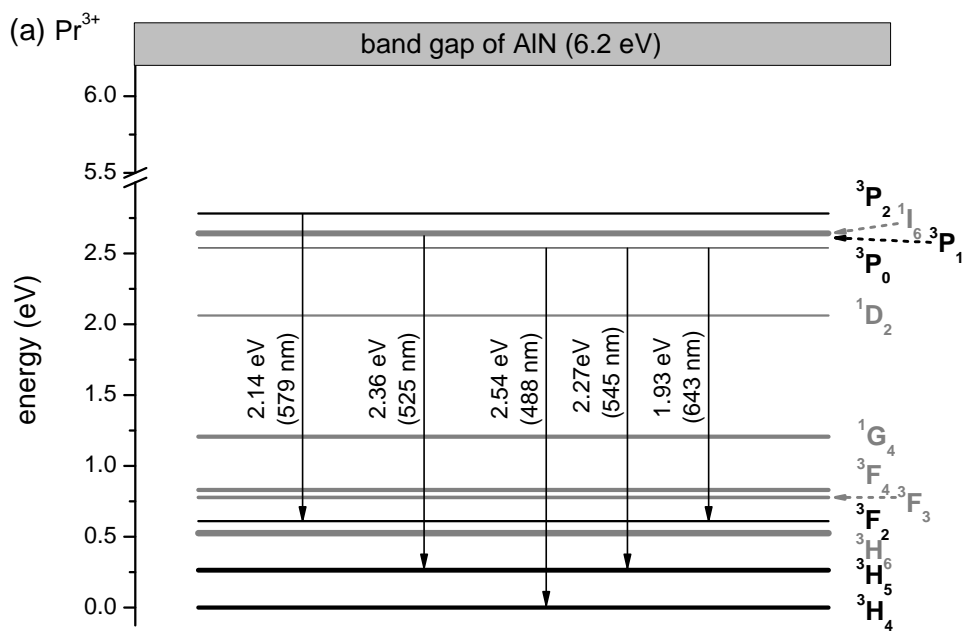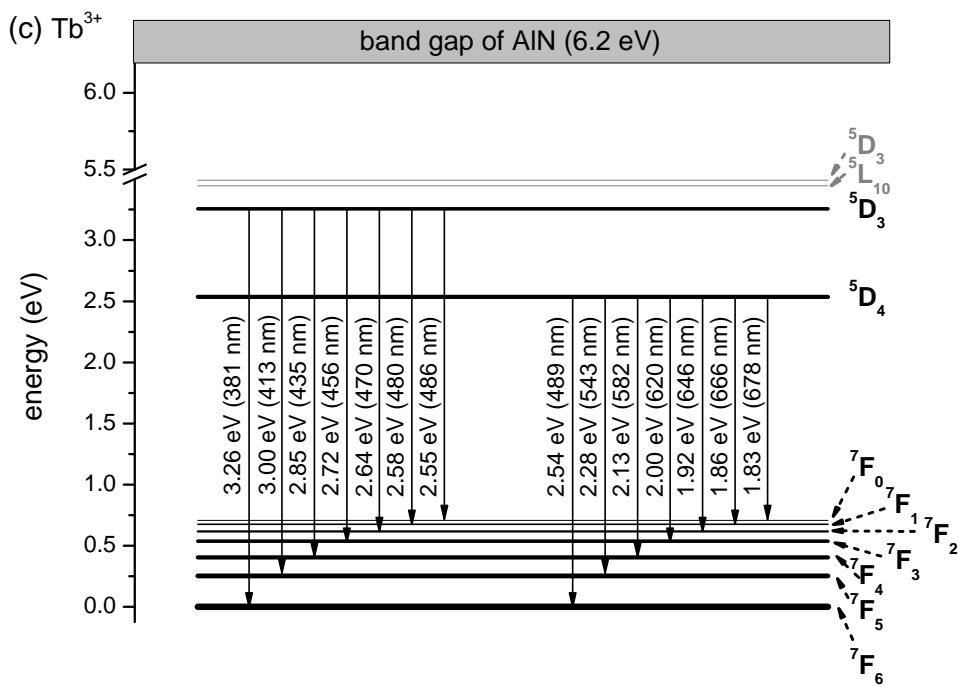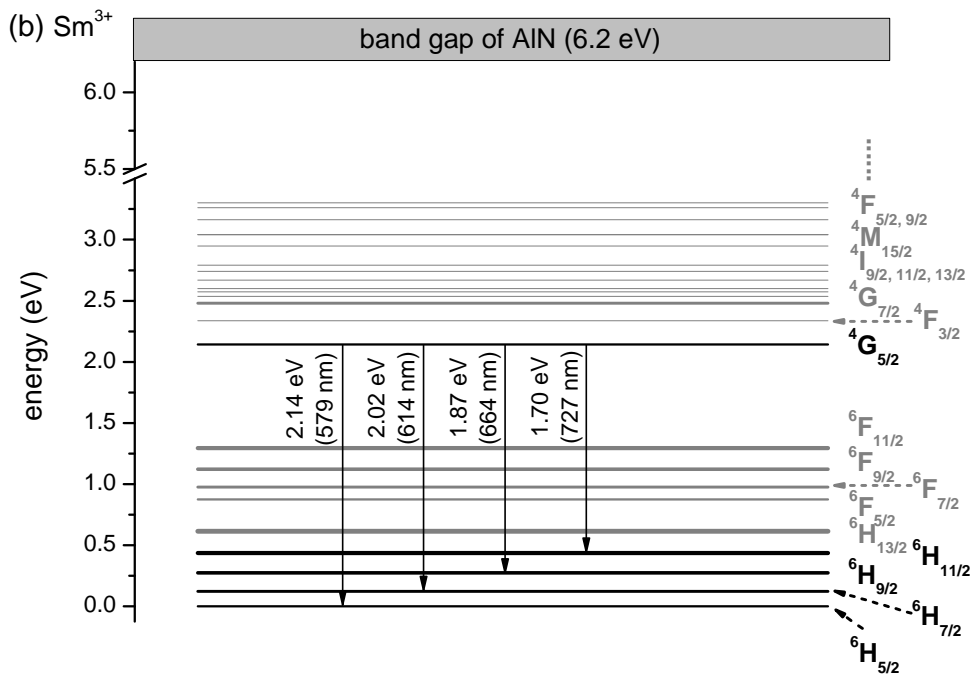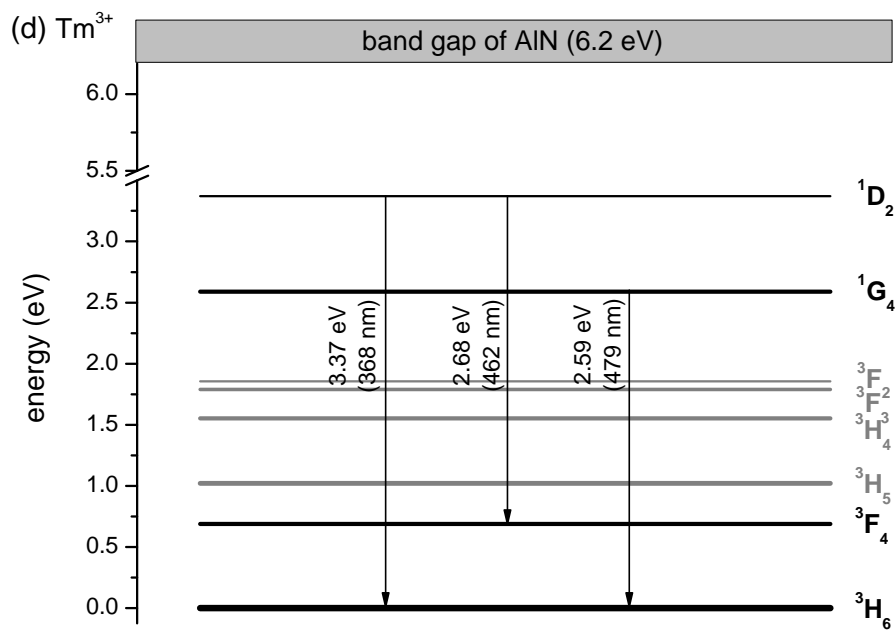
Figure C.1: Energy diagrams of $4f$-levels for Pr^{3+} (a), Sm^{3+} (b), Tb^{3+} (c) and Tm^{3+} (d) in an AlN host. The experimental observable transitions at room temperature and the corresponding energies in eV and nm are indicated as black lines. The energy levels, which were not confirmed experimentally in the present work, are taken from the Dieke diagram [47] and represented in gray lines. The position of band gap energy of AlN is represented for comparison.

D

Calculation of binodal and spinodal curves by using of Delta Lattice Parameter (DLP) and Valence Force Field (VFF) model

The chemical and coherent binodal/spinodal curves in the phase diagram of pseudo-binary system AlN-InN (figure 5.1) are calculated by using the Delta Lattice Parameter (DLP) and the Valence Force Field (VFF) model, respectively. The difference between both models is the way to calculate the enthalpy of mixing ΔH_m (presented as follows). Once this has been estimated, the binodal and spinodal curves can be quantified through drawing a tangent line to $\Delta G_m(x)$ and solving $\mathrm{d}^2 \Delta G_m/\mathrm{d}x^2 = 0$ respectively.

DLP model

In this model the enthalpy of mixing $\Delta H_m^{\mathrm{DLP}}$ is considered as the difference of solid state atomisation enthalpy $\Delta H_{at}(\mathrm{s})$ between $\mathrm{Al_x In_{1-x} N}$ and its nitride components, namely AlN and InN. G.B. Stringfellow suggested that ΔH_{at} is dependent on the lattice parameter of III-V compounds a_c in their cubic phase [199]:

$$\Delta H_{at} = K \cdot a_c^{-2.5}, \tag{D.1}$$

where K denotes a proportionality factor. And thus the enthalpy of mixing $\Delta H_m^{\mathrm{DLP}}$ for AlN-InN system (equation 5.4) can be rewritten as

$$\Delta H_m^{\mathrm{DLP}} = K\{a_{\mathrm{c\text{-}AlN}}^{-2.5} \cdot x_{\mathrm{AlN}} + a_{\mathrm{c\text{-}InN}}^{-2.5} \cdot (1 - x_{\mathrm{AlN}}) - [a_{\mathrm{c\text{-}InN}} + (a_{\mathrm{c\text{-}AlN}} - a_{\mathrm{c\text{-}InN}}) \cdot x_{\mathrm{AlN}}]^{-2.5}\}. \tag{D.2}$$

The III-nitrides with zinc blende structure are instable under conventional conditions. The calculated lattice parameter for cubic AlN amounts to $a_{\mathrm{c\text{-}AlN}} = 4.36$ Å and for InN $a_{\mathrm{c\text{-}InN}} = 4.98$ Å [200]. Based on the experimental results by using Knudsen cell mass spectroscopy, G. Meloni reported that the atomisation enthalpy of gaseous AlN $\Delta H_{at}(\mathrm{g})$

is 87.9 kcal/mol [201]. Taking the relationship of atomisation enthalpy of III-nitrides between their gaseous and solid state, $\Delta H_{at}(s) = 1.9230\Delta H_{at}(g) + 105.2$ kcal/mol [202], into account, the value of K is about 1.09×10^7 Å$^{2.5}$·cal/mol, which is in good agreement with the value determined in [199] (1.15×10^7 Å$^{2.5}$·cal/mol).

VFF model

According to equation 5.5, elastic strain energy E^{VFF} and appearance probability of each type of tetrahedron P_n^{VFF} must be clarified to determine the enthalpy of mixing $\Delta H_m^{\mathrm{VFF}}$. As illustrated in figure D.1,

$$P_{\mathrm{I}}^{\mathrm{VFF}} = (1 - x_{\mathrm{AlN}})^4 \qquad \text{for tetrahedron type I,} \tag{D.3a}$$

$$P_{\mathrm{II}}^{\mathrm{VFF}} = 4x_{\mathrm{AlN}}(1 - x_{\mathrm{AlN}})^3 \qquad \text{for tetrahedron type II,} \tag{D.3b}$$

$$P_{\mathrm{III}}^{\mathrm{VFF}} = 6x_{\mathrm{AlN}}^2(1 - x_{\mathrm{AlN}})^2 \qquad \text{for tetrahedron type III,} \tag{D.3c}$$

$$P_{\mathrm{IV}}^{\mathrm{VFF}} = 4x_{\mathrm{AlN}}^3(1 - x_{\mathrm{AlN}}) \qquad \text{for tetrahedron type IV,} \tag{D.3d}$$

$$P_{\mathrm{V}}^{\mathrm{VFF}} = x_{\mathrm{AlN}}^4 \qquad \text{for tetrahedron type V.} \tag{D.3e}$$
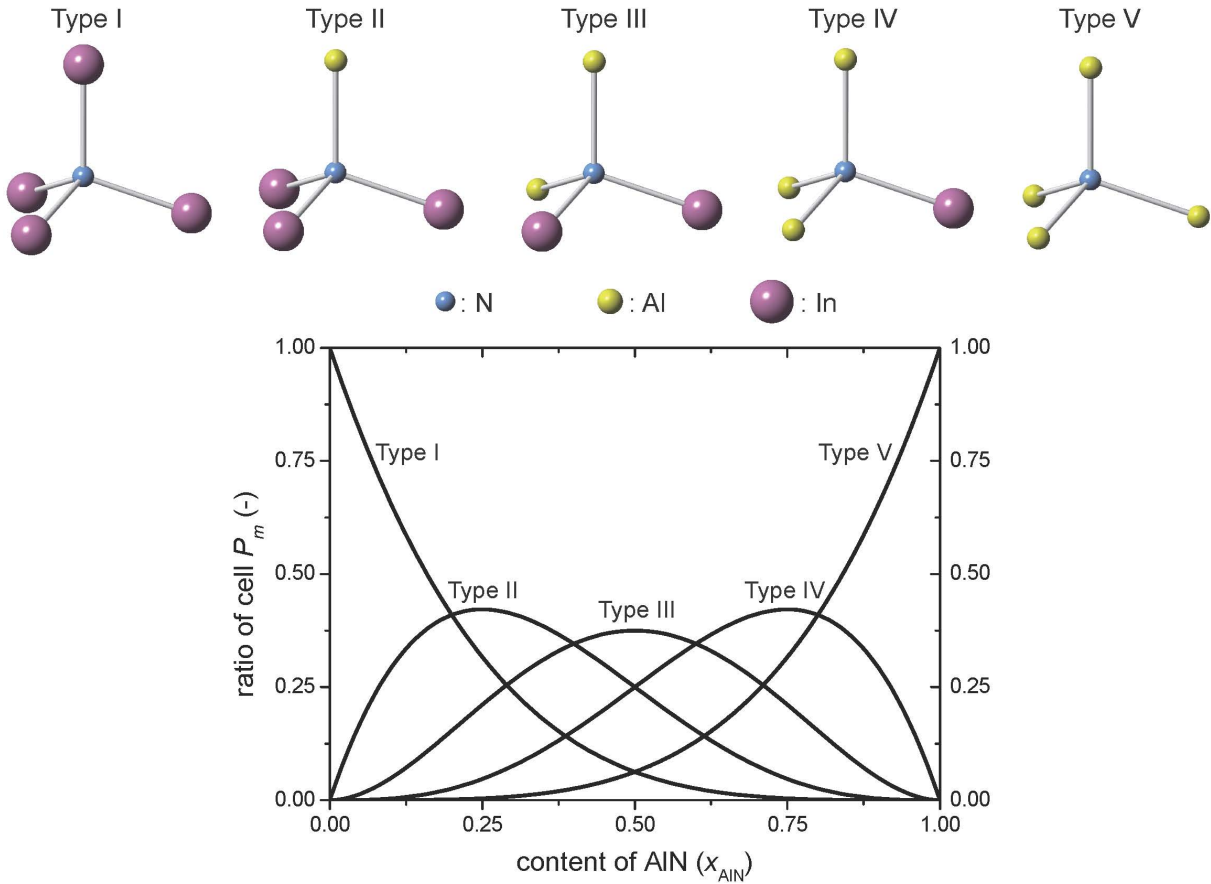

Figure D.1: Five types of $Al_x In_{1-x} N$ tetrahedron cells and the dependences of their distribution probabilities on the AlN content x_{AlN} [149].

Obviously the direct calculation of $\Delta H_m^{\mathrm{VFF}}$ for each individual AlN contents x_{AlN} is quite tedious. Inspired by the literature [13] we determined $\Delta H_m^{\mathrm{VFF}}$ through calculation of the interaction parameter Ω:

$$\Omega = \frac{\Delta H_m^{\mathrm{VFF}}}{x_{\mathrm{AlN}}(1 - x_{\mathrm{AlN}})} = \frac{C^{\mathrm{VFF}} \cdot \sum_{n=\mathrm{I}}^{n=\mathrm{V}} E_n^{\mathrm{VFF}} P_n^{\mathrm{VFF}}}{x_{\mathrm{AlN}}(1 - x_{\mathrm{AlN}})} \tag{D.4}$$

in both boundary conditions, $x_{\mathrm{AlN}} \to 0$ and $x_{\mathrm{AlN}} \to 1$, in which $E_{\mathrm{I}}^{\mathrm{VFF}}$ and $E_{\mathrm{V}}^{\mathrm{VFF}}$ is vanished, respectively. Hence, in these two cases only the tetrahedron type II and IV (equation D.3b and D.3d) are respectively needed to be considered:

$$\lim_{x_{\mathrm{AlN}} \to 0} \Omega = \lim_{x_{\mathrm{AlN}} \to 0} \left\{ C^{\mathrm{VFF}} \left[4(1 - x_{\mathrm{AlN}})^2 E_{\mathrm{II}}^{\mathrm{VFF}} + 6 x_{\mathrm{AlN}}(1 - x_{\mathrm{AlN}}) E_{\mathrm{III}}^{\mathrm{VFF}} + 4 x_{\mathrm{AlN}}^2 E_{\mathrm{IV}}^{\mathrm{VFF}} \right] \right\}$$
$$= 4 C^{\mathrm{VFF}} E_{\mathrm{II}}^{\mathrm{VFF}}, \tag{D.5a}$$

$$\lim_{x_{\mathrm{AlN}} \to 1} \Omega = \lim_{x_{\mathrm{AlN}} \to 1} \left\{ C^{\mathrm{VFF}} \left[4(1 - x_{\mathrm{AlN}})^2 E_{\mathrm{II}}^{\mathrm{VFF}} + 6 x_{\mathrm{AlN}}(1 - x_{\mathrm{AlN}}) E_{\mathrm{III}}^{\mathrm{VFF}} + 4 x_{\mathrm{AlN}}^2 E_{\mathrm{IV}}^{\mathrm{VFF}} \right] \right\}$$
$$= 4 C^{\mathrm{VFF}} E_{\mathrm{IV}}^{\mathrm{VFF}}. \tag{D.5b}$$

Assuming that Ω depends linearly on x_{AlN} [147], an expression of $\Delta H_m^{\mathrm{VFF}}$ over the entire compositional range x_{AlN} can be estimated.

It can be demonstrated that E^{VFF} decreases gradually and approaches to a quasi-constant value if the number of relaxed neighboring ion shell n increases. The lattice distortion due to the difference in ionic radius between Al and In is assumed in this work to be fully
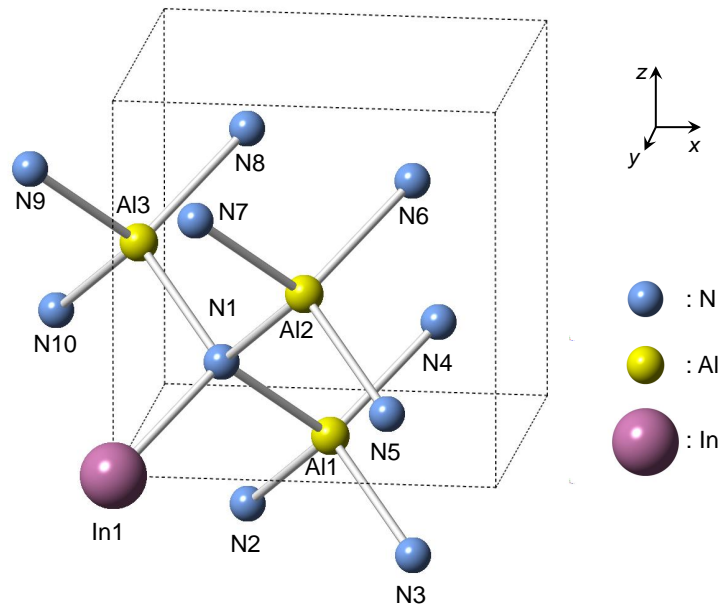
Figure D.2: 1/4 part of the structural model used to calculate the elastic strain energy in $\mathrm{Al_x In_{1-x} N}$ with $x_{\mathrm{AlN}} \to 1$. (namely AlN:In)

relaxed up to third nearest neighbouring ion shell ($n = 3$). This is reasonable, because in case of the GaInN system no noticeable differences between the results for $n = 3$ and $n > 3$ has been found [13]. Figure D.2 shows one quarter of the considered structural model as an example, in which very small amount of In is doped in AlN host ($x_{\text{AlN}} \rightarrow 1$). The centre lying In ion (In1) and N ions on the third shell (N2 - N10) are fixed on the positions, which are consistent with their sites in cubic AlN. So only appropriate positions of N ion ons the first shell (N1) and Al ions on the second shell (Al1 - Al3) has to be determined to minimise the elastic strain energy E^{VFF}. The bond-stretching and bond-bending force constant parameters (α and β from [203]) used for the calculation and the results of Ω are listed in table D.1.

Table D.1: Input parameters for VVF calculation and results of interaction parameter.

| | α | β | Ω |
	N/m	N/m	kcal/mol
InN:Al ($x_{\text{AlN}} \rightarrow 0$)	79.2	7.1	5.081
AlN:In ($x_{\text{AlN}} \rightarrow 1$)	98.0	15.0	5.509

Bibliography

[1] F. Dyson. A meeting with Enrico Fermi - How one intuitive physicist rescued a team from fruitless research. *Nature*, 427(6972):297, 2004.

[2] International Energy Agency. *Technology roadmap high-efficiency, low-emissions coal-fired power generation*. Printed in France by Corlet, October 2012.

[3] Commission Regulation (EC) No 244/2009. Implementing directive 2005 32 EC of the European parliament and of the council with regard to ecodesign requirements for non-directional household lamps. *Official Journal of the European Union*, 76:3–16, 2009.

[4] E.F. Schubert and J.K. Kim. Solid-state light sources getting smart. *Science*, 308(5726):1274–1278, 2005.

[5] D. L. MacAdam (Ed.). *Selected Papers on Colorimetry: Fundamentals*, volume 77 of *SPIE Milestone Series*. SPIE Press, 1993.

[6] A. Žukauskas, R. Vaicekauskas, F. Ivanauskas, R. Gaska, and M. S. Shur. Optimization of white polychromatic semiconductor lamps. *Applied Physics Letters*, 80(2):234–236, 2002.

[7] M.R. Krames, O.B. Shchekin, R. Mueller-Mach, G.O. Mueller, L. Zhou, G. Harbers, and M.G. Craford. Status and future of high-power light-emitting diodes for solid-state lighting. *Journal of Display Technology*, 3(2):160–175, 2007.

[8] J.M. Phillips, M.E. Coltrin, M.H. Crawford, A.J. Fischer, M.R. Krames, R. Mueller-Mach, G.O. Mueller, Y. Ohno, L.E. S. Rohwer, J.A. Simmons, and J.Y. Tsao. Research challenges to ultra-efficient inorganic solid-state lighting. *Laser & Photon Reviews*, 1(4):307–333, 2007.

[9] B. Bowers. *Lengthening the day: a history of lighting technology*. Oxford University Press, 1 edition, 1998.

[10] P. Waltereit, O. Brandt, A. Trampert, H. T. Grahn, J. Menniger, M. Ramsteiner, M. Reiche, and K. H. Ploog. Nitride semiconductors free of electrostatic fields for efficient white light-emitting diodes. *Nature*, 406:865–868, 2000.

[11] U.T. Schwarz and M. Kneissl. Nitride emitters go nonpolar. *physica status solidi (RRL)*, 1(3):44–46, 2007.

[12] F. Scholz, A. Sohmer, J. Off, V. Syganow, A. Dörnen, J.-S. Im, A. Hangleiter, and H. Lakner. In incorporation efficiency and composition fluctuations in MOVPE grown GaInN/GaN hetero structures and quantum wells. *Materials Science and Engineering B*, 50(1-3):238–244, 1997.

[13] I-H. Ho and G.B. Stringfellow. Solid phase immiscibility in GaInN. *Applied Physics Letters*, 69(18):2701–2703, 1996.

[14] J. S. Nelson, E. D. Jones, S. M. Myers, D. M. Follstaedt, H. P. Hjalmarson, J. E. Schirber, R. P. Schneider, J. E. Fouquet, V. M. Robbins, and K. W. Carey. Compositional dependence of the luminescence of $In_{0.49}(Al_y Ga_{1-y})_{0.51}P$ alloys near the direct-indirect band-gap crossover. *Physical Review B*, 53(23):15893–15901, 1996.

[15] T. Mukai, M. Yamada, and S. Nakamura. Characteristics of InGaN-based UV blue green amber red light-emitting diodes. *Japanese Journal of Applied Physics*, 38(7A):3976–3981, 1999.

[16] A.Y. Kim, W. Götz, D.A. Steigerwald, J.J. Wierer, N.F. Gardner, J. Sun, S.A. Stockman, P.S. Martin, M.R. Krames, R.S. Kern, and F.M. Steranka. Performance of high-power AlInGaN light emitting diodes. *Physica Status Solidi (A)*, 188(1):15–21, 2001.

[17] Y.C. Shen, G.O. Mueller, S. Watanabe, N.F. Gardner, A. Munkholm, and M.R. Krames. Auger recombination in InGaN measured by photoluminescence. *Applied Physics Letters*, 91(14), 2007. Article Number: 141101.

[18] J. Hader, J.V. Moloney, B. Pasenow, S.W. Koch, M. Sabathil, N. Linder, and S. Lutgen. On the importance of radiative and Auger losses in GaN-based quantum wells. *Applied Physics Letters*, 92(26), 2008. Article Number: 261103.

[19] D.P. Bour, D.W. Treat, R.L. Thornton, R.S. Geels, and D.F. Welch. Drift leakage current in AlGaInP quantum-well lasers. *IEEE Journal of Quantum Electronics*, 29(5):1337–1343, 1993.

[20] I.V. Rozhansky and D.A. Zakheim. Analysis of processes limiting quantum efficiency of AlGaInN LEDs at high pumping. *Physica Status Solidi A*, 204(1):227–230, 2007.

[21] M.-H. Kim, M.F. Schubert, Q. Dai, J.K. Kim, E.F. Schubert, J. Piprek, and Y. Park. Origin of efficiency droop in GaN-based light-emitting diodes. *Applied Physics Letters*, 91, 2007. Article Number: 183507.

[22] S. Chhajed, Y. Xi, Y.-L. Li, Th. Gessmann, and E.F. Schubert. Influence of junction temperature on chromaticity and color-rendering properties of trichromatic white-light sources based on light-emitting diodes. *Journal of Applied Physics*, 97(5), 2005. Article Number: 054506.

[23] P. Schlotter, R. Schmidt, and J. Schneider. Luminescence conversion of blue light emitting diodes. *Applied Physics A*, 64(4):417–418, 1997.

[24] R. Mueller-Mach, G.O. Mueller, M.R. Krames, and T. Trottier. High-power phosphor-converted light-emitting diodes based on III-nitrides. *IEEE Journal of selected Topics in Quantum Electronics*, 8(2):339–345, 2002.

[25] V. Bachmann, C. Ronda, and A. Meijerink. Temperature quenching of yellow Ce^{3+} luminescence in YAG:Ce. *Chemistry of Materials*, 21(10):2077–2084, 2009.

[26] Y.X. Pan, M.M. Wu, and Q. Su. Tailored photoluminescence of YAG:Ce phosphor through various methods. *Journal of Physics and Chemistry of Solids*, 65(5):845–850, 2004.

[27] H.S. Jang, W.B. Im, D.C. Lee, D.Y. Jeon, and S.S. Kim. Enhancement of red spectral emission intensity of $Y_3Al_3O_{12}$:Ce^{3+} phosphor via Pr co-doping and Tb substitution for the application to white LEDs. *Journal of Luminescence*, 126(2):371–377, 2007.

[28] S.-L. Chung, S.-C. Huang, W.-C. Chou, and W.W. Tangguh. Phosphors based on nitridosilicates: synthesis methods and luminescent properties. *Current Opinion in Chemical Engineering*, 3:62–67, 2014.

[29] W.M. Yen, S. Shionoya, and H. Yamamoto. *Phorsphor handbook*. CRC Press, 2 edition, 2006.

[30] C.T. Chen. Evolution of red organic light-emitting diodes materials and devices. *Chemistry of Materials*, 16(23):4389–4400, 2004.

[31] S. Schmidbauer, A. Hohenleutner, and B. König. Chemical degradation in organic light-emitting devices mechanisms and implications for the design of new materials. *Advanced Materials*, 25(15):2114–2129, 2013.

[32] K.S. Choi, F. Liu, J.S. Choi, and T.S. Seo. Fabrication of free-standing multilayered graphene and poly(3,4-ethylenedioxythiophene) composite films with enhanced conductive and mechanical properties. *Langmuir*, 26(15):12902–12908, 2010.

[33] H.S. Fairman, M.H. Brill, and H. Hemmendinger. How the CIE 1931 color-matching functions were derived from wright-guild data. *Color Research & Application*, 22(1):11–23, 1997.

[34] M. Böhme. Aktivierung von Lumineszenzzentren in Eu-dotierten AlN-Schichten durch Wärmebehandlung. Bachelor's thesis, Universität Stuttgart, 2013.

[35] D.V. Talapin, I. Mekis, S. Go1tzinger, A. Kornowski, O. Benson, and H. Weller. CdSe/CdS/ZnS and CdSe/ZnSe/ZnS core-shell-shell nanocrystals. *Journal of Physical Chemistry B*, 108(49):18826–18831, 2004.

[36] R.G. Xie, U. Kolb, J.X. Li, T. Basché, and A. Mews. Synthesis and characterization of highly luminescent CdSe-core CdS/ZnO$_{0.5}$Cd$_{0.5}$S/ZnS multi shell nanocrystals. *Journal of the American Chemical Society*, 127(20):7480–7488, 2005.

[37] P. Reiss, M. Protière, and L. Li. Core/shell semiconductor nanocrystals. *Small*, 5(2):154–168, 2009.

[38] S. Jun, J. Lee, and E. Jang. Highly luminescent and photostable quantum dot-silica monolith and its application to light-emitting diodes. *ACS Nano*, 7(2):1472–1477, 2013.

[39] O. Chen, J. Zhao, V.P. Chauhan, J. Cui, C. Wong, D.K. Harris, H. Wei, H.-S. Han, D. Fukumura, R.K. Jain, and M.G. Bawendi. Compact high-quality CdSe-CdS core-shell nanocrystals with narrow emission linewidths and suppressed blinking. *Nature Materials*, 12(5):445–451, 2013.

[40] http://www.qdvision.com/content1566.

[41] T.-H. Kim, K.-S. Cho, E.K. Lee, S.J. Lee, J. Chae, J.W. Kim, D.H Kim, J.-Y. Kwon, G. Amaratunga, S.Y. Lee, B.L. Choi, Y. Kuk, J.M. Kim, and K. Kim. Full-colour quantum dot displays fabricated by transfer printing. *Nature Photonics*, 5(3):176–182, 2011.

[42] E. Jang, S. Jun, H. Jang, J. Lim, B. Kim, and Y. Kim. White-light-emitting diodes with quantum dot color converters for display backlights. *Advanced Materials*, 22(28):3076–3080, 2010.

[43] Recommendation ITU-R BT.709-5. *Parameter values for the HDTV standards for production and international programme exchange.* International Telecommunication Union, 2002.

[44] National Television System Committee. *Report and Reports of Panel No. 11, 11-A, 12-19, with some supplementary references cited in the reports, and the petition for adoption of transmission standards for color television before the Federal Communications Commission.* Library of Congress Online Catalog, 1953.

[45] B.R. Judd, H.M. Crosswhite, and H. Crosswhite. Intra-atomic magnetic interactions for f electrons. *Physical Review*, 169(1):130–138, 1968.

[46] S. Gao (Ed.). *Molecular Nanomagnets and Related Phenomena*, volume 164 of *Structure and Bonding.* Springer-Verlag, 2015.

[47] G.H. Dieke. *Spectra and Energy Levels of Rare Earth Ions in Crystals.* Wiley-Interscience, 1968.

[48] J. Heikenfeld and A.J. Steckl. Alternating current thin-film electroluminescence of GaN:Er. *Applied Physics Letters*, 77(22):3520–3522, 2000.

[49] Y.Q. Wang and A.J. Steckl. Three-color integration on rare-earth-doped GaN electroluminescent thin films. *Applied Physics Letters*, 82(4):502–504, 2003.

[50] J.H. Kim abd P.H. Holloway. Near-infrared electroluminescence at room temperature from neodymium-doped gallium nitride thin films. *Applied Physics Letters*, 85(10):1689–1691, 2004.

[51] J. Heikenfeld, D.S. Lee, M. Garter, R. Birkhahn, and A.J. Steckl. Low-voltage GaN:Er green electroluminescent devices. *Applied Physics Letters*, 76(11):1365–1367, 2000.

[52] J.M. Zavada, S.X. Jin, N. Nepal, J.Y. Lin, H.X. Jiang, P. Chow, and B. Hertog. Electroluminescent properties of erbium-doped III-N light-emitting diodes. *Applied Physics Letters*, 84(7):1061–1063, 2004.

[53] A. Nishikawa, T. Kawasaki, N. Furukawa, Y. Terai, and Y. Fujiwara. Room-temperature red emission from a p-type europium-doped n-type gallium nitride light-emitting diode under current injection. *Applied Physics Express*, 2(7), 2009. Article Number: 071004.

[54] Y. Fujiwara and V. Dierolf. Present understanding of Eu luminescent centers in Eu-doped GaN grown by organometallic vapor phase epitaxy. *Japanese Journal of Applied Physics*, 53(5), 2014. Article Number: 05FA13.

[55] P.Y. Yu and M. Cardona. *Fundamentals of Semiconductors*. Springer-Verlag, 3 edition, 2001.

[56] F. Benz, H.P. Strunk, J. Schaab, U. Künecke, and P. Wellmann. Tuning the emission colour by manipulating terbium-terbium interactions: Terbium doped aluminium nitride as an example system. *Journal of Applied Physics*, 114(7), 2013. Article Number: 073518.

[57] O. Laporte and W. F. Meggers. Some rules of spectral structure. *Journal of the Optical Society of America and Review of Scientific Instruments*, 11(2):459–463, 1925.

[58] B. Henderson and G.F. Imbusch. *Optical spectroscopy of inorganic solids*. Oxford University Press, 1986.

[59] B.R. Judd. Optical absorption intensities of rare-earth ions. *Physical Review*, 127(3):750–761, 1962.

[60] G.S. Ofelt. Intensities of crystal spectra of rare-earth ions. *Journal of Chemical Physics*, 37(3):511–520, 1962.

[61] M.J. Wu, S.C. Erwin, and A. Trampert. Atomistic structure and energetics of GdN clusters in Gd-doped GaN. *Acta Materialia*, 76:87–93, 2014.

[62] I. Jlassi aand H. Elhouichet, M. Ferid, R. Chtourou, and M. Oueslati. Study of photoluminescence quenching in Er^{3+}-doped tellurite glasses. *Optical Materials*, 32(7):743–747, 2010.

[63] F. Benz, M. Yang, Y. Weng, and H.P. Strunk. Luminescenct intensity and dopant concentration in AlN:Tb. *Journal of Luminescence*, 132(6):1493–1496, 2012.

[64] M. Dolg, H. Stoll, and H. Preuss. A combination of quasirelativistic pseudopotential and ligand field calculations for lanthanoid compounds. *Theoretica Chimica Acta*, 85(6):441–450, 1993.

[65] U. Vetter, J.B. Gruber, A.S. Nijjar, B. Zandi, G. Öhl, U. Wahl, B.D. Vries, Hans Hofsäss, M. Dietrich, and the ISOLDE Collaboration. Crystal field analysis of Pm^{3+} ($4f^4$) and Sm^{3+} ($4f^5$) and lattice location studies of ^{147}Nd and ^{147}Pm in w-AlN. *Physical Review B*, 74(20), 2006. Article Number: 205201.

[66] R. Kolesov, K. Xia, R. Reuter, R. Stöhr, A. Zappe, J. Meijer, P.R. Hemmer, and J. Wrachtrup. Optical detection of a single rare-earth ion in a crystal. *Nature Communications*, 3, 2012. Article Number: 1029.

[67] Jr. K.A. Gschneidner and L. Eyring (Ed.). *Handbook on the Physics and Chemistry of Rare Earths, Chapter 155: Rationalization of crystal-field parametrization*, volume 23. Elsevier Science B.V., 1996.

[68] J.S. Griffith. *The theory of transition metal ions*. Cambridge University Press, 1961.

[69] S.Y. Zhang. The law and mechanism on ligand influencing the spectral parameter of rare earth ion in solid. *Chinese Journal of Chemical Physics*, 3(2):113 – 117, 1990.

[70] Jr. K.A. Gschneidner and L. Eyring (Ed.). *Handbook on the Physics and Chemistry of Rare Earths, Chapter 167: Spectral intensities of f-f transitions*, volume 25. Elseoier Science B.V., 1998.

[71] K.W.H. Stevens. Matrix elements and operator equivalents connected with the magnetic properties of rare earth ions. *Proceedings of the Physical Society of London*, 65(387):209–215, 1952.

[72] R.J. Elliott and K.W.H. Stevens. The theory of the magnetic properties of rare earth salts: Cerium Ethyl Sulphate. *Proceedings of the Royal Society of London. Series A, Mathematical and Physical Sciences*, 215(1123):437–453, 1952.

[73] R.J. Elliott and K.W.H. Stevens. The theory of magnetic resonance experiments on salts of the rare earths. *Proceedings of the Royal Society of London. Series A, Mathematical and Physical Sciences*, 215(1123):437–453, 1953.

[74] B.R. Judd. Operator equivalents and matrix elements for the excited states of rare-earth ions. *Proceedings of the Royal Society of London. Series A, Mathematical and Physical Sciences*, 227(1171):552–560, 1955.

[75] C.W. Nielson and G.F. Koster. *Spectroscopic Coefficients for the p^n, d^n, f^n Configurations*. The MIT Press, 1963.

[76] K.W.H. Stevens. Equivalent angular momentum operators for second quantised operators. *Physics Letters A*, A 47(5):401–403, 1974.

[77] K.H. Hellwege, E. Orlich, and G. Schaack. Absorptionsspektrum des Ce^{3+}-Ions und Kristallfeld im La(Ce)Cl. *Physik der kondensierten Materie*, 4(3):196–206, 1965.

[78] J.B. Gruber, D. Seltzer M, M.E. Hills, S.B. Stevens, and C.A. Morrison. Energy levels and upconversion fluorescence in trivalent thuliumdoped yttrium scandium aluminum garnet. *Physical Review B*, 48(21):15561–15573, 1993.

[79] E. Antic-Fidancev, M. Lemaitre-Blaise, and P. Porcher. Optical properties of $BaEu(CO_3)_2F$ and $Na_3La_2(CO_3)_4F$:Eu^{3+}: correlations to the crystallographic structures compounds. *Journal of Solid State Chemistry*, 116(2):286–289, 1995.

[80] G. Cucinotta, M. Perfetti, J. Luzon, M. Etienne, P.-E. Car, A. Caneschi, G. Calvez, K. Bernot, and R. Sessoli. Magnetic anisotropy in a dysprosium/DOTA single-molecule magnet beyond simple magneto-structural correlations. *Angewandte Chemie*, 51(7):1606–1610, 2012.

[81] K. Rajnak and B.G. Wybourne. Configuration interaction in crystal field theory. *Journal of Chemical Physics*, 41(2):565–569, 1964.

[82] J.J. Baldoví, J.J. Borrás-Almenar, J.M. Clemente-Juan, E. Coronado, and A. Gaita-Ariño. Modeling the properties of lanthanoid single-ion magnets using an effective point-charge approach. *Dalton Transactions*, 41(44):13705–13710, 2012.

[83] J.J. Baldoví, S. Cardona-Serra, J.M. Clemente-Juan, E. Coronado, A. Gaita-Ariño, and A. Palii. SIMPRE: A software package to calculate crystal field parameters, energy levels, and magnetic properties on mononuclear lanthanoid complexes based on charge distributions. *Journal of Computational Chemistry*, 34(22):1961–1967, 2013.

[84] Z.Y. Wu. AlN-Schichten: Abscheidung und optoelektronische Eigenschaften. Master's thesis, Universität Stuttgart, 2009.

[85] M. Pfund. Lumineszenzintensität von Sm-dotierten AlN-Schichten in Abhängigkeit von der Wärmebehandlung. Bachelor's thesis, Universität Stuttgart, 2012.

[86] U. Popp. Optoelektronische Eigenschaften von codotierten Aluminiumnitrid-schichten. Master's thesis, Universität Stuttgart, 2012.

[87] S. Petit, R. Jones, M.J. Shaw, P.R. Briddon, B. Hourahine, and T. Frauenheim. Electronic behavior of rare-earth dopants in AlN: A density-functional study. *Physical Review B*, 72(7), 2005. Article Number: 073205.

[88] B.D. Vries. *Lattice site location of impurities in group III nitrides using emission channeling*. PhD thesis, Katholieke Universiteit Leuven, 2006.

[89] J.L. Prather. *Atomic energy levels in crystals*. National Bureau of Standards Monograph, 1961.

[90] P. Boguslawski, E.L. Briggs, and J. Bernholc. Native defects in gallium nitride. *Physical Review B*, 51(23):17255–17258, 1995.

[91] J.-S. Filhol, R. Jones, M.J. Shaw, and P.R. Briddon. Structure and electrical activity of rare-earth dopants in GaN. *Applied Physics Letters*, 84(15):2841–2843, 2004.

[92] H. Bethe. Termaufspaltung in Kristallen. *Annalen der Physik*, 3(2):133–208, 1929.

[93] G.F. Koster, J.O. Dimmock, R.G. Wheeler, and H. Statz. *Properties of the thirty-two point groups*. MIT Press, 1962.

[94] T. Koubaa, M. Dammak, M. Kammoun, W.M. Jadwisienczak, H.J. Lozykowski, and A. Anders. Spectra and energy levels of Yb^{3+} in AlN. *Journal of Applied Physics*, 106(1), 2009. Article Number: 013106.

[95] J.B. Gruber, B. Zandi, H.J. Lozykowski, and W.M. Jadwisienczak. Spectra and energy levels of Tb^{3+} $(4f^8)$ in GaN. *Journal of Applied Physics*, 92(9):5127–5132, 2002.

[96] P.N. Favennec, H.L'Haridon, M. Salvi, D. Moutonnet, and Y. Le Guillou. Luminescence of erbium implanted in various semiconductors: IV, III-V and II-VI-materials. *Electronic Letters*, 25(11):718–719, 1989.

[97] H.J. Lozykowski and W.M. Jadwisienczak. Thermal quenching of luminescence and isovalent trap model for rare-earth-ion-doped AlN. *Physica Status Solidi B*, 244(6):2109–2126, 2007.

[98] A.R. Zanatta. Effect of thermal annealing treatments on the optical properties of rare-earth-doped AlN films. *Journal of Physics D*, 42(2), 2009. Article Number: 025109.

[99] P. Gehring, Y. Weng, Z.Y. Wu, and H.P Strunk. Photoluminescence from $Al_xIn_{1-x}N$ layers doped with Tb^{3+} ions. *Journal of Physics: Conference Series*, 281, 2011. Article Number: 012014.

[100] F. Benz. Unconventional light emission from thin III-nitride films. Master's thesis, Universität Stuttgart, 2013.

[101] G.A. Slack and T.F. McNelly. Growth of high purity AlN crystals. *Journal of Crystal Growth*, 34(2):263–279, 1976.

[102] R.A. Youngman and J.H. Harris. Luminescence studies of oxygen-related defects in aluminium nitride. *Journal of American Ceramic Society*, 73(11):3238–3246, 1990.

[103] J. W. McCauley and N. D. Corbin. High temperature reactions and microstructures in the Al_2O_3-AlN system. *Progress in Nitrogen Ceramics, NATO ASI Series*, 65:111–118, 1983.

[104] K.M. Krishnan, R.S. Rai, and G. Thomas. Characterization of long period polytypoid structures in the Al_2O_3-AlN systems. *MRS Proceedings*, 60:211–218, 1985.

[105] B. Feng. Herstellung und Charakterisierung von dünnen AlN Schichten. Master's thesis, Universität Stuttgart, 2008.

[106] F. Benz. Lumineszenzintensität und Dotierkonzentration am Beispiel von AlN:Tb. Bachelor's thesis, Universität Stuttgart, 2011.

[107] D. Feil. Lumineszenz von Er-dotierten AlN-Schichten in Abhängigkeit von der Auslagerungstemperatur. Bachelor's thesis, Universität Stuttgart, 2011.

[108] M. Yildirim. Photolumineszenz-Untersuchungen an AlN mit Tb^{3+}, Tm^{3+} und Sm^{3+} und AlInN mit Tm^{3+} Dotierung. Bachelor's thesis, Universität Ulm, 2015.

[109] H.J. Lozykowski, W.M. Jadwisienczak, A. Bensaoula, and O. Monteiro. Luminescence and excitation mechanism of Pr, Eu, Tb and Tm ions implanted into AlN. *Microelectronics Journal*, 36(3-6):453–455, 2005.

[110] T. Mattila and R.M. Nieminen. Ab initio study of oxygen point defects in GaAs, GaN, and AlN. *Physical Review B*, 54(23):16676–16682, 1996.

[111] D.J. Chadi and K.J. Chang. Theory of the atomic and electronic structure of DX centers in GaAs and $Al_xGa_{1-x}As$ alloys. *Physical Review Letters*, 61(7):873–876, 1988.

[112] C.G. van de Walle. DX-center formation in wurtzite and zinc-blende $Al_xGa_{1-x}N$. *Physical Review B*, 57(4):R2033–R2036, 1998.

[113] W.A. Groen, J.G. van Lierop, and A. Roosen. Electrical and thermal conductivity of AlN ceramics doped with beryllium and oxygen. *Journal of Materials Science Letters*, 12(15):1224–1226, 1993.

[114] S. Schweizer, U. Rogulis, J.-M. Spaeth, L. Trinkler, and B. Berzina. Investigation of oxygen-related luminescence centres in AlN ceramics. *Physica Status Solidi (B)*, 219(1):171–180, 2000.

[115] J. Pastrňák and L. Roskovcová. Optical absorption edge of AlN single crystals. *Physica Status Solidi*, 26(2):591, 1968.

[116] J.H. Harris, R.A. Youngman, and R.G. Teller. On the nature of the oxygen-related defect in aluminium nitride. *Journal of Materials Research*, 5(8):1763–1773, 1990.

[117] L. Trinkler and B. Berzina. Radiation induced recombination processes in AlN ceramics. *Journal of Physics-Condensed Matter*, 13(40):8931–8938, 2001.

[118] B. Berzina, L. Trinkler, J. Sils, and K. Atobe. Luminescence mechanisms of oxygen-related defects in AlN. *Radiation Effects & Defects in Solids*, 157(6-12):1089–1092, 2002.

[119] B. Berzina, L. Trinkler, D. Jakimovica, V. Korsaks, J. Grabis, I. Steins, E. Palcevskis, S. Bellucci, L.-C. Chen, S. Chattopadhyay, and K.-H. Chen. Spectral characterization of bulk and nanostructured aluminium nitride. *Journal of Nanophotonics*, 3, 2009. Article Number: 031950.

[120] J.C. Nappé, Ph. Grosseau, M. Benabdesselam, M. Beauvy, and B. Guilhot. Characterization of aluminium nitride material under swift heavy ion irradiations. *Proceedings of the 11th ECERS Conference*, pages 1105–1108, 2009.

[121] H.J. Lozykowski, W.M. Jadwisienczak, J. Han, and I.G. Brown. Luminescence properties of GaN and $Al_{0.14}Ga_{0.86}N$/AlN superlattice doped with europium. *Applied Physics Letters*, 77(6):767–769, 2000.

[122] T. Ishizaka, R. Nozaki, and Y. Kurokawa. Luminescence properties of Tb^{3+} and Eu^{3+}-doped alumina films prepared by sol-gel method under various conditions and sensitized luminescence. *Journal of Physics and Chemistry of Solids*, 63(4):316–617, 2002.

[123] A.J. Kenyon. Recent developments in rare-earthdoped materials for optoelectronics. *Progress in Quantum Electronics*, 26(4-5):225–284, 2002.

[124] T. Förster. Zwischenmolekulare Energiewanderung und Fluoreszenz. *Annalen der Physik*, 2(6):55–75, 1948.

[125] A. Wakahara, Y. Nakanishi, T. Fujiwara, H. Okada, A. Yoshida, T. Ohshima, T. Kamiya, and Y.-T. Kim. Strong blue emission from Er^{3+} doped in $Al_xGa_{1-x}N$. *Physica Status Solidi (A)*, 201(12):2768–2772, 2004.

[126] R. Weingärtner, O. Erlenbach, A. Winnacker, A. Welte, I. Brauer, H. Mendel, H.P. Strunk, C.T.M. Ribeiro, and A.R. Zanatta. Thermal activation, cathodo- and photoluminescence measurements of rare earth doped (Tm, Tb, Dy, Eu, Sm, Yb) amorphous/nanocrystalline AlN thin films prepared by reactive rf-sputtering. *Optical Materials*, 28(6-7):790–793, 2006.

[127] C. Stampfl and C.G. Van de Walle. Theoretical investigation of native defects, impurities, and complexes in aluminum nitride. *Physical Review B*, 65(15), 2002. Article Number: 155212.

[128] V.A. Soltamov, I.V. Ilyin, A.A. Soltamova, D.O. Tolmachev, N.G. Romanov, A.S. Gurin, V.A. Khramtsov, E.N. Mokhov, Y.N. Makarov, G.V. Mamin, S.B. Orlinskii, and P.G. Baranov. Shallow donors and deep-level color centers in bulk AlN crystals: EPR, ENDOR, ODMR and optical studies. *Applied Magnetic Resonance*, 44(10):1139–1165, 2013.

[129] E. Flegel. Thermische Aktivierung der Lumineszenzzentren in Tm-dotierten AlN-Schichten. Bachelor's thesis, Universität Stuttgart, 2011.

[130] T.L. Tansley and R.J. Egan. Point-defect energies in the nitrides of aluminium, gallium, and indium. *Physical Review B*, 45(19):10942–10950, 1992.

[131] D.W. Jenkins and J.D. Dow. Electronic structures and doping of InN, $In_xGa_{1-x}N$, and $In_xAl_{1-x}N$. *Physical Review B*, 39(5):3317–3329, 1989.

[132] A. Wakahara, T. Fujiwara, H. Okada, A. Yoshida, T. Ohshima, and H. Itho. Energy-back-transfer process in rare-earth doped AlGaN. *Materials Research Society Symposium Proceedings*, 886:V.3.9.1–V3.9.6, 2005.

[133] H.J. Lozykowski. Kinetics of luminescence of isoelectronic rare-earth ions in III-V semiconductors. *Physical Review B*, 48(24):17758–17769, 1993.

[134] E.J. Mittemeijer. Analysis of the kinetics of phase transformations. *Journal of Materials Science*, 27(15):3977–3987, 1992.

[135] F. Liu, F. Sommer, C. Bos, and E.J. Mittemeijer. Analysis of solid state phase transformation kinetics: models and recipes. *International Materials Reviews*, 52(4):193–212, 2007.

[136] H.E. Kissinger. Reaction kinetics in differential thermal analysis. *Analytical Chemistry*, 29(11):1702–1706, 1957.

[137] R.N. Bhargava, D. Gallagher, X. Hong, and A. Nurmikko. Optical properties of manganese-doped nanocrystals of ZnS. *Physical Review Letters*, 72(3):416–419, 1994.

[138] P.G. Kik and A. Polman. Exciton-erbium interactions in Si nanocrystal-doped SiO_2. *Journal of Applied Physics*, 88(4):1992–1998, 2000.

[139] Y. Hori, X. Biquard, E. Monroy, D. Jalabert, F. Enjalbert, Le Si Dang, M. Tanaka, O. Oda, and B. Daudin. GaN quantum dots doped with Eu. *Applied Physics Letters*, 84(2):206–208, 2004.

[140] Y. Hori, T. Andreev, D. Jalabert, E. Monroy, L.S. Dang, B. Daudin, M. Tanaka, and O. Oda. GaN quantum dots doped with Tb. *Applied Physics Letters*, 88(5), 2006. Article Number: 053102.

[141] B.A. Smith J.C. Woolley. Solid solution in $A^{III}B^V$ compounds. *Proceedings of the Physical Society of London*, 72(464):214–223, 1958.

[142] L.M. Foster and J.F. Woods. Thermodynamic analysis of the III-V alloy semiconductor phase diagrams 1. InSb-GaAs, and InP-GaP. *Journal of the Electrochemical Society*, 118(7):1175–1183, 1971.

[143] G.B. Stringfellow. Calculation of ternary and quaternary III-V phase diagrams. *Journal of Crystal Growth*, 27:21–34, 1974.

[144] J.W. Cahn. On spinodal decomposition. *Acta Metallurgica*, 9(9):795–801, 1961.

[145] P.N. Keating. Effect of invariance requirements on the elastic strain energy of crystals with application to the diamond structure. *Physical Review*, 145(2):637–645, 1966.

[146] J.L Martisn and A. Zunger. Bond lengths around isovalent impurities and in semiconductor solid solutions. *Physical Review B*, 30(10):6217–6220, 1984.

[147] T. Saito and Y. Arakawa. Atomic structure and phase stability of $In_xGa_{1-x}N$ random alloys calculated using a valence-force-field method. *Physical Review B*, 60(3):1701–1706, 1999.

[148] S.Y. Karpov, N.I. Podolskaya, and I.A. Zhmakin. Statistical model of ternary group-III nitrides. *Physical Review B*, 70(23), 2004. Article Number: 235203.

[149] M. Ichimura and A Sasaki. Short-range order in III-V ternary alloy semiconductors. *Journal of Applied Physics*, 60(11):3850–3855, 1986.

[150] L. Vegard. The constitution of the mixed crystals and the filling of space of the atoms. *Zeitschrift für Physik*, 5:17–26, 1921.

[151] L.K. Teles, L.M.R. Scolfaro, J.R. Leite, J. Furthmüller, and F. Bechstedt. Phase diagram, chemical bonds, and gap bowing of cubic $In_xAl_{1-x}N$ alloys: Ab initio calculations. *Journal of Applied Physics*, 92(12):7109–7113, 2002.

[152] M. Yang, Y. Weng, and H.P. Strunk. Spinodal decomposition and the luminescence of Er in $Al_xIn_{1-x}N$:Er layers. *Physica Status Solidi A*, 210(1):209–212, 2013.

[153] M. Tang and A. Karma. Surface modes of coherent spinodal decomposition. *Physical Review Letters*, 108(26), 2012. Article Number: 265701.

[154] W. Rieger, T. Metzger, H. Angerer, R. Dimitrov, O. Ambacher, and M. Stutzmann. Influence of substrate-induced biaxial compressive stress on the optical properties of thin GaN films. *Applied Physics Letters*, 68(7):970–972, 1995.

[155] C. Findler. Optoelectronic properties of praseodymium-doped $Al_xIn_{1-x}N$ layers. Bachelor's thesis, Universität Stuttgart, 2014.

[156] K.B. Rundman and J.E. Hilliard. Early stages of spinodal decomposition in an aluminium-zinc alloy. *Acta Metallurgica*, 15(6):1025–1033, 1967.

[157] J.W. Cahn and J.E. Hilliard. Free energy of a nonuniform system. I. interfacial free energy. *Journal of Chemical Physics*, 28(2):258–267, 1958.

[158] L.K. Teles, J. Furthmüller, L.M.R. Scolfaro, J.R. Leite, and F. Bechstedt. First-principles calculations of the thermodynamic and structural properties of strained $In_xGa_{1-x}N$ and $Al_xGa_{1-x}N$ alloys. *Physical Review B*, 62(4):2475–2485, 2000.

[159] E.A. Lass, W.C. Johnson, and G.J. Shiflet. Correlation between CALPHAD data and the Cahn-Hilliard gradient energy. *CALPHAD-Computer Coupling of Phase Diagrams and Thermochemistry*, 30(1):42–52, 2005.

[160] I.Z-. Tomaszkiewicz, R. Swierzewski, and P. Gierycz. Heat capacity of indium nitride. *Journal of Thermal Analysis and Calorimetry*, 91(2):649–653, 2008.

[161] J.F. Shackelford and W. Alexander. *Materials science and engineering handbook.* CRC Press, 3 edition, 2001.

[162] D.A. Huse. Corrections to late-stage behavior in spinodal decomposition lifshitz-slyozov scaling and monte carlo simulations. *Physical Review B*, 34(11):7845–7850, 1986.

[163] I.M. Lifshitz and V.V. Slyozov. The kinetics of precipitation from supersaturated solid solutions. *Journal of Physics and Chemistry of Solids*, 19(1-2):35–50, 1961.

[164] C. Wagner. Theorie der Alterung von Niederschlagen durch Umlosen (Ostwald-Reifung). *Zeitschrift für Elektrochemie*, 65(7-8):581–591, 1961.

[165] C. Tessarek, S. Figge, T. Aschenbrenner, S. Bley, A. Rosenauer, M. Seyfried, J. Kalden, K. Sebald, J. Gutowski, and D. Hommel. Strong phase separation of strained $In_xGa_{1-x}N$ layers due to spinodal and binodal decomposition: Formation of stable quantum dots. *Physical Review B*, 83(11), 2011. Article Number: 115316.

[166] M.V. Maximov, A.F. Tsatsul'nikov, B.V. Volovik, D.A. Bedarev, A.E. Zhukov, A.R. Kovsh, N.A. Maleev, V.M. Ustinov, P.S. Kop'ev, Zh.I. Alferov, R. Heitz, N.N. Ledentsov, and D. Bimberg and. Quantum dots formed by activated spinodal decomposition of InGa(Al)As alloy on InAs stressors. *Physica E*, 7(3-4):326–330, 2000.

[167] A.L. Efros. Interband absorption of light in a semiconductor sphere. *Soviet Physics Semiconductors - USSR*, 16(7):772–775, 1982.

[168] L.E. Brus. A simple model for the ionization potential, electron affinity, and aqueous redox potentials of small semiconductor crystallites. *Journal of Chemical Physics*, 79(11):5566–5571, 1983.

[169] B.E.A. Saleh and M.C. Teich. *Fundamentals of Photonics.* Wiley-VCH, 2 edition, 2007.

[170] Y.H. Huo, B.J. Witek, S. Kumar, J.R. Cardenas, J.X. Zhang, N. Akopian, R. Singh, E. Zallo, R. Grifone, D. Kriegner, R. Trotta1, F. Ding, J. Stangl, V. Zwiller, G. Bester, A. Rastelli, and O.G. Schmidt. A light-hole exciton in a quantum dot. *Nature Physics*, 10(1):46–51, 2014.

[171] P. Gehring. Optoelektronische Eigenschaften Seltenerd-dotierter III-Nitrid-Schichten. Master's thesis, Universität Stuttgart, 2010.

[172] P.Y. Yu and M. Cardona. *Fundamentals of Semiconductors.* Springer Verlag, 2003.

[173] M. Suzuki and T. Uenoyama. Strain effect on electronic and optical properties of GaN/AlGaN quantumwell lasers. *Applied Physics Letters*, 80(12):6868–6874, 1996.

[174] C.P. Foley and T.L. Tansley. Pseudopotential band structure of indium nitride. *Physical Review B*, 33(2):1430–1433, 1986.

[175] Y.C. Yeo, T.C. Chong, and M.F. Li. Electronic band structures and effective-mass parameters of wurtzite GaN and InN. *Journal of Applied Physics*, 83(3):1429–1436, 1998.

[176] S.K. Lim, M. Brewster, F. Qian, Y. Li, C.M. Lieber, and S. Gradečak. Direct correlation between structural and optical properties of III-V nitride nanowire heterostructures with nanoscale resolution. *Nano Letters*, 9(11):3940–3944, 2009.

[177] F. Qian, M. Brewster, S.K. Lim, Y.C. Ling, C. Greene, O. Laboutin, J.W. Johnson, S. Gradečak, Y. Cao, and Y. Li. Controlled synthesis of AlN/GaN multiple quantum well nanowire structures and their optical properties. *Nano Letters*, 12(6):3344–3350, 2012.

[178] L. Brusaferri, S. Sanguinetti, E. Grilli, M. Guzzi, A. Bignazzi, F. Bogani, L. Carraresi, M. Colocci, A. Bosacchi, P. Frigeri, and S. Franchi. Thermally activated carrier transfer and luminescence line shape in selforganized InAs quantum dots. *Applied Physics Letters*, 69(23):3354–3356, 1996.

[179] A.V. Uskov, J. McInerney, F. Adler, H. Schweizer, and M. H. Pilkuhn. Auger carrier capture kinetics in self-assembled quantum dot structures. *Applied Physics Letters*, 72(1):58–60, 1998.

[180] A.S. Bracker, M. Scheibner, M.F. Doty, E.A. Stinaff, I.V. Ponomarev, J.C. Kim, L.J. Whitman, T. L. Reinecke, and D. Gammon. Engineering electron and hole tunneling with asymmetric InAs quantum dot molecules. *Applied Physics Letters*, 89(23), 2006. Article Number: 233110.

[181] S. Marcinkevicius and R. Leon. Photoexcited carrier transfer in InGaAs quantum dot structure. *Applied Physics Letters*, 76(17):2406–2408, 2000.

[182] R.M. Clegg. Forster resonance energy transfer - FRET what is it, why do it, and how it's done. *FRET and FLIM Techniques Book Series: Laboratory Techniques in Biochemistry and Molecular Biology*, 33:1–57, 2009.

[183] K. O'Donnell and V. Dierolf (Ed.). *Rare Earth Doped III-Nitrides for Optoelectronic and Spintronic Applications*. Springer Verlag, 2010.

[184] J. Kistner, X. Chen, Y. Weng, H.P. Strunk, M.B. Schubert, and J. H. Werner. Photoluminescence from silicon nitride - no quantum effect. *Journal of Applied Physics*, 110(2), 2011. Article Number: 023520.

[185] A. Rose. Recombination processes in insulators and semiconductors. *Physical Review*, 97(2):322–333, 1955.

[186] D. Bimberg, N. Kirstaedter, N.N. Ledentsov, Zh.I. Alferov, P.S. Kop'ev, and V.M. Ustinov. InGaAs-GaAs Quantum-dot lasers. *IEEE Journal of Selected Topics in Quantum Electronics*, 3(2):196–205, 1997.

[187] J. Siegert, S. Marcinkevičius, and Q.X. Zhao. Carrier dynamics in modulation-doped InAs/GaAs quantum dots. *Physical review B*, 72(8):085316, 2005.

[188] T. Andreev, N.Q. Liem, Y. Hori, M. Tanaka, O. Oda, D.L.S. Dang, B. Daudin, and B. Gayral. Optical study of excitation and deexcitation of Tm in GaN quantum dots. *Physical Review B*, 74(15), 2006. Article Number: 155310.

[189] L.C. Chao and A.J. Steckl. Room-temperature visible and infrared photoluminescence from Pr-implanted GaN films by focused-ion-beam direct write. *Applied Physics Letters*, 74(16):2364–2366, 1999.

[190] S.F. Song, W.D. Chen, F.H. Su, J.J. Zhu, K. Ding, and C.C. Hsu. Structure and photoluminescence studies of Pr-implanted GaN. *Journal of Crystal Growth*, 267(3-4):400–404, 2004.

[191] C.K. Jørgensen and B.R. Hudd. Hypersensitive pseudoquadrupole transitions. *Molecular Physics*, 8(3):281–290, 1964.

[192] J.F. Suyver, A. Aebischer, D. Biner, P. Gerner, J. Grimm, S. Heer, K.W. Krämer, C. Reinhard, and H.U. Güdel. Novel materials doped with trivalent lanthanides and transition metal ions showing near-infrared to visible photon upconversion. *Optical Materials*, 27(6):1111–1130, 2005.

[193] K. Kubota, Y. Kobayashi, and K. Fujimoto. Preparation and properties of III-V nitride thin films. *Journal of Applied Physics*, 66(7):2984–2988, 1989.

[194] T. Peng, J. Piprek, G. Qiu, J. O. Olowolafe, K. M. Unruh, C. P. Swann, and E. F. Schubert. Band gap bowing and refractive index spectra of polycrystalline $Al_xIn_{1-x}N$ films deposited by sputtering. *Applied Physics Letters*, 71(17):2439–2441, 1997.

[195] S. Yamaguchi, M. Kariya, S. Nitta, T. Takeuchi, C. Wetzel, H. Amano, and I. Akasaki. Anomalous features in the optical properties of $Al_xIn_{1-x}N$ on GaN grown by metal organic vapor phase epitaxy. *Applied Physics Letters*, 76(7):876–878, 2000.

[196] M.J. Lukitsch, Y.V. Danylyuk, V.M. Naik, C. Huang, G.W. Auner, L. Rimai, and R. Naik. Optical and electrical properties of $Al_xIn_{1-x}N$ films grown by plasma source molecular-beam epitaxy. *Applied Physics Letters*, 79(5):632–634, 2001.

[197] W. Terashima, S.-B. Che, Y. Ishitani, and A. Yoshikawa. Growth and characterization of AlInN ternary alloys in whole composition range and fabrication of InN/AlInN multiple quantum wells by RF molecular beam epitaxy. *Japanese Journal of Applied Physics*, 45(21):539–542, 2006.

[198] T.S. Yeh, J.M. Wu, and W.H. Lan. Electrical properties and optical bandgaps of AlInN films by reactive sputtering. *Journal ofCrystalGrowth*, 310(24):5308–5311, 2008.

[199] G.B. Stringfellow. Calculation of regular solution interaction parameters in semiconductor solid solutions. *Journal of Physics and Chemistry of Solids*, 34(10):1749–1750, 1973.

[200] S.H. Wei and A. Zunger. Valence band splittings and band offsets of AlN, GaN, and InN. *Applied Physics Letters*, 69(18):2719–2721, 1996.

[201] G. Meloni and K.A. Gingerich. Thermodynamic study of the gaseous molecules Al_2N, AlN, and Al_2N_2 by Knudsen cell mass spectrometry. *Journal of Chemical Physics*, 113(24):10978–10982, 2000.

[202] L. von Szentpály. Atom-based thermochemistry crystal atomization and sublimation enthalpies in linear relationships to molecular atomization enthalpy. *Journal of the American Chemical Society*, 130(18):5962–5973, 2008.

[203] K. Kim, W.R.L. Lambrecht, and B. Segall. Elastic constants and related properties of tetrahedrally bonded BN, AlN, GaN, and InN. *Physical Review B*, 53(24):16310–16326, 1996.